Analysis of Crystal and Electronic Structures of Next Generation Cathode Materials

Aruto Watanabe

Analysis of Crystal and Electronic Structures of Next Generation Cathode Materials

Aruto Watanabe

Graduate School of Human and Environmental Studies
Kyoto University

Outline

Chapter 1. General Introduction

1-1. Background

The first secondary battery (storage battery) that could be used repeatedly by recharging was the lead storage battery invented by Plante in 1859 [1]. Various improvements have been made to lead-acid batteries since then, and are still generally used as automobile-mounted batteries.

Recently, lithium-ion batteries, nickel/hydrogen batteries, and others have been developed and widely used as power sources for small electronic devices including mobile phones and personal computers [1, 2]. The development and popularization of excellent secondary batteries have greatly contributed to miniaturization, weight reduction, and improved performance of large electronic devices such as portable computers.

In particular, since the 2000s, mobile phones and notebook PCs have greatly increased in popularity, and the role of secondary batteries in the industrial development and convenience in daily life has continued to expand.To solve global problems, including global warming and depletion of energy resources, power generation technology using natural energy such as solar, wind, and geothermal must be developed to replace fossil fuels. To widely spread the use of these renewable energy sources, a technology that enables stable power supply regardless of the time of production and the weather is required. Secondary batteries are expected to play an important role for leveling output power and effectively storing surplus power.

Secondary batteries are expected to become increasingly popular in transportation machinery as a power source for next-generation electric vehicles and hybrid vehicles that replace gasoline vehicles that emit CO_2, NO_x, etc.... The development of electric vehicles with extended ranges will require secondary batteries with higher energy density than that of existing secondary batteries [2].

Furthermore, recently in Japan, the demand for public transportation has increased in the major metropolitan areas of Tokyo, Osaka, and Nagoya, which have a huge population [3]. Storage batteries can also be used as a power source for land-based mass transportation such as railways and buses [4]. Japan has an aging society, as the total population began to decline after peaking in 2008, and continues to decline rapidly,

especially in rural areas [5]. It is estimated that Japan's population in 2050 will be approximately 75% of that in 2010 [5]. This necessitates the rapid development and maintenance of the society.

It is important to build and implement comprehensive policies by utilizing knowledges from a wide range of fields, rather than thinking separately about each policy. Energy policy is no exception and the development of large-scale secondary batteries that enable large-capacity electricity storage and supply will be important for realizing a sustainable society.

1-2. Lithium-Ion Batteries

1-2-1. Mechanism

The cathode material of lithium ion secondary batteries in current practical use is a Li^+ ion containing transition metal oxide such as lithium cobalt oxide ($LiCoO_2$). In addition, graphite is mainly used for the anode, where lithium perchlorate ($LiClO_4$) and lithium hexafluorophosphate ($LiPF_6$) can be dissolved in a mixed organic solvent such as a carbonate ester as the supporting electrolyte.

In addition, various substances have been studied as novel battery materials, and research has been conducted for their practical application. The secondary battery configuration shown in Figure 1-1 uses a layered carbon material for the anode, $LiCoO_2$ for the cathode material, and an organic electrolyte to dissolve Li salt, which was practically used by Asahi Kasei and Sony in 1991. The reaction equation is expressed in Eq. (1.1).

$$\begin{aligned} &\text{Cathode} && Li_{1-x}CoO_2 + xLi^+ + xe^- \leftrightarrow LiCoO_2 \\ &\text{Anode} && Li_xC_6 \leftrightarrow xLi^+ + xe^- + C_6 \\ &\text{All} && Li_{1-x}CoO_2 + Li_xC_6 \leftrightarrow LiCoO_2 + C_6 \end{aligned} \tag{1.1}$$

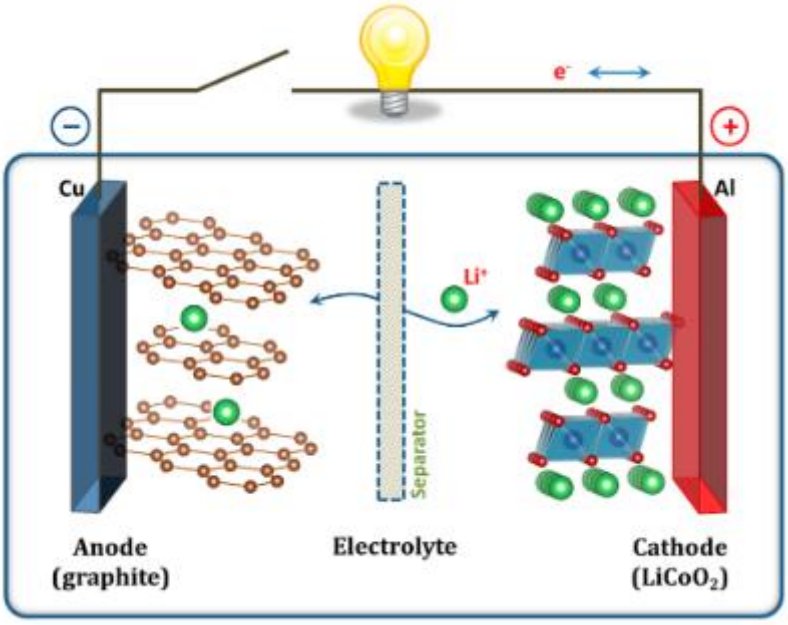

Figure 1-1. Structure of a lithium-ion battery. [6].

During the charging reaction, Li^+ in the cathode material is desorbed and eluted in the electrolytic solution, and Li^+ in the electrolytic solution is inserted between the anode carbons. At this time, electrons flow from the cathode to anode via an external circuit. The reverse reaction occurs during the discharge reaction, where Li^+ and electrons move from the anode toward the cathode. This reaction, called intercalation, proceeds while maintaining the host structure of both electrodes, and largely governs the reversible stability during the charge/discharge reaction.

Energy density is expressed as the product of the cell voltage and amount of electricity that can be stored per unit weight or volume. Lithium-ion batteries exhibit the highest energy density among currently available secondary batteries because lithium, which is responsible for charge transport, is the lightest metal and its redox potential is the most basic, allowing increased cell voltage.

1-2-2. Challenges

A quarter of a century has passed since the practical application of the $LiCoO_2$ cathode, and demand for this technology continues to expand. Under modern

circumstances, lithium-ion batteries currently in practical use have major problems. The first major problem is capacity, which is directly related to the size of the storage battery. $LiCoO_2$ can theoretically extract a capacity of 274 mAh g^{-1}, assuming that all Li^+ can be desorbed. However, when the amount of Li^+ desorption reaches 0.4 to 0.5 electrons, phase transition from orthorhombic to monoclinic occurs, changing the crystal structure [7-9]. For this reason, the range in which reversible Li^+ insertion/desorption can be performed in Li_xCoO_2 is limited to $0.5 < x < 1$, as shown in Eq. (1.1). The actual working capacity of this type of battery is approximately 130 to 140 mAh g^{-1}, which is nearly half of the theoretical value, which represents a practical limit. Another problem is that Co, which is a rare transition metal, is quite expensive. Many studies have been performed to develop a novel cathode materials to replace $LiCoO_2$, and the following sections outlines a few examples.

1-3. Cathode Materials

1-3-1. Layered rock salt-type oxide cathode materials

Figure 1-2 shows the structure of $LiCoO_2$ as a typical example of a layered rock salt-type oxide cathode material.

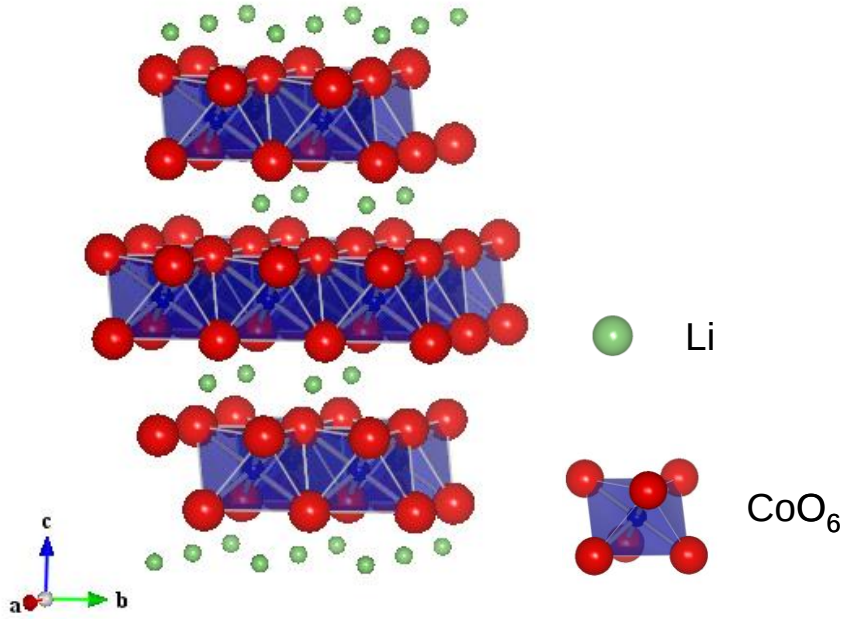

Figure 1-2. Structure of $LiCoO_2$.

As the name suggests, the Li layers and transition metal layers exist alternately in a layered structure. As described above, the host structure does not change even when a Li^+ desorption occurs. In addition to $LiCoO_2$, many layered rock salt-type oxide cathode materials have been studied, such as $LiNiO_2$ in which Co is replaced with Ni. Co and Ni are adjacent transition metals in the periodic table and have similar atomic weights and properties. The theoretical capacity of $LiNiO_2$ is 275 mAh g^{-1} which is nearly the same as $LiCoO_2$, but Ni is cheaper and more abundant than Co.

However, $LiNiO_2$ tends to be reduced from Ni^{3+} to Ni^{2+} during synthesis, resulting in the formation of Li deficient $Li_{1-x}Ni_{1+x}O_2$ [10]. In addition, when Li^+ is desorbed from $LiNiO_2$, Ni moves from the 3b site to the Li^+ 3a site, and cation mixing occurs so that Li^+ occupies the 3b site when large amounts of Li are present [11,12]. Therefore, the Ni-based material is not easy to synthesize compared to $LiCoO_2$ and its rate performance and cycle performance are easily degraded due to decreased Li^+ diffusion rate [13].

In addition, as a layered type cathode material, research has been conducted on a material in which some Co in $LiCoO_2$ is replaced with another transition metal. A popular example is the Ni/Co/Mn ternary layered oxide of $LiNi_{1/3}Co_{1/3}Mn_{1/3}O_2$ reported by Ohzuku et al. [14]. This material can be obtained by replacing 1/3 of the Co in $LiCoO_2$ with Ni and Mn, maintaining electrical stability by replacing trivalent Co with divalent Ni and tetravalent Mn.

Since Mn^{4+} cannot be further oxidized and is electrochemically inactive, Ni and Co are oxidized when Li is desorbed for charge compensation. The existence of Mn increased the thermal stability of highly oxidized electrodes [15]. Because the Co content is lower in this material compared to that in $LiCoO_2$, it is a novel cathode material that has the potential to replace $LiCoO_2$.

However, it has been highlighted that the rate performances of this novel material are low compared to those of $LiCoO_2$, because Li^+ diffusion is slow, and capacity degradation is significant when charged to a high potential of $\geq$ 4.5 V (vs Li / Li^+) [15,16].

1-3-2. Spinel-type cathode materials

An example of a cathode material with a typical spinel structure, $LiMn_2O_4$ has been extensively studied and Figure 1-3 shows its structure.

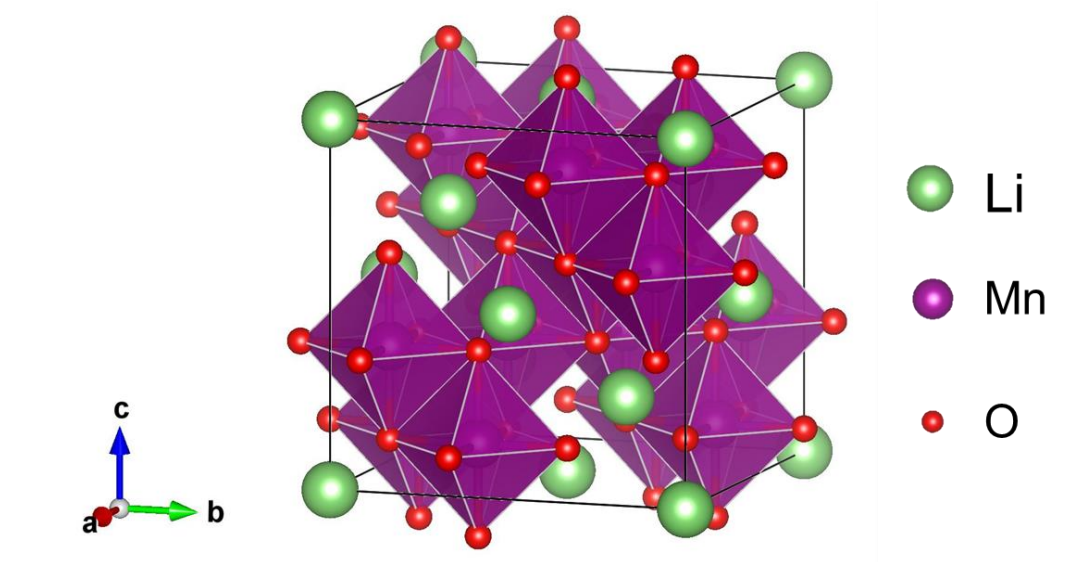

Figure 1-3. Structure of $LiMn_2O_4$.

The theoretical capacity of $LiMn_2O_4$ is 148 mAh g^{-1}, which is small compared to those of $LiCoO_2$ and $LiNiO_2$. However, the main constituent transition metal Mn, is low-cost and abundant, with features such as relatively low environmental impact and high safety during charging [17].

A major issue with the $LiMn_2O_4$ cathode is its poor cycle performance due to the elution of Mn ions into the electrolyte and crystal structure distortion due to the presence of Mn^{3+}, which is a Jahn-Teller ion [18,19]. Therefore, research was performed to improve the charge/discharge performance by replacing some Mn with other metals [20]. Kaneko et al. examined the mechanism of cycle performance improvement via substitution experimentally and computationally by analyzing the local structure of the Co/Cr substituted Mn spinel $LiM_yMn_{2-y}O_4$ (M = Co, Cr), showing that excellent charge/discharge performances were obtained in the 4 V region for Cr-substituted materials [21]. Kaneko et al. also argued that the reduction in local strain due to substitution and increased bonding strength between Mn-O are factors that improve the

cycle performance. In addition, substitutional spinel oxides including those containing Co, Cr, Ni, and Fe that operate at a high potentials of ≥4.5 V have attracted significant attention for realizing higher energy densities [22,23]. In particular, Ni-substituted electrode materials for large-capacity batteries have shown great potential because of their high capacity and excellent charge/discharge performance.

1-3-3. Olivine structure cathode materials

Cathode materials with an olivine structure, represented by $LiMPO_4$ (M = Mn, Co, Ni, Fe), were first reported by Padhi et al. [24]. The most common representative of this material type is lithium iron phosphate ($LiFePO_4$) and Figure 1-4 shows its structure.

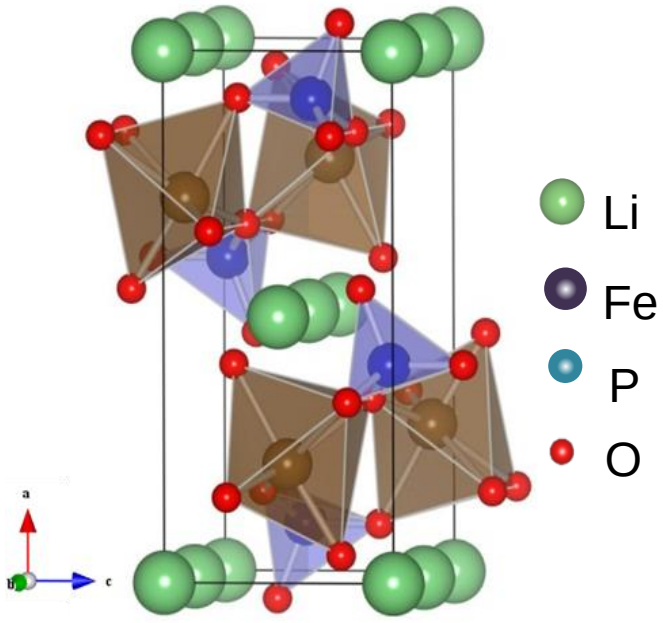

Figure 1-4. Structure of $LiFePO_4$.

$LiFePO_4$ has the great advantage of containing Fe, which is inexpensive and abundant, exhibiting a relatively high potential of approximately 3.5 V. Because PO_4 forms a stable skeletal structure, the materials exhibits excellent thermal stability and cycle performances during charging [25]. Moreover, despite the relatively low

theoretical capacity of 170 mAh g^{-1}, it has been reported that a capacity close to the theoretical value can be obtained experimentally [26].

General issues regarding an olivine-type phosphate include its low electronic conductivity of only approximately 10^{-8} S cm^{-1} compared to those of others such as $LiCoO_2$ (10^{-3} S cm^{-1}) and $LiMn_2O_4$ (10^{-5} S cm^{-1}). This is significantly lower than the other cathodes, and is likely due to the strong ionic bonding between the transition metals M and O as well as the isolation of valence electrons of the metal, resulting in low electronic conductivity of the olivine phosphate.

1-3-4. Current status and issues associated with cathode materials

A major challenge facing all cathode materials, including $LiCoO_2$, in practical use is low actual capacity. The performance of current lithium-ion batteries is largely limited by the cathode materials, representing the main obstacle that prevents increased capacity.

Lithium ion batteries using these transition metal oxides as cathode materials have already approached the theoretical limit [27], and it is considered difficult to further increase the size and capacity.

To further increase the capacity, it is conceivable to develop a material with a larger theoretical capacity, that is, a material containing a large amount of Li that contributes to charging and discharging. Figure 1-5 shows a potential roadmap for the development of improved cathode materials.

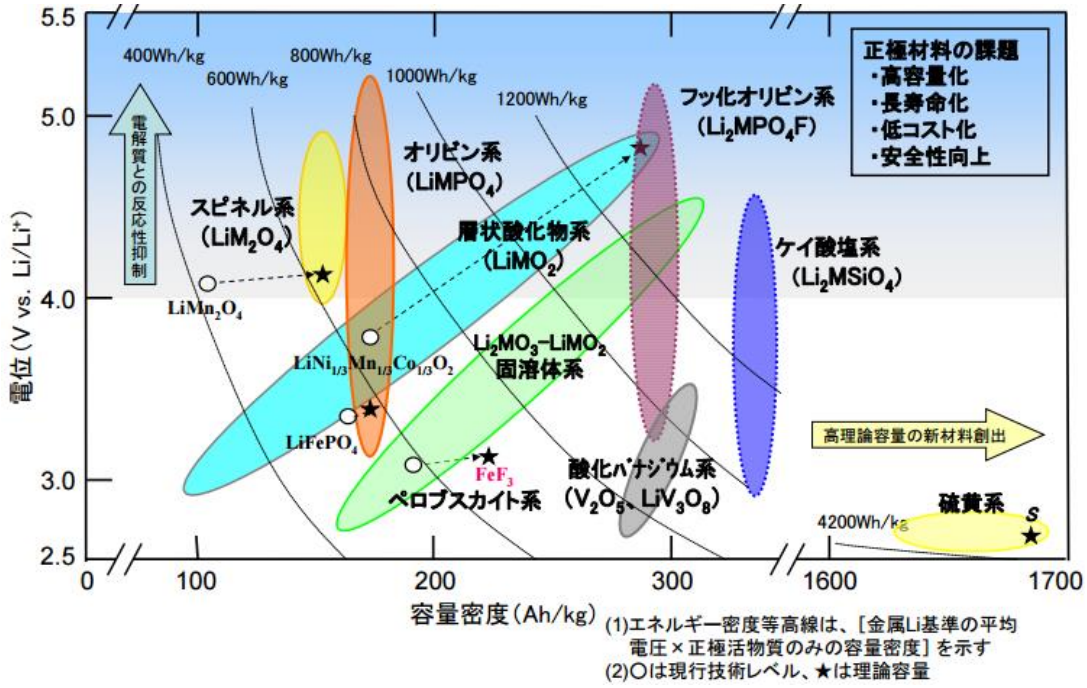

Figure 1-5. NEDO cathode material roadmap [28].

Examples of alternatives to layered oxide-based, spinel-based, and olivine-based cathode materials include Li-rich solid solution systems, vanadium oxide-based materials, and silicate-based materials. Although many vanadium oxide-based cathodes are capable of fast charge and discharge [29], their average potential is low (approximately 2.5 V) and energy density is not easily improved.

In addition, lithium-sulfur batteries are currently being studied as storage batteries with higher theoretical capacities, but many issues remain for their practical use, including the easy dissolution of sulfur in organic electrolytes [30].

Therefore, Li-rich cathode materials have attracted significant attention for increasing the energy density of lithium ion batteries.

1-4. Lithium-Rich Cathode Materials

1-4-1. Overview

Li-rich material, as the name suggests, is a material that contains an excessive amount of Li in the structure compared to the conventional materials. As a typical example, Figure 1-6 shows the structure of Li_2MnO_3, which is a layered rock salt type Li-rich material.

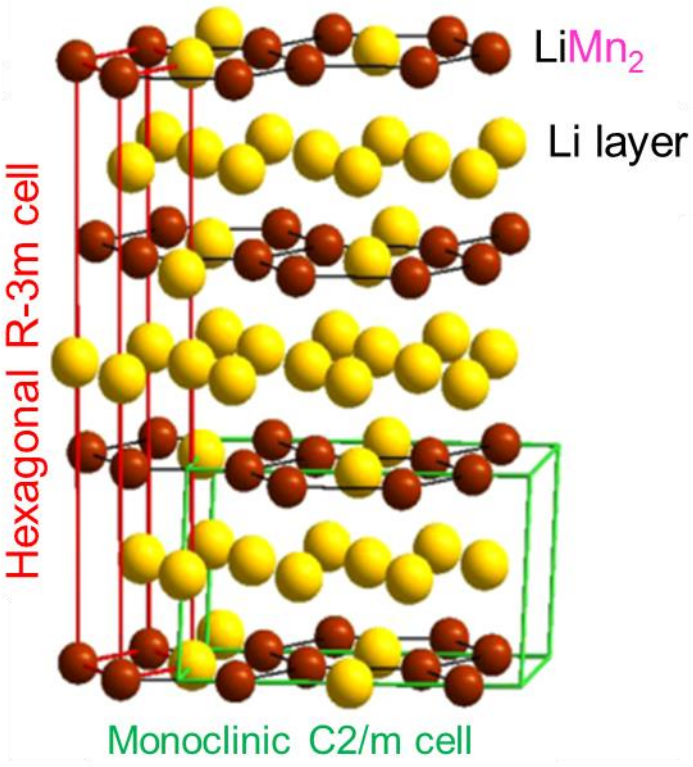

Figure 1-6. Structure of Li_2MnO_3.

The Li and transition metal layers are present, similar to conventional cathode materials, but the Li^+ is also present in the transition metal layer ($LiMn_2$ layer; Figure 1-6). The presence of excess Li^+ can greatly improve the theoretical capacity. For example, the theoretical capacity of Li_2MnO_3 is 458 mAh g^{-1}, assuming that all Li in Li_2MnO_3 can be desorbed. However, for materials that undergo intercalation, described in the previous section, oxidation of the transition metal is necessary for Li^+ elimination.

For Li_2MnO_3, the formal oxidation state of Mn is 4+, so it is considered impossible to desorb Li^+.

1-4-2. Li_2MnO_3

As mentioned previously, Mn^{4+} cannot be further oxidized and is electrochemically inactive. Therefore, Li_2MnO_3 is considered to be an inert phase that cannot easily electrochemically desorb Li^+, achieving a charge/discharge capacity of approximately 10 mAh g^{-1} even if the charge/discharge reaction is repeated at a potential range of ≤4 V.

Li_2MnO_3 has attracted significant attention because Bruce et al. revealed that an initial charge capacity of ≥300 mAh g^{-1} could be obtained by charging to ≥ 4.5 V [32,33]. Many reports regarding the associated reaction mechanism, including that by Yu et al., which noted the charge compensation by oxidation of Mn^{4+} to Mn^{5+} [34]. Kalyani reported that charge compensation was achieved by O^{2-} desorption and H^+ exchange reactions [35]. Koyama et al. reported that charge compensation by oxidation of oxygen occurs because high capacity cannot be achieved only by charge compensation by Mn oxidation [36].

However, the initial discharge capacity of Li_2MnO_3 is greatly reduced compared to the actual charge capacity [34] and has not been applied for practical use. Significant research efforts have been dedicated to clarifying the underlying mechanism and it is now believed that a reaction such as that described in Eq. (1.2) occurs with oxygen gas generation during the initial charge reaction [37].

$$Li_2MnO_3 \rightarrow 2Li^+ + 2e^- + MnO_2 + \frac{1}{2}O_2 \qquad (1.2)$$

Furthermore, this reaction occurs irreversibly and the cycle performance is deteriorated due to the phase transition from a layered rock salt-type structure to spinel-type structure.

1-4-3. Lithium-rich solid solution materials

Li_2MnO_3 has attracted great expectations for its high theoretical capacity, but the problem of poor cycle performance due to lack of structural stability remains a significant challenge. Thus, layered rock salt-type oxide cathode materials with a stable host structure, such as $LiCoO_2$, have attracted much attention since it was believed to be soluble in the electrolyte solution. Thus, research aimed at the realization of a material that combines the high capacity features of the excess cathode material and high stability and good cycle performances of the layered rock salt-type oxide cathode material has been reported.

Solid solution materials can be represented by $xLi_2M'O_3$- (1-x) LiM”O_2 (M' and M” are transition metals), which is a combination of a Li-excess cathode and layered rock salt-type oxide cathode. A large number of combinations exist for these materials that can be produced by replacing some of the transition metal of the layered rock salt-type oxide with another metal or application of a ternary system with the various solid solution ratios of x, M’, and M”. Dahn et al. reported materials containing Mn as a base for both transition metals M’ and M”, and replaced some of the M” on the layered oxide side with Ni, Co, Cr, etc., at various substitution ratios [38-48].

In these systems, assuming that all Li^+ can be desorbed, the theoretical capacity ranges from approximately 350 to 400 mAh g^{-1}, and as for Li_2MnO_3, a large capacity can be achieved by charging to ≥ 4.5 V, 300 mAh g^{-1} during the initial charge process. However, the initial discharge capacity decreases to approximately 150 to 250 mAh g^{-1}, and thereafter, the capacity gradually decreases while showing the same charge/discharge capacity. This is considered to be caused by the effect of oxygen desorption by the reaction described in Eq. (1.2) and local phase transitions [49]. In addition, it has been reported that polarization is very large at the end of the charge/discharge reaction, and the inactive Li_2MnO_3 component has been identified as a governing factor of rate performances [50]. Li_2MnO_3-based solid solution cathode materials often exhibit suppressed irreversible capacity at the first cycle compared to Li_2MnO_3 due to the effect of the solid solution of the layered oxide.

1-4-4. Li_2RuO_3

Li-rich cathode materials containing Mn have a higher theoretical capacity than layered rock-salt cathode materials, with the initial charge capacity typically exceeding 300 mAh g^{-1}, but generally lack reversible stability. This low stability is a significant barrier for practical use. Therefore, Li-rich cathodes containing other transition metals instead of inert Mn have been studied. A typical example is Li_2RuO_3, wherein Mn is replaced with the 4d transition metal Ru and Figure 1-7 shows the structure.

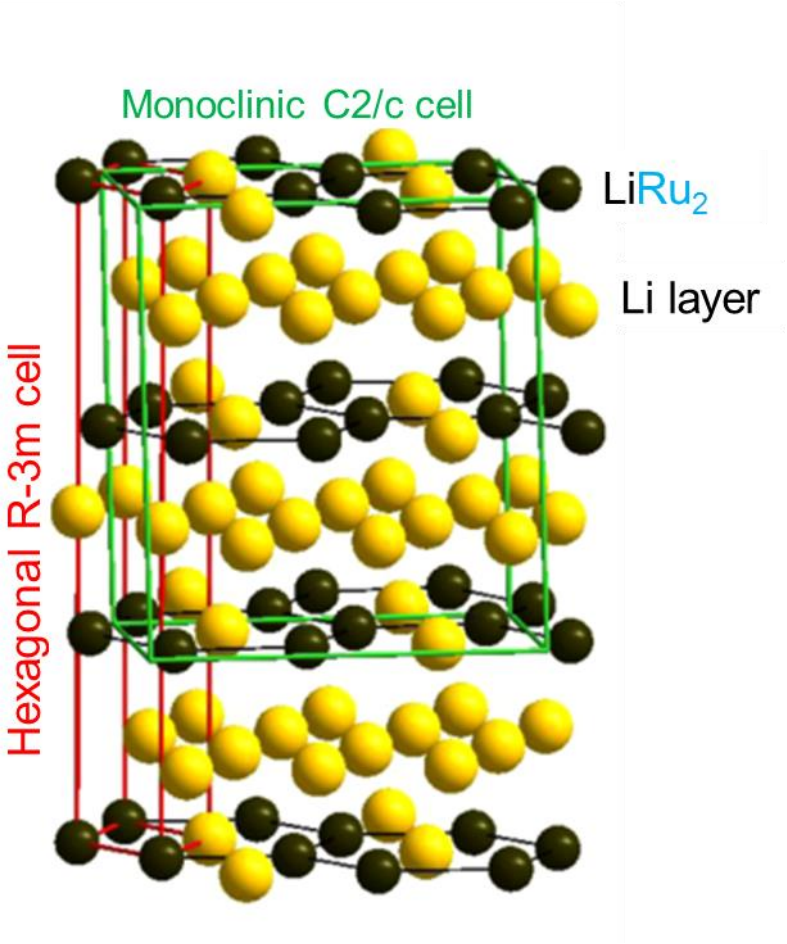

Figure 1-7. Structure of Li_2RuO_3 [31].

Similar to Li_2MnO_3, Li_2RuO_3 also contains excess Li^+ in the transition metal layer. The theoretical capacity of Li_2RuO_3, assuming that all Li^+ can be desorbed, is 328 mAh g^{-1}, which is small because the atomic weight of Ru is approximately twice that of Mn. A significant difference between Li_2RuO_3 and Li_2MnO_3 is that Li charge

elimination can be achieved by Ru oxidation. That is, during the charging process, reactions such as those described by Eqs. (1.3) and (1.4) can occur.

$$Li_2RuO_3 \rightarrow LiRuO_3 + Li^+ + e^- \qquad (1.3)$$

$$LiRuO_3 \rightarrow RuO_3 + Li^+ + e^- \qquad (1.4)$$

Because the reported capacity is approximately 250 to 280 mAh g^{-1}, the reaction described in Eq. (1.4) is not expected to proceed completely [51].

In addition, a major feature of Li_2RuO_3 is its lack of capacity reduction during discharge, as commonly observed in Mn-based materials. The initial discharge capacity has been reported to be approximately 250 to 280 mAh g^{-1}, with relatively good cycle performances [31,51-55].

Since Ru is a rare 4d transition metal, it is unsuitable as a practical material for widespread industrial use. Therefore, a material in which Ru is replaced with a more abundant element has been reported. Tarascon et al. reported a material in which some of the Ru is replaced with Mn, Sn, or Ti. [31,51,53,54].

1-4-5. Cation disordered-type materials

In addition to layered oxide cathode materials, the novel type of lithium-rich cathode materials with a cation disordered rock salt structure has been actively studied. For many years, rock salt structures were considered electrochemically inert [56-59]. When designing such materials, a route for Li diffusion in the bulk region is required. Because the electrostatic repulsive force greatly affects Li diffusion, the route must avoid high valence transition metals. To ensure such a route is formed in the electrode materials, the amount of transition metal must be reduced by adding excess Li. In the composition of $Li_{2-x}MO_2$, with excess Li but where $x < 1.0$, electrochemical activity is greatly increased [60-63].

These materials can be easily synthesized by mixing via mechanical energy input, such as ball milling. Yabuuchi et al. reported a novel cation disordered cathode material, $Li_{1.2}Ti_{0.4}Mn_{0.4}O_2$ [64], achieving >300 mAh g^{-1} during the 1st charge at 50 °C and a low

current rate, exhibiting a relatively reversible charge/discharge behavior. This material has the significant advantage of charge compensation of Mn^{3+} / Mn^{4+}, which is difficult to realize using layered oxide cathode materials.

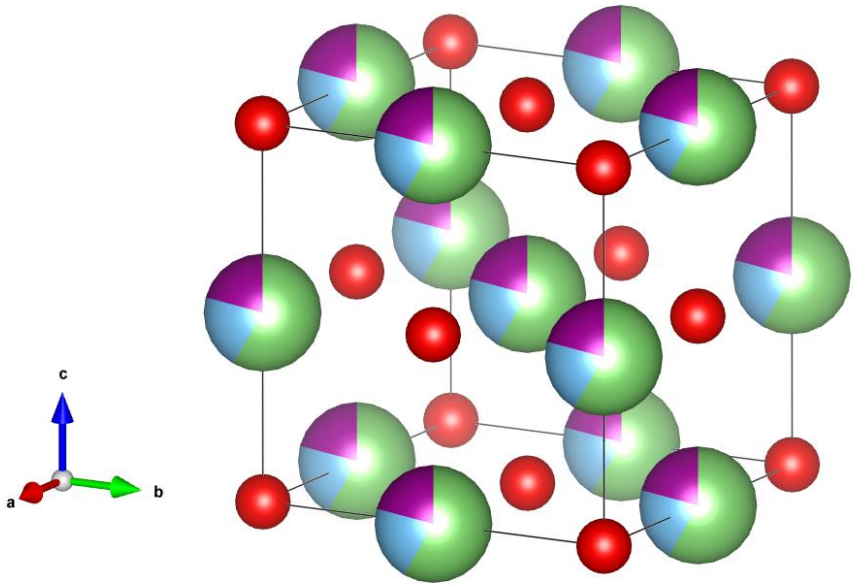

Figure 1-8. The general structure of cation disordered rock salt cathode materials.

Yabuuchi et al. also reported the same type of cathode containing other cation disordered rack salt cathode materials $Li_{1.3}Nb_{0.3}Mn_{0.4}O_2$ [61], $Li_{9/7}Nb_{2/7}Mo_{3/7}O_2$ [65], and so on to achieve high capacity by combined cationic and anionic redox. Lee et al. reported $Li_{(1+x)/100}Ni_{(1/2-x/120)}Ti_{(1/2-x/120)}Mo_{x/150}O_2$ [66] cathode materials that can utilize the Ni redox reaction more effectively. The authors tried to perform high-capacity charge compensation via redox reaction between Ni^{2+}/Ni^{4+}, but in rock-salt structures, the Ni redox reaction is limited between the 2+ and 3+ charge states.

In Li-excess materials, the proportion of the transition metal occupying the cation site decreases. Therefore, it is necessary to use anionic oxygen redox in addition to cation charge compensation to obtain a high capacity. However, if the amount of Li addition exceeds a critical value, the structure becomes unstable, causing oxygen desorption. To prevent this problem, the Li composition can be easily adjusted, but this decreases the availability of diffusion paths for Li, as shown in Figure 1-9 [67]. Therefore, an approach to solve these problems is urgently required.

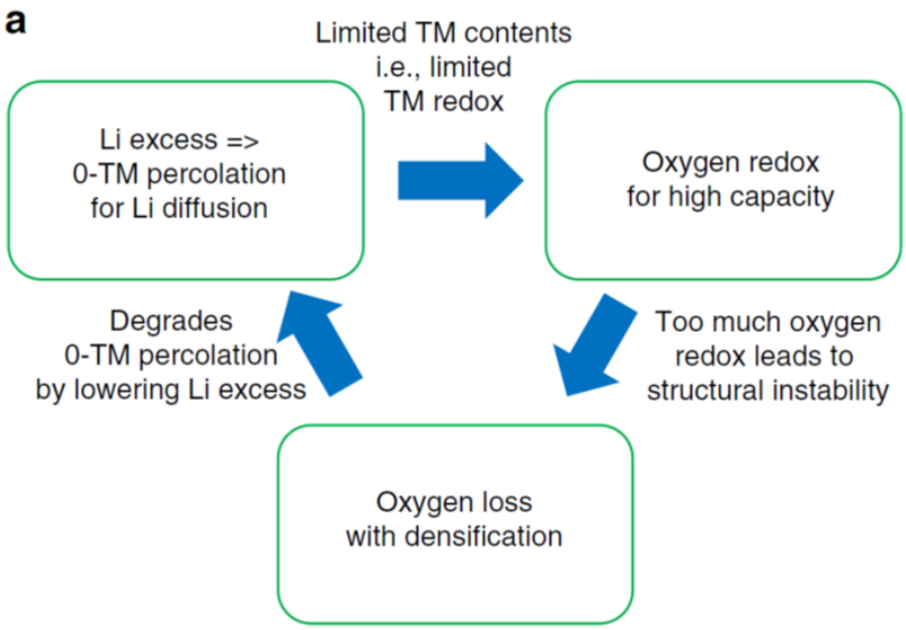

Figure 1-9. The challenges faced by cation-disordered cathode materials. [67]

1-5. Oxygen Redox and Electronic Structure Analysis

1-5-1. Anionic redox reaction

Many studies have been conducted regarding the factors that cause the irreversible behavior of Li_2MnO_3 materials and those that contribute to the high capacity and reversible charge/discharge capacity of Li_2RuO_3. Recently, the underlying mechanism has been considered from the viewpoint of electronic structure and Figures 1-10 and 1-11 show the density of states (DOS) of the representative Li_2MnO_3 and Li_2RuO_3.

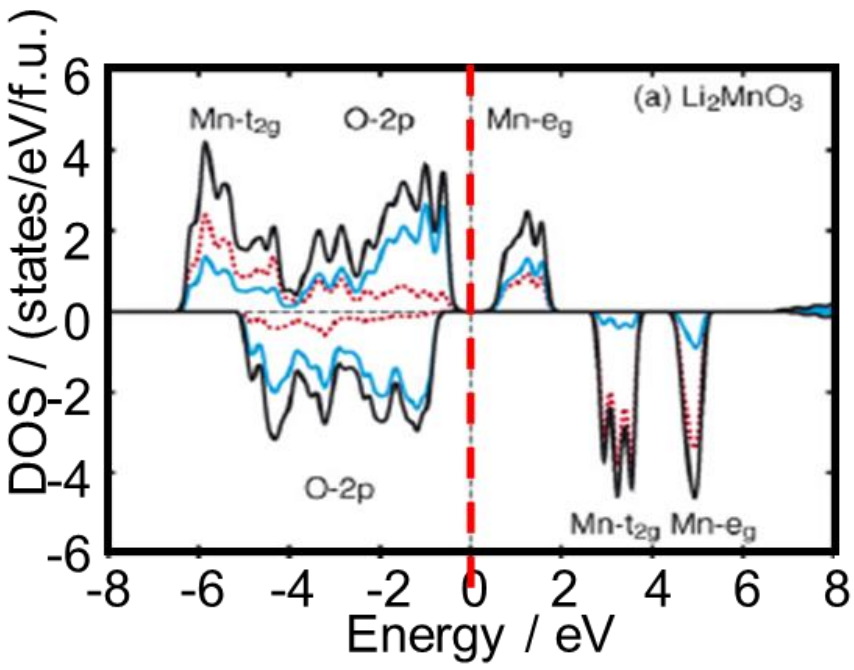

Figure 1-10. Li_2MnO_3 density of states function [36].

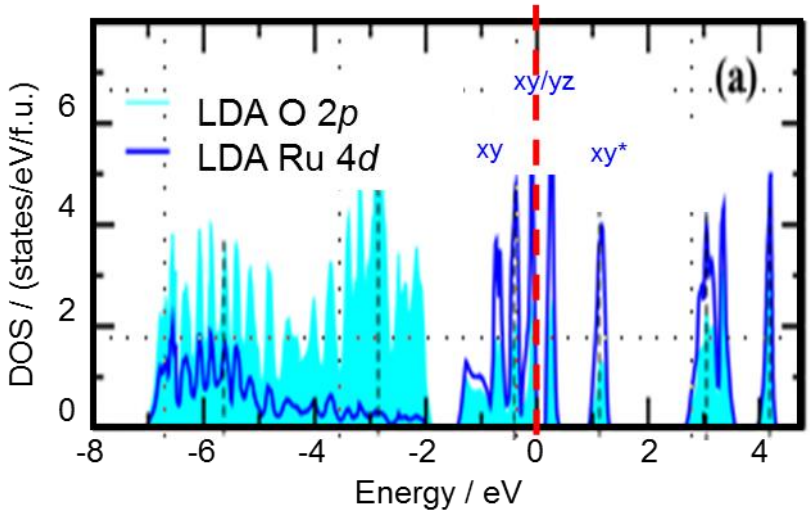

Figure 1-11. Li_2RuO_3 density of states function [68].

It is clear that the overlap between the Mn-3*d* and O-2*p* orbits is small near the Fermi level of Li_2MnO_3, as indicated by the red line in Figure 1-10. This reflects the weak hybridization between the transition metal and oxygen and low covalent bonding. Koyama et al. reported that charge compensation is achieved by desorbing electrons

from the O-2*p* orbital during Li desorption in Li_2MnO_3 charging and by desorption of oxygen, as described in Eq. (1.2) [36].

In contrast, in the vicinity of the Li_2RuO_3 Fermi level, as indicated by the red line in Figure 1-11, it is clear that a large overlap exists between the Ru-4*d* and O-2*p* orbitals. Thus, a hybrid orbital is created between Ru and O, resulting in highly covalent bonding. Tarascon et al. reported that during Li_2RuO_3 charging, the reaction described in Eq. (1.3) occurs initially, but the subsequent oxidation reaction of the anion (oxygen) occurs instead of Ru oxidation, and charge compensation for Li desorption is achieved [69]. The major difference between Li_2MnO_3 and solid solution materials based on Li_2MnO_3 is that oxygen desorption occurs at a higher potential region, whereas Li_2RuO_3 undergoes oxygen oxidation. Therefore, a difference in the degree of hybridization can be observed between the two materials.

Tarascon et al. used density functional theory (DFT) and DOS to reveal that an electronic structure that can stabilize oxygen holes during Li desorption would result in reversible charge/discharge and good cycle stability. For Li_2MnO_3, an irreversible reaction occurs due to the generation of oxygen, and for Li_2RuO_3, a reversible redox reaction occurs between the oxide (O^{2-}) and peroxide ions $(O_2)^{n-}$ [69].

Ceder et al. noted that a Li-rich cathode material exhibits a linear local structure of Li-O-Li because Li is also present in the transition metal layer. Because the energy of this Li-O-Li orbital is high and easily oxidized, the cathode material can effectively utilize the oxygen redox reaction as long as a local Li-O-Li structure is present [70]. In addition, Bruce et al. reported the experimental confirmation of oxygen gas generation originating from the cathode materials using mass spectrometry (MS) by replacing oxygen in the Mn-based solid solution material with ^{18}O. The authors suggested that oxygen generation could not be confirmed at ≤4.5 V, but oxygen gas was generated at ≥4.5 V. This oxygen did not originate from the decomposition of the electrolyte solution, but the oxygen present in the cathode materials [71].

Various reports describing differing interpretations of the oxygen redox reaction have been published and the associated research is ongoing. Application of the reversible oxygen redox reaction to high capacity expression is important for the future of cathode materials.

The charge compensation mechanism of cathode materials involves a complex reaction mechanism featuring a redox reaction of the cation (transition metal) and a redox reaction of the anion (oxygen). X-ray absorption spectroscopy (XAS) is an effective technique for analyzing the electronic structure and local structure changes of each element in the cathode materials. Conventionally, XAS has been used to observe changes in the valence of transition metals during the charge and discharge processes using hard X-rays. However, since oxygen greatly contributes to the charge/discharge process, the soft X-ray region including the *K* absorption edge of oxygen has attracted increasing attention. Oishi et al. analyzed the electronic structure of Li_2MnO_3 and Mn solid solutions using XAS in the soft X-ray region, demonstrating that oxygen contributed to charge compensation in the high potential region [72-74]. Yabuuchi et al. found that the lithium rich cathode materials $Li_{1.3}Nb_{0.3}Mn_{0.4}O_2$ and $Li_{1.42}Mo_{0.29}Fe_{0.29}O_2$ adopt a “superoxide state” that differs from conventional materials during charging, as determined by XAS measurements [75,76].

1-5-2. Challenges for anionic redox

The realization of a reversible anion redox reaction is indispensable for achieving a high capacity, which is characteristic of lithium-rich cathode materials. However, many problems remains for the effective use of anion redox, including the dependence of the reversible anion redox reaction proceeds on the electronic state in the material. Control of the electronic state remains difficult and electrode performance has been improved by approaches developed using both experimental and computational methods. However, research progress has not yet reached a decisive point where the electronic state can be precisely controlled.

Another challenge involves the anion redox reaction itself. In the charge compensation mechanism of lithium-rich cathodes, both cations and anions contribute to the redox reaction, but the anion redox reaction is a kinetically slower reaction [54,77]. Li et al. suggested that Li^+ diffusion coefficients in the plateau region (i.e. at higher voltage) of the first charge are very small, which were attributed to the high kinetic barriers associated with the concurrent Li^+ extraction, oxygen loss, and structural rearrangement [77]. Therefore, the lithium-rich cathode materials that undergo an anion

redox reaction generally exhibit low rate performance, and are not suitable for high-speed charge/discharge, which is important for practical use.

1-5-3. Anionic doping of lithium-rich cathode materials

This chapter has reviewed many previously reported lithium-rich cathodes, which have been commonly improved by changing the kind of cation in the metal oxide or changing the cation composition. By cationic substitution, the electronic state of the cathode materials can be drastically changed. However, the cation-substitution methods realized by changing the species or the ratio of transition metals in lithium-rich cathode materials described above still suffer from the sluggish kinetics of the anion redox reaction, voltage hysteresis, poor rate capability, and voltage fading [54].

Recently, the stabilization of anion redox and the use of transition metal redox instead of anion redox have been investigated. A promising approach involves anionic substitution for lithium-rich cathode materials instead of cationic substitution. Using anionic substitution, the electronic state of the cathode materials can be drastically changed, similar to cationic substitution. Generally, since cathode materials are composed of metal oxides, in anion substitution oxygen is substituted with another anion. Thus, it is natural to consider a material that substituted some oxygen with fluorine. Recently, anionic substitution by fluorine-doping has been reported [67, 78-82], and since oxygen is substituted with fluorine, it is necessary to use a transition metal with a lower valence to maintain the charge balance in the crystal. By partially reducing the constituent transition metal, the valence can be decreased to improve the cationic redox capacity. For example, Horse et al. synthesized Li_2MnO_2F in which some O in Li_2MnO_3 was replaced with F. In this material, the valence of Mn is primarily trivalent, so that the capacity can be obtained from the redox reaction of Mn^{3+} / Mn^{4+} [78].

Even when fluorine substitution is performed, no significant difference in the theoretical capacity is observed, so the ratio of charge compensation by the transition metal redox increases while the contribution of oxygen redox to the charge compensation decreases.

With fluorination as a new degree of freedom to tune and mix the average anion and cation valence, the rational design of lithium rich cation-disordered cathodes has become increasingly complex. Therefore, to design novel cathode materials, careful

balance between the lithium excess and transition metal content, as well as consideration of the feasibility of fluorination and synthesis temperature are required [83, 84].

Another alternative anion substitution method is the replacement of oxygen with nitrogen, and several nitrogen doping techniques for lithium-rich cathode materials have been reported [85-87]. Binder et al. suggested that the existence of nitrogen in the surface layer contributed to lithium diffusion acceleration, as the nitrogen-doped lithium-rich cathode exhibited improved rate capabilities and suppressed the voltage fading [85]. The nitrogen doping examples reported to date have been limited to surface treatments, and the detailed reaction mechanism has not yet been clarified. In addition, when nitrogen substitution is performed using the same approach as fluorine substitution, the transition metal remains in a highly oxidized state to maintain the charge balance. In addition, since the 2*p* orbital of nitrogen is closer to the Fermi level than that of oxygen, the presence of nitrogen may result in a new anion redox mechanism. Therefore, the nitrogen substitution approach can stabilize the oxygen redox reaction, leading to a higher capacity. The development of novel cathode materials by anion substitution remains in its infancy and is a desirable field where further development is expected.

1-6. Next Generation Batteries

Cathode material development for further applications of lithium ion batteries has been described with specific examples in previous sections. Research regarding the practical application of next-generation storage batteries to large-scale applications is not limited to lithium-ion batteries, and some other types will be briefly mentioned in this section.

A typical example of a next-generation battery is the sodium ion battery that uses monovalent ion similar to lithium. The great advantage of sodium is that it is superior to lithium in terms of abundance and cost. In addition, a number of materials can be adopted for use as sodium-based materials, in sharp contrast to lithium-based materials [88]. For example, $Na_{2/3}[Fe_{1/2}Mn_{1/2}]O_2$ reported by Yabuuchi et al. is a layered oxide, but unlike a general Li-based layered oxide, the space group was assigned as P2 [88]. In

addition, sodium has a lower Lewis acidity than lithium, reducing its desolvation activation energy and accelerating the interface reaction [89].

However, the ionic radius and atomic weight of sodium are larger than those of lithium, resulting in decreased theoretical capacity. Furthermore, since the standard electrode potential of sodium is approximately 0.3 V higher than that of lithium, it is impossible to construct a system with a voltage higher than that of a lithium system with the same material configuration.

If divalent ions can be used as charge carriers, charge storage can be performed more efficiently than for monovalent ions such as lithium and sodium. To take advantage of divalent ions, the adoption of magnesium and calcium over lithium has been considered. The magnesium ion batteries have attracted significant attention as they are less flammable and explosive than lithium ion batteries and are currently being developed as safe storage batteries.

Many reports of candidates for cathode materials for magnesium ion batteries have been published. However, because magnesium is a divalent ion, the Coulomb interaction in the solid is stronger than for lithium, and it is difficult to insert magnesium into the host material. Another problem restricting the development of these batteries is the slow diffusion of magnesium ions in the host material [90].

Moreover, divalent ions exhibit strong Lewis acidity, complicating the design of electrolytes due to problems associated with achieving a stable solvation state [91]. In addition, magnesium metal reacts with many organic electrolytes, passivating its surface and preventing the precipitation dissolution reaction at the anode. Conventionally, Grignard reagents have been used as electrolytes, but other systems that cause magnesium precipitation and dissolution have been developed. Shiraga et al. succeeded in achieving the magnesium precipitation dissolution reaction with high coulombic efficiency using an electrolytic solution containing magnesium bromide dissolved in 2-methyl-tetrahydrofuran (2-MeTHF) [92].

In addition to these systems, lithium-sulfur batteries using multi-electron reactions with polysulfides as an intermediate during the sulfur reduction reaction have been developed. A lithium-air battery wherein lithium metal is arranged as the anode has also attracted significant attention. Moreover, the anode materials, electrolytes, additives,

and binders used in lithium ion batteries are constantly being improved. Advances in strategies aimed at developing high performance batteries by using abundant general-purpose elements are required. Therefore, deep insight based on crystal structure analysis and electronic structure analysis of various materials, understanding of functionalization based on these insights, and a wide range of seamless approaches must be developed to achieve morphological control and compounding of materials for use in next-generation batteries.

1-7. Outline of the Present Thesis

The present thesis consists of seven chapters that are focused on the crystal and electronic structures of cathode materials for the development of next-generation batteries.

In Chapter 1, the formation of storage batteries and current issues are reviewed, mainly focusing on lithium-ion batteries. Because the application of lithium-ion batteries to large-scale applications is hindered by the low capacity of cathode materials, the development of novel high capacity cathode materials is urgently needed, and other types of next-generation storage batteries are briefly introduced.

In Chapter 2, the monoclinic lithium-rich Li_2TiO_3 and Li_2RuO_3 crystal structural analysis were performed. Recently, many reports regarding lithium-rich cathode materials have been published, but their precise crystal structure remains largely unknown. In this chapter, precise analysis considering stacking faults and cation mixing was performed to determine basic crystallographic information for revealing the correlations between the Li-rich materials structures and the differences of Li^+ diffusion path mechanism.

In Chapter 3, magnesium batteries are investigated as next-generation battery systems. Using intercalation-type cathodes similar to those of lithium ion batteries, the performance of the magnesium battery can be greatly improved. In this chapter, the mechanism of magnesium insertion/extraction using the olivine-type $FePO_4$ system as a host structure was investigated.

In Chapter 4, a solid solution material using the 4d transition metal Ru was synthesized. Subsequently, with respect to conventional solid solution materials

containing Mn, the rate performance and reversibility of anion redox when using a 4d transition metal will be compared.

In Chapters 5 and 6, nitrogen substitution was performed in bulk cation disordered Ti-Mn lithium-rich cathode materials. By performing nitrogen substitution in a relatively stable system, high capacity, improved rate performance, and changing charge compensation mechanisms including anion redox were achieved and have been discussed in detail.

In Chapter 7, the general conclusion summarizes the present studies and prospects of future cathode materials for use in next-generation batteries.

1-8. References

[1] 「電池ハンドブック」, 電気化学会, 電池技術委員会【編】, オーム社

[2] 「エンジニアのための電気化学」, 林 茂雄 著, コロナ社

[3] 国土交通省　平成 27 年度全国都市交通特性調査

[4] JR 東日本資料「蓄電池駆動電車(EV-E301 系)」

[5] 「地方消滅　東京一極集中が招く人口急減」, 増田寛也編著, 中央公論新社刊

[6] J.B. Goodenough and K. S. Park, "The Li-ion rechargeable battery: a perspective." *J. Am. Chem. Soc.* **135**, 1167-1176, (2013).

[7] J.N Reimers and J.R. Dahn, "Electrochemical and In Situ X-Ray Diffraction Studies of Lithium Intercalation in Li_xCoO_2." *J. Electrochem. Soc.* **139**, 2091-2097, (1992).

[8] C. Delmas, "Alkali metal intercalation in layered oxides." *Mater. Sci. Eng.* **B3**, 97-101, (1989).

[9] J. N. Reimers, W. Li, E. Rossen and J.R. Dahn, "MRS Sympo. Proc., Vol. 293(Ed. G.-A. Nazn, J. M Tarason, M. Armand)*"* p.3, *MRS* (1993).

[10] R. Kanno, H. Kubo,Y. Kawamoto, T. Kamiyama, F. Izumi, Y. Takeda and M. Takano, "Phase Relationship and Lithium Deintercalation in Lithium Nickel Oxides." *J. Soid State Chem.* **110**, 216-225, (1994).

[11] C. Delmas and I. Saadonne, "Electrochemical and physical properties of the $Li_xNi_{1-y}Co_yO_2$ phases." *Solid State Ionics*. **53-56**, 370-375 (1992).

[12] G. Dutta, A. Manthiram, J.B. Goodenough and J-C. Greinier, "Chemical synthesis and properties of $Li_{1-\delta-x}Ni_{1+\delta}O_2$ and $Li[Ni_2]O_4$," *J.Solid State Chem.* **96,** 123-131, (1992).

[13] K. Takeda, N. Aotani, K. Iwamoto and S. Kondo, "Electrochemical behavior of Li_xMO_2 (M = Co, Ni) in all solid state cells using a glass electrolyte." *Solid State Ionics*. **79**, 284-287, (1995).

[14] T. Ohzuku, Y. Makimura, "Layered Lithium Insertion Material of $LiNi_{1/2}Mn_{1/2}O_2$: A Possible Alternative to $LiCoO_2$ for Advanced Lithium-Ion Batteries." *Chem. Lett.* **30**, 744-745, (2001).

[15] S-T. Myung, K. Amine and Y-K. Sun, "Surface modification of cathode

materials from nano- to microscale for rechargeable lithium-ion batteries." *J. Mater. Chem.* **20**, 7074-7095, (2010).

[16] T. Ohzuku and Y. Makimura, "Layered Lithium Insertion Material of $LiCo_{1/3}Ni_{1/3}Mn_{1/3}O_2$ for Lithium-Ion Batteries," *Chem. Lett.,* **30**, 642-643, (2001).

[17] S. Yajima, S. Miyamoto and R. Nishikawa, *J. Mater. Sci. Soc.Japan.* **34**, 230 (1997).

[18] Y. Xia, Y. Zhou and M. Yoshio, "Capacity Fading on Cycling of 4 V Li / $LiMn_2O_4$ Cells." *J. Electrochem. Soc.* **144**, 2593-2600, (1997).

[19] J. Gummow, A. de Kock and M. M. Thackeray, "Improved capacity retention in rechargeable 4 V lithium/lithium-manganese oxide (spinel) cells." *Solid State Ionics.* **69**, 59-67, (1994).

[20] M. Wakihara, L. Guohua, K. Sakuma, H. Ikuta and T. Uchida, *Proceedings of the symposium on rechargeable lithium and lithium-ion batteries(186th Meeting of the electrochemical society, Miami Beach, Florida)*. **53**, 9 (1994)

[21] M. Kaneko, S. Matsuno, T. Miki, M. Nakayama, H. Ikuta, Y. Uchimoto, M. Wakihara and K. Kawamura, "Local Structural Studies of $LiCr_yMn_{2-y}O_4$ Cathode Materials for Li-Ion Batteries." *J. Phys. Chem. B.* **107**, 1727-1733, (2003).

[22] R. Alcantara, M. Jaraba, P. Lavela, J. L. Tirado, "Optimizing preparation conditions for 5 V electrode performance, and structural changes in $Li_{1-x}Ni_{0.5}Mn_{1.5}O_4$ spinel." *Electrochim. Acta.* **47**, 1829-1835, (2002).

[23] H. Kawai, M. Nagata, H. Kageyama, H. Tsukamoto and A. R. West, "5 V lithium cathodes based on spinel solid solutions $Li_2Co_{1+X}Mn_{3-X}O_8$: $-1 \leq X \leq 1$," *Electrochim. Acta.* **45**, 315, (1999).

[24] A. K. Padhi, K. S. Nanjundaswamy and J. B. Goodenough, "Phospho-olivines as Positive-Electrode Materials for Rechargeable Lithium Batteries." *J. Electrochem. Soc.* **144**, 1188-1194, (1997).

[25] A. Yamada, S.C. Chung and K. Hinokuma, "Optimized $LiFePO_4$ for Lithium Battery Cathodes." *J. Electrochem. Soc.*, **148,** A224-A229, (2001).

[26] A. Yamada, H. Koizumi, S. Nishimura, N. Sonoyama, R. Kanno, M.

Yonemura, T. Nakamura and Y. Kobayashi, “Room-temperature miscibility gap in Li_xFePO_4.” *Nat. Mater.* **5**, 357-360, (2006).

[27] H. Wang, L.-F. Cui, Y. Yang, H. S. Casalongue, J. T. Robinson, Y. Liang, Y. Cui, and H. Dai, “Mn_3O_4-Graphene Hybrid as a High-Capacity Anode Material for Lithium Ion Batteries.” *J. Am. Chem. Soc.*, **132**, 13978-13980, (2010).

[28] 国立研究開発法人新エネルギー・産業技術総合開発機構(NEDO)「ＮＥＤＯ次世代自動車用蓄電池技術開発ロードマップ 2008」

[29] S. Yang, Y. Gong, Z. Liu, L. Zhan, D. P. Hashim, L. Ma, R. Vajtai and P. M. Ajayan, “Bottom-up Approach toward Single-Crystalline VO_2-Graphene Ribbons as Cathodes for Ultrafast Lithium Storage.” *Nano Lett.* **13**, 1596-1601, (2013).

[30] P. G. Bruce, F. A. Freunberger, L. J.Hardwick and J-M Tarascon, “Li-O_2 and Li-S batteries with high energy storage.” *Nat.Mater.* **11**, 19-29, (2012).

[31] M. Sathiya, K. Ramesha, G. Rousse, D. Foix, D. Gonbeau, A. S. Prakash, M. L. Doublet, K. Hemalatha and J.-M. Tarascon, “High Performance $Li_2Ru_{1-y}Mn_yO_3$ ($0.2 \leq y \leq 0.8$) Cathode Materials for Rechargeable Lithium-Ion Batteries: Their Understanding,” *Chem. Mater.*, **25,** 1121-1131, (2013).

[32] A. D. Robertson and P. G. Bruce, “Mechanism of Electrochemical Activity in Li_2MnO_3.” *Chem. Mater.*, **15**, 1984-1992, (2003).

[33] A. D. Robertson and P. G. Bruce, “The origin of electrochemical activity in Li_2MnO_3,” *Chem. Commun.*, **23**, 2790-2791, (2002).

[34] D. Y. W. Yu, K. Yanagida, Y. Kato and H. Nakamura, “Electrochemical Activities in Li_2MnO_3.” *J. Electrochem. Soc.* **156**, A417-A424, (2009).

[35] P. Kalyani, S. Chitra, T. Mohan and S. Gopukumar, “Lithium metal rechargeable cells using Li_2MnO_3 as the positive electrode.” *J. Power Sources.* **80**, 103-106, (1999).

[36] Y. Koyama, I. Tanaka, M. Nagao and R. Kanno, “First-principles study on lithium removal from Li_2MnO_3,” *J. Power Sources.* **189**, 798-801, (2009).

[37] H.Chen and M.S. Islam, “Lithium Extraction Mechanism in Li-Rich Li_2MnO_3 Involving Oxygen Hole Formation and Dimerization.” *Chem. Mater.* **28**,

6656-6663, (2016).

[38] Z. Lu and J.R. Dahn, "Layered Cathode Materials Li $[NixLi_{(1/3-2x/3)}Mn_{(2/3-x/3)}]O_2$ for Lithium-Ion Batteries." *Electrochem. Solid. St.*, **4**, A191-A194, (2001).

[39] Z. Lu and J.R. Dahn, "Layered Li $[Ni_xCo_{1-2x}Mn_x]O_2$ Cathode Materials for Lithium-Ion Batteries." *Electrochem. Solid. St.* **4**, A200-A203, (2001).

[40] Z. Lu and J.R. Dahn, "Synthesis, Structure, and Electrochemical Behavior of Li $[Ni_xLi_{1/3-2x/3}Mn_{2/3-x/3}]O_2$." *J. Electrochem. Soc.* **149**, A778-A791, (2002).

[41] Z. Lu and J.R. Dahn, "Understanding the Anomalous Capacity of Li / $Li[NixLi_{(1/3-2x/3)}Mn_{(2/3-x/3)}]O_2$ Cells Using *In Situ* X-Ray Diffraction and Electrochemical Studies." *J. Electrochem. Soc.* **149**, A815-A822, (2002).

[42] Z. Lu and J.R. Dahn, "Structure and Electrochemistry of Layered $Li[Cr_xLi_{(1/3-x/3)}Mn_{(2/3-2x/3)}]O_2$." *J. Electrochem. Soc.* **149**, A1454-A1459, (2002).

[43] Z. Lu, Z. Chen, J.R. Dahn, "Preparation, structure, and thermal stability of new $Ni_xCo_{1-2x}Mn_x(OH)_2$ $(0 \leq x \leq 1/2)$ phases," *Chem.Mater.*, **15**, 495-499 (2003).

[44] Z. Lu, Z. Chen and J.R. Dahn, "Lack of Cation Clustering in $Li[Ni_xLi_{1/3-2x/3}Mn_{2/3-x/3}]O_2$ $(0 < x \leq 1/2)$ and $Li[Cr_xLi_{(1-x)/3}Mn_{(2-2x)/3}]O_2$ $(0 < x < 1)$." *Chem.Mater.* **15**, 3214, (2003).

[45] S. Jouanneau, K.W. Eberman, L.J. Krause and J.R. Dahn, "Synthesis, Characterization, and Electrochemical Behavior of Improved $Li[Ni_xCo_{1-2x}Mn_x]O_2$ $(0.1 \leqslant x \leqslant 0.5)$." *J. Electrochem. Soc.* **150**, A1637-A1642, (2003).

[46] S. Jouanneau, W. Bahmet, K.W. Eberman and L.J. Krause, "Effect of the Sintering Agent, B_2O_3, on $Li[Ni_xCo_{1-2x}Mn_x]O_2$ Materials Density, Structure, and Electrochemical Properties." *J. Electrochem. Soc.* **151**, A1789-A1796, (2004).

[47] S. Jouanneau and J.R. Dahn, "Morphology and Safety of $Li[Ni_xCo_{1-2x}Mn_x]O_2$ $(0 \leqslant x \leqslant 1/2)$." *J. Electrochem. Soc.* **151**, A1749 (2003).

[48] E. McCalla, C. M. Lowartz, C. R. Brown and J. R. Dahn, "Formation of

Layered–Layered Composites in the Li–Co–Mn Oxide Pseudoternary System during Slow Cooling." *Chem.Mater.* **25**, 912 (2013).

[49] A.R. Armstrong, M. Holzapfel, P. Novak, C.S. Johnson, S.-H. Kang, M.M. Thackeray and P.G. Bruce, "Demonstrating oxygen loss and associated structural reorganization in the lithium battery cathode $Li[Ni_{0.2}Li_{0.2}Mn_{0.6}]O_2$." *J. Am. Chem. Soc.* **128**, 8694-8698, (2008).

[50] H. Yu, Y. Wang, D. Asakura, E. Hosono, T.Zhang and H. Zhou, "Electrochemical kinetics of the $0.5Li_2MnO_3$-$0.5LiMn_{0.42}Ni_{0.42}Co_{0.16}O_2$ 'composite' layered cathode material for lithium-ion batteries." *RSC Adv*. **2**, 8797–8807 (2012).

[51] D. Mori, H. Kobayashi, T. Okumura, H. Nitani, M. Ogawa and Y. Inaguma, "XRD and XAFS study on structure and cation valence state of layered ruthenium oxide electrodes, Li_2RuO_3 and $Li_2Mn_{0.4}Ru_{0.6}O_3$, upon electrochemical cycling." *Solid State Ionics*, **285**, 66-74, (2016).

[52] Y. Yao, P. Yang, X. Bie, C. Wang, Y. Wei, G. Chen, F. Du, "High capacity and rate capability of a layered Li_2RuO_3 cathode utilized in hybrid Na^+/Li^+ batteries." *J. Mater. Chem*. *A.* **3**, 18273-18278, (2015).

[53] M. Sathiya, A.M. Abakumov, D. Foix, G. Rousse, K. Ramesha, M. Saubanere, M. L. Doublet, H. Vezin, C.P. Laisa, A.S. Prakash, D. Gonbeau, G. VanTendeloo and J-M. Tarascon, "Origin of voltage decay in high-capacity layered oxide electrodes." *Nat. Mater.*, **14**, 230-238, (2015).

[54] G. Assat, C. Deacourt, D. A. D. Corte and J-M. Tarascon, "Practical Assessment of Anionic Redox in Li-Rich Layered Oxide Cathodes: A Mixed Blessing for High Energy Li-Ion Batteries." *J. Electrochem. Soc.* **163**, A2965-A2976, (2016).

[55] B. Li, R. Shao, H. Yan, L. An, B. Zhang, H. Wei, J. Ma, D. Xia and X. Han, "Understanding the Stability for Li-Rich Layered Oxide Li_2RuO_3 Cathode." *Adv. Funct. Mater.* **26**, 1330-1337, (2016).

[56] K. Kang, D. Carlier, J. Reed, E. M. Arroyo, G. Ceder, L. Croguennec and C. Delmas, "Synthesis and Electrochemical Properties of Layered $Li_{0.9}Ni_{0.45}Ti_{0.55}O_2$." *Chem. Mater.* **15**, 4503-4507, (2003).

[57] Y. Sakurai, H. Arai and J. Yamaki, “Preparation of electrochemically active α-$LiFeO_2$ at low temperature” *Solid State Ionics.* **113-115**, 29-34, (1998).

[58] M. N. Obrovac, O. Mao and J. R. Dahn, “Structure and electrochemistry of $LiMO_2$ (M=Ti, Mn, Fe, Co, Ni) prepared by mechanochemical synthesis.” *Solid State Ionics*, **112**, 9-19, (1998).

[59] K. Ozawa, Y. Nakao, L. Wang, Z. Cheng, H. Fujii, M. Hase and M. Eguchi, “Structural modifications caused by electrochemical lithium extraction for two types of layered $LiVO_2$.” *J. Power Sources*. **174**, 469-472, (2007).

[60] J. Lee, A. Urban, X. Li, D. Su, G. Hautier and G. Ceder, “Unlocking the Potential of Cation-Disordered Oxides for Rechargeable Lithium Batteries.” *Science*, **343**, 519-522, (2014).

[61] N. Yabuuchi, M. Takeuchi, M. Nakayama, H. Shiiba, M. Ogawa, K. Nakayama, T. Ohta, D. Endo, T. Ozaki, T. Inamasu, K. Sato and S. Komaba, “High-capacity electrode materials for rechargeable lithium batteries: Li_3NbO_4-based system with cation-disordered rocksalt structure.” *Proc. Natl. Acad. Sci. U. S. A.*, **112**, 7650-7655, (2015).

[62] R. Chen, S. Ren, M. Yavuz, A. A. Guda, V. Shapovalov, R. Witter, M. Fichtner and H. Han, “Li^+ intercalation in isostructural Li_2VO_3 and Li_2VO_2F with O_2 and mixed O_2/F anions.” *Phys. Chem. Chem. Phys.*, **17**, 17288-17295, (2015).

[63] S. Ren, R. Chen, E. Maawad, O. Dolotko, A. A. Guda, V. Shapovalov, D. Wang, H. Hahn and M. Fichtner, “Improved Voltage and Cycling for Li^+ Intercalation in High-Capacity Disordered Oxyfluoride Cathodes.” *Adv. Sci.* **2**, 1500128, (2015).

[64] N. Yabuuchi, M. Nakayama, M. Takeuchi, S. Komaba, Y. Hashimoto, T. Mukai, H. Shiiba, K. Sato, Y. Kobayashi, A. Nakao, M. Yonemura, K. Yamanaka, K. Mitsuhara and T. Ohta, “Origin of stabilization and destabilization in solid-state redox reaction of oxide ions for lithium-ion batteries.” *Nat. Commn.* **7**, 13814, (2016).

[65] S. Hoshino, A. M. Glushenkov, S. Ichikawa, T. Ozaki, T. Inamasu and N. Yabuuchi, “Reversible Three-Electron Redox Reaction of Mo^{3+}/Mo^{6+} for Rechargeable Lithium Batteries.” *ACS Energy Lett.* **2**, 733-738, (2017).

[66] J. Lee, D-H. Seo, M. Balasubramanian, N. Twu, X. Li and G. Ceder, “A new class of high capacity cation-disordered oxides for rechargeable lithium batteries: Li–Ni–Ti–Mo oxides.” *Energy Environ. Sci.* **8**, 3255-3265, (2015).

[67] J. Lee, J. K. Papp, R. J. Clément, S. Sallis, D-H. Kwon, T. Shi, W. Yang, B. D. McCloskey and G. Ceder, “Mitigating oxygen loss to improve the cycling performance of high capacity cation-disordered cathode materials.” *Nat. Commun.* **8**, 891, (2017).

[68] Z. V. Pchelkina, A. L. Pitman, A. Moewes, E. Z. Kurmaev, T-Y. Tan, D. C. Peets, J-G. Park, S. V. Streltsov, “Electronic structure of Li_2RuO_3 studied by LDA and LDA+DMFT calculations and soft x-ray spectroscopy,” *Phys. Rev. B,* **91**, 115-138 (2015).

[69] M. Saubanere, E. McCalla, J-M. Tarascon, M.-L. Doublet, “The intriguing question of anionic redox in high-energy density cathodes for Li-ion batteries,” *Energy Environ. Sci.*, **9**, 984-991 (2016).

[70] G. Ceder, “Combining Reversible Oxygen Charge Transfer and Li-Excess to achieve High Capacity Cathodes,” *18th International Meeting on Lithium Batteries*, June 22 (2016).

[71] K. Luo, M. R. Roberts, R. Hao, N. Guerrini, D. M. Pickup, Y-S. Liu, K. Edstrom, J. Guo, A. V. Chadwick, L. C. Duda and P. G. Bruce, “Charge-compensation in 3d-transition-metal-oxide intercalation cathodes through the generation of localized electron holes on oxygen.” *Nat. Chem.* **8**, 684-691, (2016).

[72] M. Oishi, K.Yamanaka, I.Watanabe, K.Shimoda, T. Matsunaga, H. Arai, Y. Ukyo, Y. Uchimoto, Z. Ogumi and T. Ohta, “Direct observation of reversible oxygen anion redox reaction in Li-rich manganese oxide, Li_2MnO_3, studied by soft X-ray absorption spectroscopy.” *J. Mater. Chem. A.* **4**, 9293-9302 (2016).

[73] M. Oishi, C.Yogi, I. Watanabe, T.Ohta, Y. Orikasa, Y. Uchimoto and Z. Ogumi, “Direct observation of reversible charge compensation by oxygen ion in Li-rich manganese layered oxide positive electrode material, $Li_{1.16}Ni_{0.15}Co_{0.19}Mn_{0.50}O_2$.” *J. Power. Sources.* **276**, 89-94, (2015).

[74] M. Oishi, T. Fujimoto, Y. Takanashi, Y. Orikasa, A. Kawamura, T. Ina, H.

Yamashige, D. Takamatsu, K. Sato, H. Murayama, H. Tanida, H. Arai, H. Ishii, C. Yogi, I. Watanabe, T. Ohta, A. Mineshige, Y. Uchimoto and Z. Ogumi, "Charge compensation mechanisms in $Li_{1.16}Ni_{0.15}Co_{0.19}Mn_{0.50}O_2$ positive electrode material for Li-ion batteries analyzed by a combination of hard and soft X-ray absorption near edge structure." *J. Power. Sources.* **222**, 45-51, (2013).

[75] T. Matsuhara, Y. Tsuchiya, K. Yamanaka, K. Mitsuhara, T. Ohta and N. Yabuuchi, "Synthesis and Electrode Performance of Li_4MoO_5-$LiFeO_2$ Binary System as Positive Electrode Materials for Rechargeable Lithium Batteries." *Electrochem. Soc.Japan,* **84**, 797-801, (2016).

[76] N. Yabuuchi, K.Yoshii, S-T. Myung, I.Nakai and S. Komaba, "Detailed Studies of a High-Capacity Electrode Material for Rechargeable Batteries, Li_2MnO_3-$LiCo_{1/3}Ni_{1/3}Mn_{1/3}O_2$." *J. Am. Chem. Soc.,* **133**, 4404-4419, (2011).

[77] Z. Li, F. Du, X. Bie, D. Zhang, Y. Cai, X. Cui, C. Wang, G. Chen and Y. Wei, "Electrochemical Kinetics of the $Li[Li_{0.23}Co_{0.3}Mn_{0.47}]O_2$ Cathode Material Studied by GITT and EIS." *J. Phys. Chem. C*. **114**, 22751–22757, (2010).

[78] R. A. House, L.Jin, U. Maitra, K. Tsuruta, J. W. Somerville, D. P. Forstermann, F. Massel, L. Duda, M. R. Robertsa and P. G. Bruce, "Lithium manganese oxyfluoride as a new cathode material exhibiting oxygen redox." *Energy Environ. Sci.* **11**, 926-932, (2018).

[79] J. Lee, D.A. Kitchaev, D-H. Kwon1, C-W. Lee, J. K. Papp, Y-S. Liu, Z. Lun, R. J. Clément, T. Shi, B. D. McCloskey, J. Guo, M. Balasubramanian and G. Ceder, "Reversible Mn2+/Mn4+ double redox in lithium-excess cathode materials." *Nature*, **556**, (2018).

[80] F. Kong, C. Liang, R.C. Longo, D-H. Yeon, Y. Zheng, J-H. Park, S-G. Doo and K. Cho, "Conflicting Roles of Anion Doping on the Electrochemical Performance of Li-Ion Battery Cathode Materials." *Chem. Mater.* **28**, 6942-6952, (2016).

[81] X. Li, Z. Xie, W. Liu, W. Ge, H. Wang and M. Qu, "Effects of fluorine doping on structure, surface chemistry, and electrochemical performance of $LiNi_{0.8}Co_{0.15}Al_{0.05}O_2$." *Electrochim. Acta.* **174**, 1122-1130, (2015).

[82] N. Takeda, S. Hoshino, L. Xie, S. Chen, I. Ikeuchi, R. Natsui, K. Nakura and N. Yabuuchi, “Reversible Li storage for nanosize cation/anion-disordered rocksalt-type oxyfluorides: $LiMoO_2$ - x LiF ($0 \leq x \leq 2$) binary system.” *J. Power Sources.* **367**, 122-129, (2017).

[83] W. D. Richards, S. T. Dacek, D. A. Kitchaev, and G. Ceder, “Fluorination of Lithium-Excess Transition Metal Oxide Cathode Materials.” *Adv. Energy Mater.* **8,** 1701533, (2018).

[84] H. Ji, D. A. Kitchaev, Z. Lun, H. Kim, E. Foley, D-H. Kwon, Y. Tian, M. Balasubramanian, M. Bianchini, Z. Cai, R. J. Clement, J. C. Kim and G. Ceder, “Computational Investigation and Experimental Realization of Disordered High-Capacity Li-Ion Cathodes Based on Ni Redox.” *Chem. Mater.* **31**, 2431-2442, (2019).

[85] H. Z. Zhang, Q. Q. Qiao, G. R. Li, S. H. Ye and X. P. Gao, “Surface nitridation of Li-rich layered $Li(Li_{0.17}Ni_{0.25}Mn_{0.58})O_2$ oxide as cathode material for lithium-ion battery.” *J. Mater. Chem.* **22**, 13104-13109, (2012).

[86] J. O. Binder, S. P. Culver, R. Pinedo, D. A. Weber, M. S. Friedrich, K. I. Gries, K. Volz, W. G. Zeier and J. Janek, “Investigation of Fluorine and Nitrogen as Anionic Dopants in Nickel-Rich Cathode Materials for Lithium-Ion Batteries.”*ACS Appl. Mater. Interfaces,* **10**, 44452-44462, (2018).

[87] E. M. Erickson, H. Sclar, F. Schipper, J. Liu, R. Tian, C. Ghanty, L. Burstein, N.Leifer, J. Grinblat, M. Talianker, J-Y. Shin, J. K. Lampert, B. Markovsky, A. I. Frenkel, and D. Aurbach, High-Temperature Treatment of Li-Rich Cathode Materials with Ammonia: Improved Capacity and Mean Voltage Stability during Cycling, *Adv. Energy Mater.*, **7**, 1700708 (2017).

[88] N. Yabuuchi, M. Kajiyama, J. Iwatate, H. Nishikawa, S. Hitomi, R. Okuyama, R. Usui, Y. Yamada, and S. Komaba, “P2-type $Na_x[Fe_{1/2}Mn_{1/2}]O_2$ made from earth-abundant elements for rechargeable Na batteries.” *Nat. Mater*. **11**, 512-517, (2012).

[89] F. Sagane, T. Abe, Y. Iriyama, and Z. Ogumi, “Li^+ and Na^+ transfer through interfaces between inorganic solid electrolytes and polymer or liquid electrolytes.” *J. Power Sources.* **146**, 749-752, (2005).

[90] D. Aurbach, Z. Lu, A. Schechter, Y. Gofer, H. Gizbar, R. Turgeman, Y. Cohen, M. Moshkovich, and E. Levi, “Prototype systems for rechargeable magnesium batteries.” *Nature*, **407**, 724-727, (2000).

[91] M. Okoshi, Y. Yamada, A. Yamada, and H. Nakai, “Theoretical Analysis on De-Solvation of Lithium, Sodium, and Magnesium Cations to Organic Electrolyte Solvents.” *J. Electrochem. Soc.* **160**, A2160-A2165, (2013).

[92] M. Shiraga, F. Sagane, K. Miyazaki, T. Fukutsuka, T. Abe, K. Nishio, and Y. Uchimoto, *218th Electrochemical Society Meeting*, A1, No. 52 (2010).

Chapter 2. Structural analysis of imperfect Li_2TiO_3 and Li_2RuO_3 crystals

2-1. Introduction

In recent years, the so-called Li-rich layered compounds of the form Li_2MO_3 (*M*: pure transition metal or mixed transition metals) have been extensively investigated for use as superior cathode or anode materials for lithium-ion batteries because these materials theoretically have higher specific capacities than compounds of the form $LiMO_2$, exceeding at least 250 - 300 mAh/g, as can be expected from their Li-rich compositions. Among the various Li_2MO_3 compounds being explored, Li_2MnO_3 has been examined intensively [1-3] (see Figure 2-1). This ternary material crystallizes into a monoclinic crystal with *ABC* stacking of atomic layers, in which Li/Mn mixing at the transition-metal (TM) layers topologically forms long Li^+ percolation paths in the atomic configuration, which further contributes to the high capacity of this material [3].

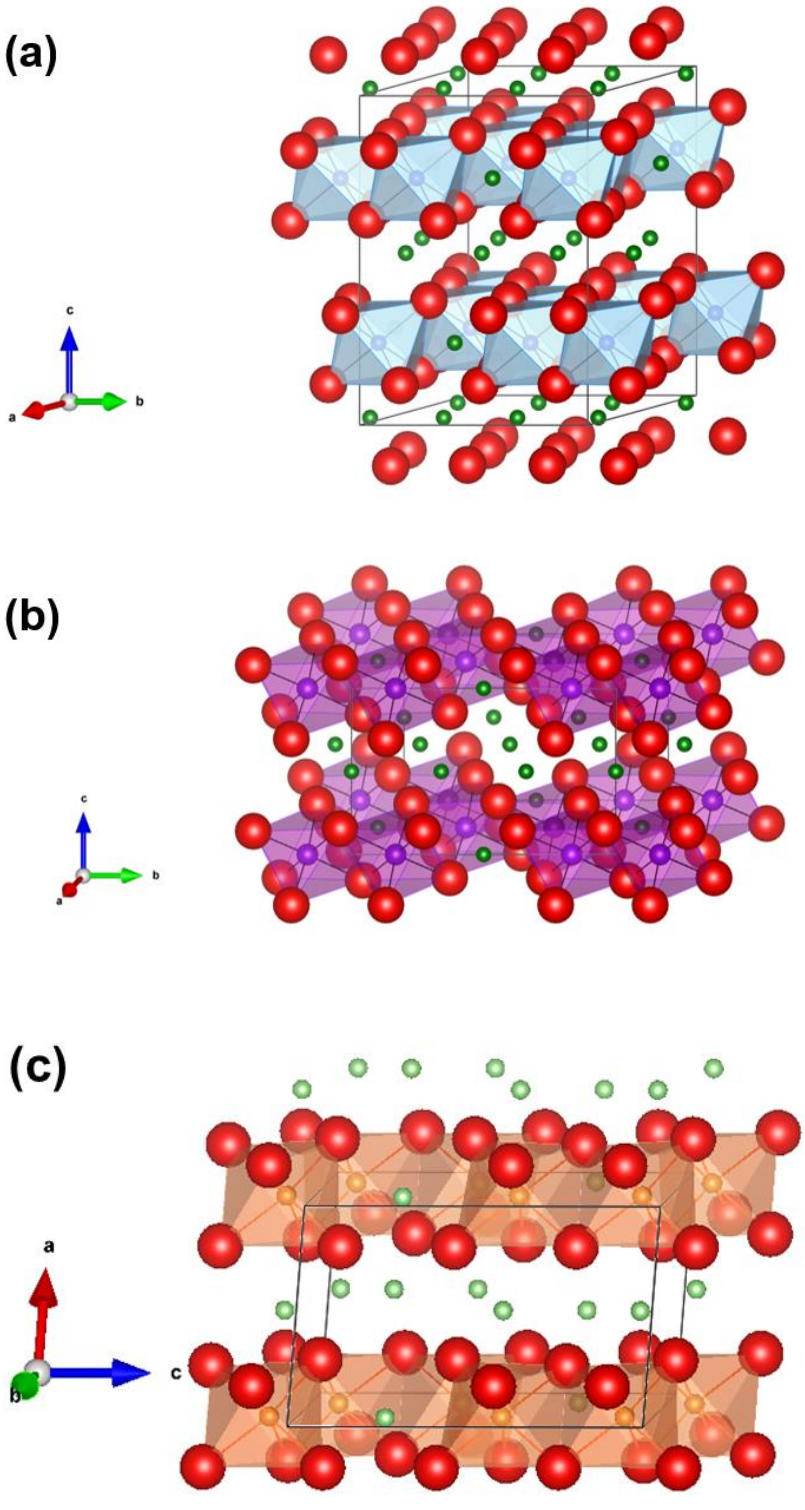

Figure 2-1. Stereographic views of the structure models for ideally ordered a) Li_2TiO_3 b) Li_2MnO_3 and c) Li_2RuO_3 (Li: green, O: red, Ti: blue, Mn: purple and Ru: orange). The crystal structure can be represented as a cubic close packing of oxygen atoms with

metal atoms placed in the octahedral voids. Li and Ti form two types of layers: one occupied only by Li atoms, and another occupied by 2/3 of Ti, Mn, Ru and 1/3 of Li.

Li_2TiO_3 is another Li_2MO_3 Li-rich layered compound [4]. As for lithium titanate compounds, not only Li_2TiO_3 but also $Li_4Ti_5O_{12}$ has been vigorously investigated for an anode material for lithium-ion batteries [5-9]. Li_2RuO_3 is also well known such Li_2MO_3 Li-rich layered compound containing 4d transition metal. Li_2RuO_3 has been reported for use as a cathode material for lithium-ion batteries with 250 - 300 mAh/g capacity.
The crystal structures of Li_2TiO_3, Li_2RuO_3 and Li_2MnO_3 are different from each other, as shown in Figure 2-1. Both structures consist of successive stacks of O, TM, and Li layers as $\cdots/\mathrm{O}/\mathrm{TM}/\mathrm{O}/\mathrm{Li}/\cdots$ (TM: Li/transition metal mixing layer). If a set of /O/TM/O/Li/ layers is regarded as a unit, both structures can be considered as successive stacks of these units (also see Figure 2-3). These units pile up regularly along the ***c***-axis direction in the Li_2MnO_3 crystal, while they are laminated in the Li_2TiO_3 crystal and shifted by $\left[-\frac{1}{6}, \frac{1}{6}\right]$ in the ***a***–***b*** plane (see Figure 2-1 (b)). In the Li_2RuO_3 crystal, these units pile up regularly along the ***a***-axis direction. Because of these differences in layer stacking, these crystals belong to different space groups, *C*2/*m*, *C*2/*c*, and $P2_1/m$, respectively. Kataoka et al. [10] have been analyzed the structure of Li_2TiO_3 in detail by the single-crystal method, and Tarakina et al. [11, 12] have been reported that this crystal has a serious number of stacking faults. However, we have found that Li_2MnO_3 comprises a great deal of structural defects, such as disordered atomic arrangements or stacking faults, depending on the synthesis conditions [3]. We then synthesized Li_2TiO_3 samples at 600–900 °C and Li_2RuO_3 sample at 900 °C and then performed powder diffraction measurements on them. In these diffraction patterns, we found not only weaker superstructure reflections than those expected from the ordered structure model but also diffused intensities attributed to stacking faults. To analyze such structural defects, the FAULTS program created by Cabanas *et al*. is very helpful [13], as it simultaneously allows for Rietveld refinement [14] and stacking fault analysis based on DIFFaX [15]. The kind of stacking fault observed in Li_2MnO_3 can occur in any other possible $Li_lM_mO_n$ (*l*, *m*, and *n*: integer) layered material in which the layers have ordered atomic arrangements. We carried out detailed structural analysis of our

Li_2TiO_3 and Li_2RuO_3 crystals using this FAULTS program. By the analysis of the stacking faults and atomic arrangements, we can obtain basic knowledge about the lithium diffusion mechanism due to the difference in crystal structure, which will be a very useful research for the future development of cathode materials for lithium ion batteries.

2-2. Experimental

2-2-1. Material Synthesis

Li_2TiO_3 powders were synthesized by a solid-state reaction using Li_2CO_3 and TiO_2 as precursors. The starting materials were thoroughly mixed by milling in acetone for 2 h. The resulting precursors were pelletized and calcined for 24 h in 1 atm of Ar gas. The calcination temperatures were 600, 650, 700, 750, 800, 850, and 900 °C, and the heating rate up to each resultant temperature and cooling rate down to 100 °C were both 300 °C/h. Li_2RuO_3 powders were also synthesized by a solid-state reaction using Li_2CO_3 and RuO_2 as precursors. The starting materials were thoroughly mixed by milling in acetone for 2 h. The resulting precursors were pelletized and calcined at 900 °C for 24 h in 1 atm of Air atmosphere. The heating rate and cooling rate down to 600 °C were both 300 °C/h and then quenched into liquid nitrogen. The powder specimens were produced by crushing heat-treated ingots and then packing them into flat glass sample holders with a depth of 0.2 mm for X-ray measurements in the Bragg–Brentano geometry.

2-2-2. X-ray Diffraction Measurements

Powder X-ray diffraction (XRD) patterns of Li_2TiO_3 were collected between 15° and 127° at a scan rate of 1°/min (in 2θ) on a Rigaku SmartLab diffractometer (*Cu Kα* radiation) equipped with a high-speed one-dimensional X-ray detector, D/teX Ultra [16]. In addition, for the specimen that was synthesized at 750 °C, we performed diffraction measurements using an incident beam monochromatized by a Johansson-type curved crystal to examine the structure in detail. XRD pattern of Li_2RuO_3 was collected between 2.1° and 78.216° on a semiconductor detector multiple diffractometer (λ = 0.61981 Å) equipped with a MYTHEN detector by synchrotron radiation XRD experiments at SPring-8 BL02B2.

Structure refinements were performed using the Rietveld method; the programs FAULTS and JANA2006 [17] were used for this purpose.

2-3. Results and discussion

The perfectly ordered structural model of Li_2TiO_3 has, as mentioned above, already been obtained. Based on this structural model, we carried out FAULTS structure refinement by taking the disordering of Li and Ti atoms at the TM layers and stacking faults into account. The analysis results are shown in Figure 2-2 and Table 2-1.

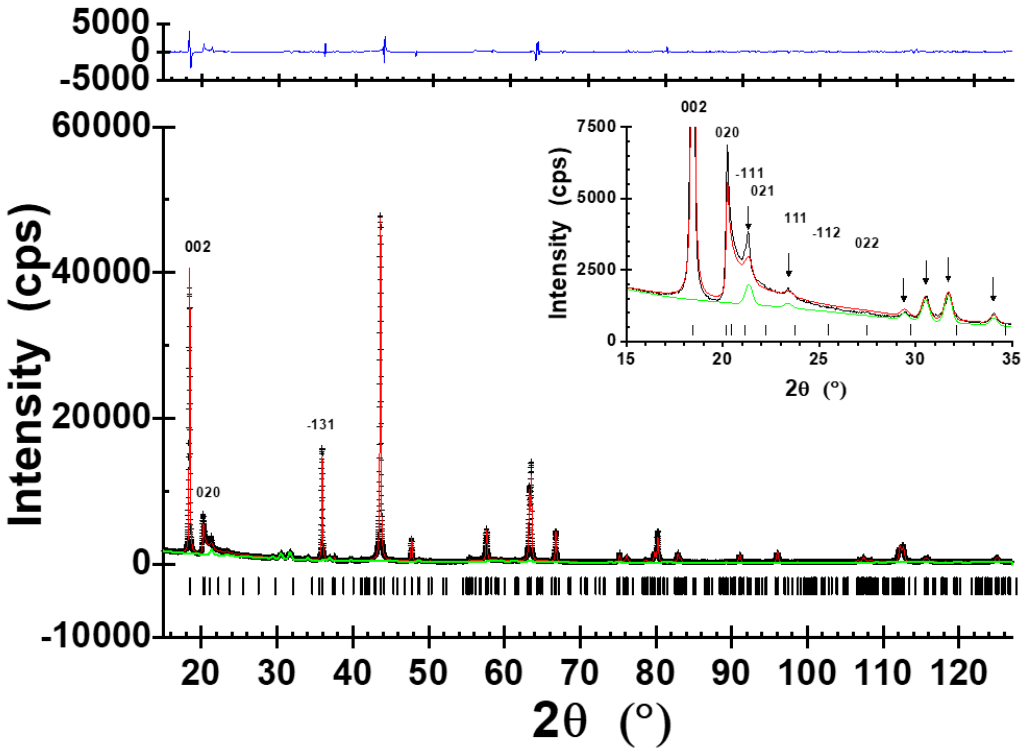

Figure. 2-2. Observed (+) and calculated (red line) X-ray powder diffraction profiles acquired at room temperature for Li_2TiO_3 synthesized at 750°C. Under the profiles, the background intensities and the reflection markers are indicated by the green line and by spikes. The difference curve (observed minus calculated) appears at the top of the figure in blue. Mirror indices are appended to some peaks: the 002 and -131 peaks are the fundamental reflections and the others are the superstructure reflections. Except for 020, the Bragg peaks of the latter reflections become extinct due to the generation of stacking

faults, due to varying diffuse scattering intensities. The arrows indicate to the peaks from residual Li_2CO_3.

Table 2-1: Refined structural parameters. The *g* parameters for Li/Ti (1) and Li/Ti (2) show the occupation rate of Li atoms relative to that of Ti atoms. The structural parameters and stacking probabilities, α_{11}, α_{12}, and α_{13}, were determined by a Rietveld program, FAULTS, under the assumption that $\alpha_{11} + \alpha_{12} + \alpha_{13} = 1$. This Rietveld analysis concluded that Li/Ti(3) – 4e site should contain no Li atoms.

*C*2/*c*: a = 5.0687(16) Å, b = 8.7765(14) Å, c = 9.7498(5) Å, β = 99.9793(31)°, B_{all} = 0.74(7) Å^2; R = 8.1%, χ^2 = 9.3.

atom	Site	*G*	*x*	*y*	*z*
Li (1)	8*f*	1	0.233(3)	0.905(3)	0.499(2)
Li (2)	4*d*	1	1/4	1/4	1/2
Li/Ti (1)	4*e*	0.234(1) / 0.766	0	0.085(1)	1/4
Li/Ti (2)	4*e*	0.766 / 0.234	0	0.417(3)	1/4
Li/Ti (3)	4*e*	1	0	0.747(1)	1/4
O (1)	8*f*	1	0.156(2)	0.244(2)	0.131(1)
O (2)	8*f*	1	0.120(2)	0.599(2)	0.136(1)
O (3)	8*f*	1	0.106(2)	0.909(2)	0.137(1)

α_{11}	α_{12}	α_{13}
0.747(1)	0.249(1)	0.004

The Li_2TiO_3 crystal consists of periodic *ABC* stacking of three different atomic layers, namely, the TM, O, and Li layers, along the *c*-axis direction, as follows (see Figure 2-1 and Figure 2-3):

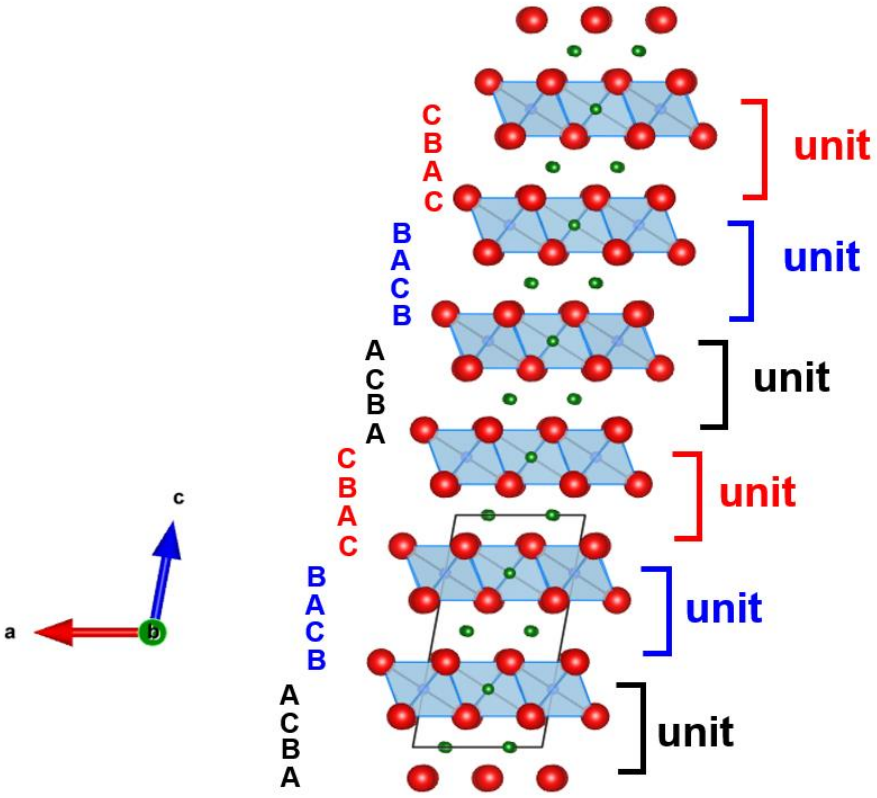

Figure 2-3. Structure model for the ideally ordered Li_2TiO_3 represented in a trigonal lattice (Li: green, O: red, and Ti: blue), in which atoms are arranged in layer stacking structure; the Li_2TiO_3 monoclinic structure can be assumed to have a trigonal atomic arrangement. The monoclinic cell is depicted with thin solid lines. This structure can also be regarded as *ABC* stacking of structural units consisting of four atomic layers of O, TM, O, and Li. FAULTS analysis was performed with this trigonal structure model.

This structure can also be described as a pseudo-trigonal cell consisting of 24 atomic layers, as shown in Figure 2-3. We carried out FAULTS analysis for Li_2TiO_3 with this pseudo-trigonal cell in the *P*1 space group. It can be seen to consist of *ABC* stacking of the above-mentioned structural units formed by -O-TM-O-Li- atomic layers. In a perfect crystal (without stacking faults), every unit is obtained by a shift of $\left[-\frac{1}{3}, 0, \frac{1}{6}\right]$ in the trigonal axis from each unit directly below. When layers are laminated

in order, stacking faults are generated in such layered structures if the glide translation of the next unit is anything other than $\left[-\frac{1}{3}, 0, \frac{1}{6}\right]$ (Figure 2-4).

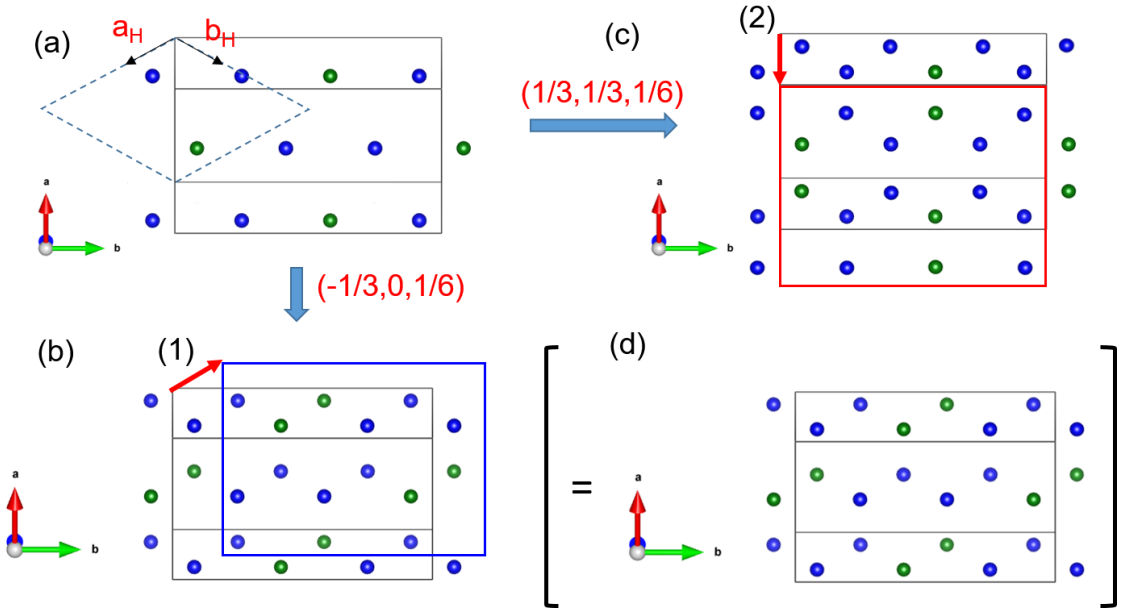

Figure 2-4. One of the TM layers extracted from the *C*2/*c* monoclinic unit cell is shown in the panel (a) at the top of the figure. Two kinds of Li/Ti atomic configurations at the TM layers in the upper and lower consecutive structural units are shown in panels, (b), (c), and (d). The atomic arrangement in panel (a) corresponds to the lower TM layer of the two. When the lower structural unit is stacked onto the original unit and shifted by (1): [-1/3, 0, 1/6] (in the hexagonal axis notation, dotted line in the panel (a)), they form an identical topological pattern to that seen in panel (d). This is the case of regular stacking without stacking fault. Whereas, when the former unit is laminated on the latter and shifted by (2): [1/3, 1/3, 1/6], this makes a different topological pattern as shown in panel *c*. This difference in atomic arrangement is caused due to the atomic ordering of the TM layer. When these atoms are in a completely disordered atomic arrangement, these two kinds of stackings make no difference in the geometric pattern. This applies to the cases of the Li and O layers in the lower and upper units. Namely, these Li-Li layers and O-O layers make no difference in topological pattern both in the [-1/3, 0, 1/6] and [1/3, 1/3, 1/6] shifts.

Here, it is assumed that stacking faults were never generated at interlayers within the units in Expression (1) (and in Figure 2-3). We can fully describe the regular stacking and other possible stacking faults using three different stacking vectors, $\left[-\frac{1}{3}, 0, \frac{1}{6}\right]$, $\left[\frac{1}{3}, \frac{1}{3}, \frac{1}{6}\right]$ (both as cubic-type stacking), and $\left[0, \frac{1}{3}, \frac{1}{6}\right]$ (as a hexagonal-type stacking) in the pseudo-trigonal cell, and using linear combinations (multiplications) of these vectors. For instance, combination of the former two cubic-type stacking vectors can locally form the $P3_112$ trigonal and *C2*/*m* monoclinic atomic configurations as shown in Tarakina et al.'s paper [11,12]. They have analyzed the stacking faults in the *C2*/*c* Li_2TiO_3 crystal assuming that its layer stacking contains the $P3_112$ trigonal and *C2*/*m* monoclinic atomic configurations. The above these three stacking vectors correspond to$\left[-\frac{1}{6}, \frac{1}{6}, \frac{1}{2}\right]$, $\left[\frac{1}{3}, 0, \frac{1}{2}\right]$, and $\left[\frac{1}{6}, \frac{1}{6}, \frac{1}{2}\right]$ in the monoclinic (*C*2/*c*) cell. The translation probabilities for these stacking vectors are represented by the three α parameters, α_{11}, α_{12}, and α_{13}, which are determined through FAULTS analysis. When $\alpha_{11} = 1$, $\alpha_{12} = 0$, and $\alpha_{13} = 0$, the crystal contains no stacking faults; however, if the TM layer has a completely disordered (random) atomic arrangement, there is no difference between α_{11} and α_{12} (see Figure 2-4). After analyses in FAULTS program, we converted the data from *P*1 trigonal structures back to *C*2/*c* monoclinic structures. As seen in Table 1 and Figure 2-5, our FAULTS analysis revealed that Li_2TiO_3 crystals contain about 25% stacking faults. Such large numbers of stacking faults have also been detected in Li_2MnO_3, which exhibits the same type of structure. However, both Li_2TiO_3 and Li_2MnO_3 have almost no hexagonal-type stacking faults. If hexagonal-type stacking faults were generated in these crystals, the distance between O^{2-} ions of two consecutive top and bottom oxygen layers would be around 2.3 Å, which is considered too short for these large ions ($r \approx 1.4$ Å) [18]. As seen in Figure 2-5, the three stacking fault probabilities are almost unchanged, irrespective of synthesis temperature.

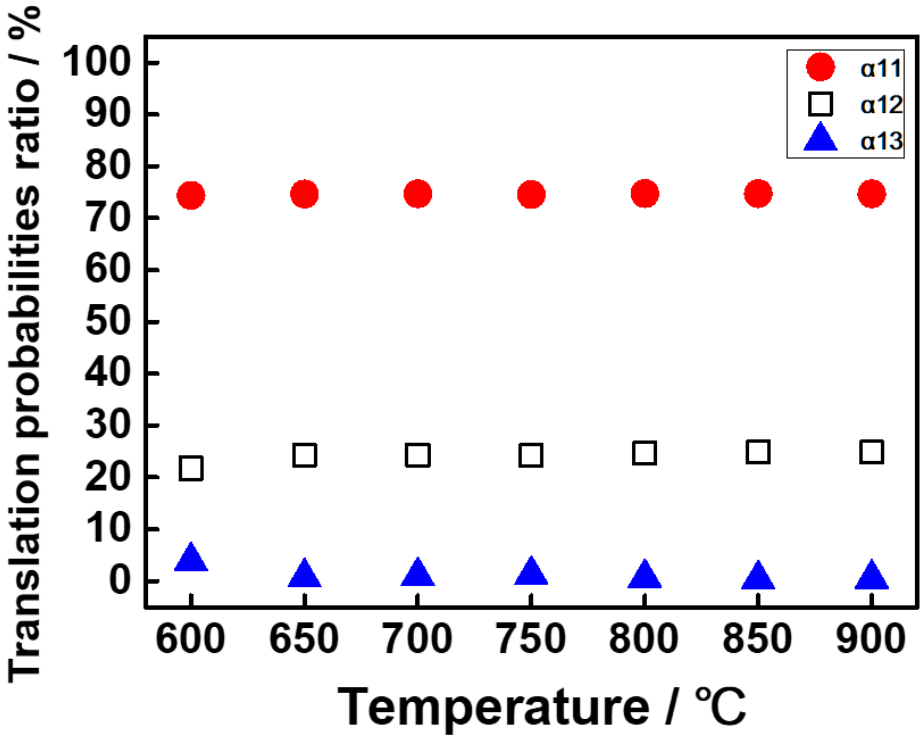

Figure 2-5. Translation probabilities, α_{11}, α_{12}, and α_{13}, determined by Rietveld analysis as a function of synthesis temperature.

Usually, we roughly understand crystal structures from analyses that are performed without taking stacking faults into account. We performed this type of simple analysis using the JANA2006 program to examine the powder diffraction pattern of Li_2TiO_3 synthesized at 750 °C. The results are shown in Table 2-2. As seen in Table 2-2, this analysis concluded that all three transition metal sites should be occupied in random configurations by both Li and Ti atoms. However, as shown in Table 2-1, the FAULTS analysis showed that one of the three sites of the TM layer is exclusively occupied by Ti atoms, and the others are also occupied by their respective favorite atoms. Both stacking faults and atomic disordering affect the diffraction intensities; therefore, when the crystals contain both structural defects, their structures should be analyzed while taking both structural imperfections into account. Figure 2-6 shows the Li/Ti atomic mixing for the compounds synthesized from 600 °C to 900 °C. As seen in Figure 2-6, the atomic disordering gradually became larger as the synthesis temperature was increased. It is well known that when the temperature is raised, the atomic arrangement generally

becomes more irregular to decrease the free energy of the system. This irregularity in atomic configuration with increasing temperature is considered to be a reasonable physical phenomenon for general materials [19-21].

Table 2-2: Structural parameters for Li_2TiO_3 obtained by the Rietveld refinement performed under the assumption that this crystal contains no stacking faults. Standard deviations are shown in parentheses.

*C*2/*c*: a = 5.0668(7) Å, b = 8.784(1) Å, c = 9.752(2) Å, β = 100.03(1)°, B_{all} = 0.89(18) Å^2; R_{wp} = 6.59%, R_p = 4.54%, R_{Fwobs} = 6.81%, and R_{Fobs} = 5.69%.

Atom	Site	*G*	*x*	*y*	*z*
Li (1)	8*f*	1	0.224(9)	0.085(9)	-0.005(9)
Li (2)	4*d*	1	1/4	1/4	1/2
Li/Ti (1)	4*e*	0.477(32) / 0.523	0	0.092(4)	1/4
Li/Ti (2)	4*e*	0.385(30) / 0.615	0	0.419(4)	1/4
Li/Ti (2)	4*e*	0.138 / 0.862	0	0.746(3)	1/4
O (1)	8*f*	1	0.138(5)	0.254(6)	0.138(2)
O (2)	8*f*	1	0.145(6)	0.581(6)	0.134(3)
O (3)	8*f*	1	0.111(6)	0.912(5)	0.134(3)

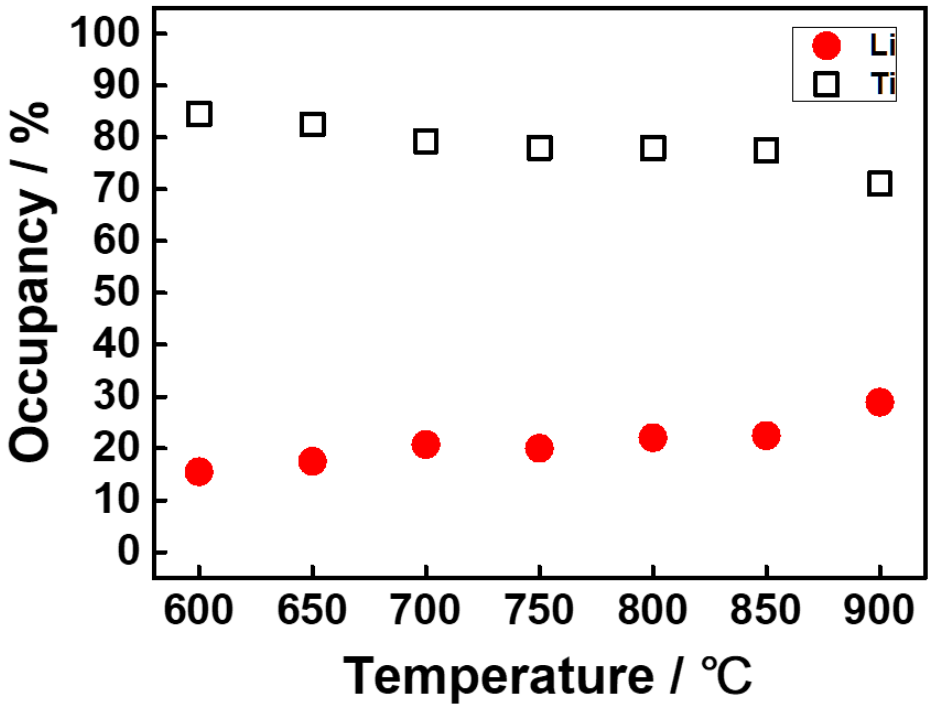

Figure 2-6. Occupancies of Li and Ti atoms at the Li/Ti(1) site (see Table 1 and Supporting Information), also showing the mixing rates of both atoms between the Li/Ti(1) and Li/Ti(2) sites.

The details of the ordered/disordered atomic arrangements for this Li_2TiO_3 material are a future subject to be investigated. Figure 2-7 shows the mean crystallite size determined by Rietveld analysis as a function of the synthesis temperature. As seen in Figure 2-7, the crystallites of Li_2TiO_3 suddenly began to grow around above 700 °C, whereas the melting point of Li_2TiO_3 is 1325 °C [22]. This suggests that the recrystallization temperature of this material lies around 700 °C, corresponding to about 60% of the melting point. This abrupt growth in crystallite size around at 700 °C also indicates possibility of the size-induced phase transition in the Li_2TiO_3 crystal [23]; however, detailed investigation on this interesting topic is left the future subject to be performed.

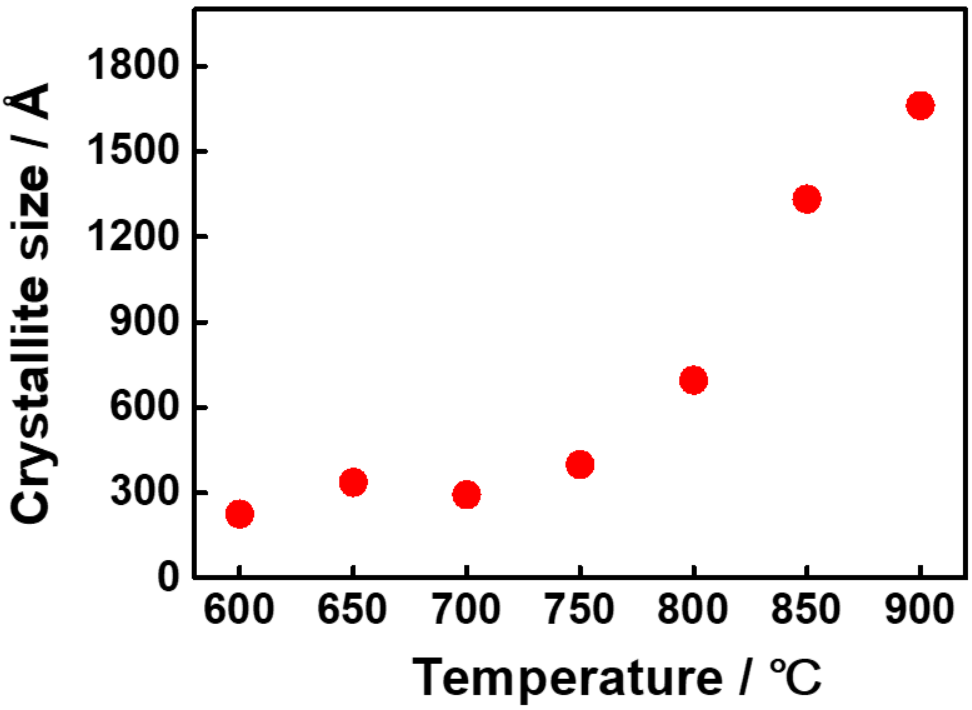

Figure 2-7. Dependence of the crystallite size on the synthesis temperature estimated by FAULTS analysis.

The perfectly ordered structural model of Li_2RuO_3 has already been obtained as mentioned in Figure 2-8. Based on this structural model, we carried out FAULTS structure refinement by taking the disordering of Li and Ru atoms at the TM layers and stacking faults into account as shown in this section. The analysis result of Li_2RuO_3 crystal is shown in Figure 2-9.

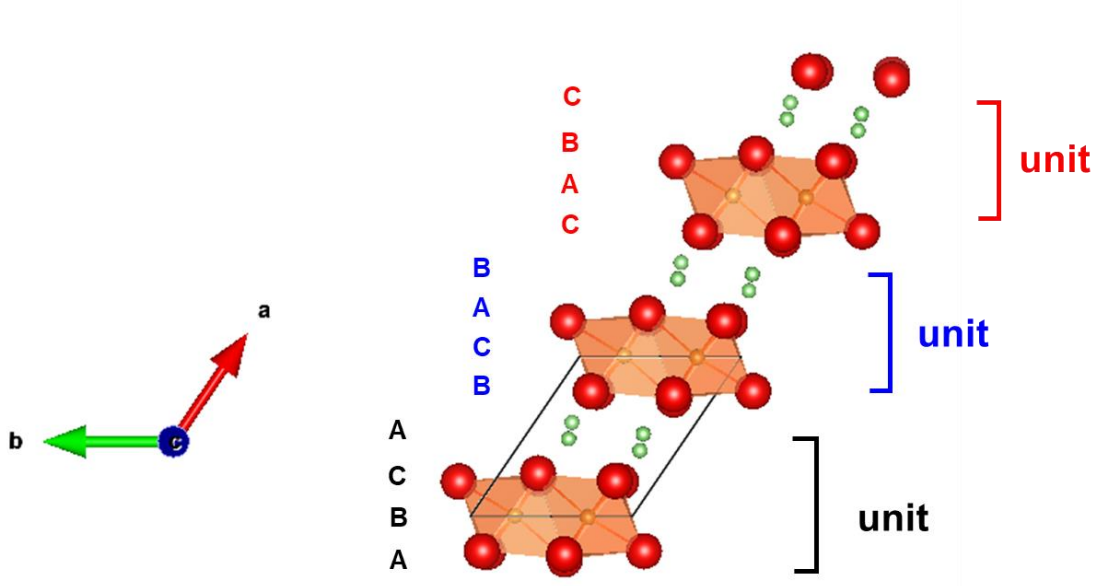

Figure 2-8. Structure model for the ideally ordered Li_2RuO_3 (Li: green, O: red, and Ru: orange), in which atoms are arranged in layer stacking structure. The monoclinic cell is depicted with thin solid lines. This structure can also be regarded as *ABC* stacking of structural units consisting of four atomic layers of O, TM, O, and Li.

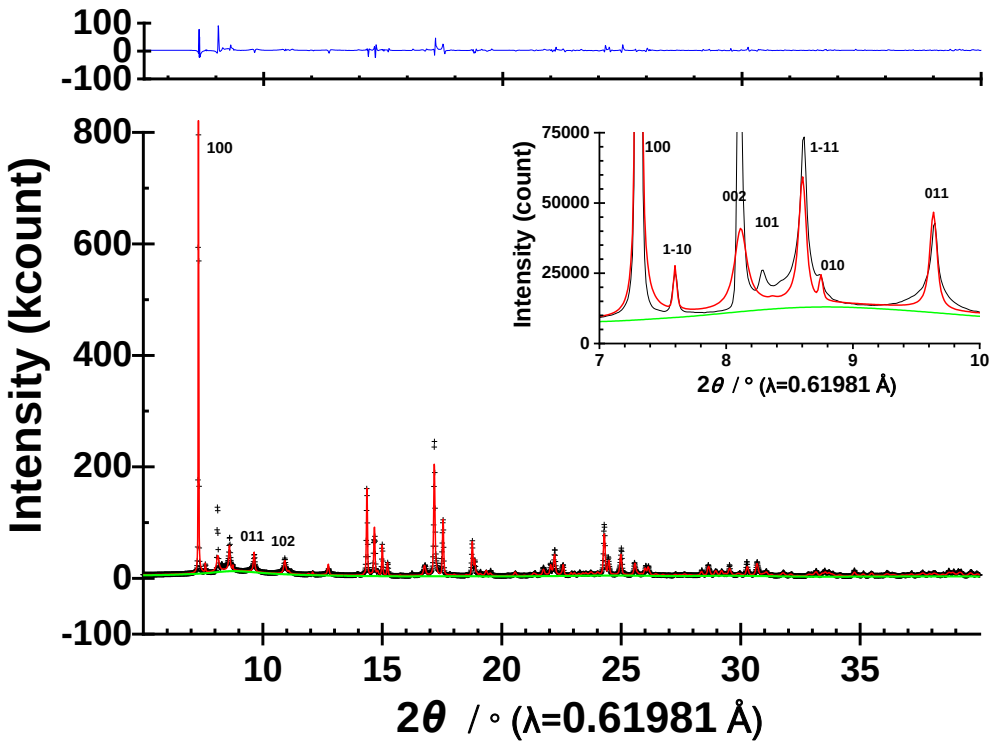

Figure. 2-9. Observed (+) and calculated (red line) X-ray powder diffraction profiles acquired at room temperature for Li_2RuO_3 synthesized at 900℃. Under the profiles, the background intensities are indicated by the green line. The difference curve (observed minus calculated) appears at the top of the figure in blue.

The results of Li_2RuO_3 Rietveld analysis suggested the formation of staking faults and atomic arrangements between Li and Ru in TM layers. The stacking faults of Li_2RuO_3 were described as three vectors to $[1,0,0]$, $\left[1,0,-\frac{1}{3}\right]$, and $\left[1,-\frac{1}{2},-\frac{1}{6}\right]$ in the monoclinic ($P2_1/m$) cell as shown in Figure 2-10. Since Li_2RuO_3 has a different crystal structure from Li_2TiO_3, the arrangement of atoms is such that stacking faults in all directions satisfy cubic close packing. The translation probabilities for these stacking vectors are represented by the three α parameters, α_{11}, α_{12}, and α_{13}, which are determined through FAULTS analysis. When $\alpha_{11} = 1$, $\alpha_{12} = 0$, and $\alpha_{13} = 0$, the crystal contains no stacking faults.

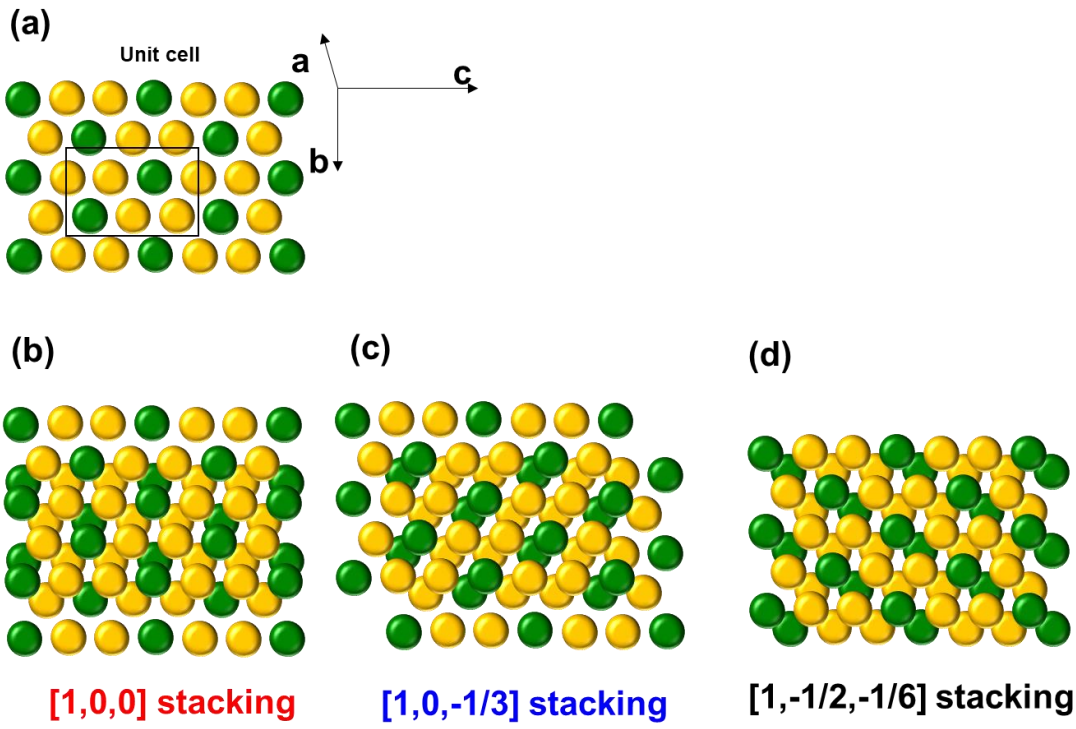

Figure 2-10. One of the TM layers extracted from the *P2₁/m* monoclinic unit cell is shown in the panel (a) at the top of the figure. Three kinds of Li/Ru atomic configurations at the TM layers in the upper and lower consecutive structural units are shown in panels, (b), (c), and (d). The atomic arrangement in panel (a) corresponds to the lower TM layer of the two. When the lower structural unit is stacked onto the original unit and shifted as shown in panel (b): [1, 0, 0], this is the case of regular stacking without stacking fault. Whereas, when the former unit is laminated on the latter and shifted as shown in panel (c): [1, 0, -1/3] and panel (d) [1, -1/2, -1/6], these make different topological patterns. These differences in atomic arrangement are caused due to the atomic ordering of the TM layer. When these atoms are in a completely disordered atomic arrangement, these two kinds of stackings make no difference in the geometric pattern. This applies to the cases of the Li and O layers in the lower and upper units. Namely, these Li-Li layers and O-O layers make no difference in topological pattern all shifts.

As seen in Table 2-3, our FAULTS analysis revealed that Li_2RuO_3 crystal contain about only 5% stacking faults. This result is a very small value compared to Li_2TiO_3 calcined at 900 °C. In addition, Li_2RuO_3 crystal only about 12% of the atomic

disordering, which is also smaller ratio than Li_2TiO_3. Li/TM mixing at the TM layers caused by stacking faults and topologically forms long three-dimensional Li^+ percolation paths in the atomic configuration, which further contributes to the high capacity of this material [3]. Therefore, it is considered that the Li^+ diffusion mechanism of Li_2RuO_3 is hardly affected by three-dimensional diffusion, which is different from the results of Li_2TiO_3 and Li_2MnO_3 (especially synthesized at low temperature [3]).

Table 2-3. The results were determined by a Rietveld program, FAULTS, under the assumption that $\alpha_{11} + \alpha_{12} + \alpha_{13} = 1$. For comparison, the generation ratio of stacking faults and atomic disordering of Li_2TiO_3 and Li_2MnO_3 calcined at 900 °C is also described. The stacking faults formation ratio of Li_2RuO_3 is represented by $\alpha_{12} + \alpha_{13}$ (ratio of Li_2TiO_3 and Li_2MnO_3 is α_{12}).

	Li_2RuO_3	Li_2TiO_3	Li_2MnO_3
Stacking faults	5 %	25 %	10 %
Atomic disordering	12 %	25 %	9 %

2-4. Conclusions

Li_2TiO_3 and Li_2RuO_3 compounds were crystallized into single-phase monoclinic structures. It is known that these crystals belong to the monoclinic space group $C2/c$ and $P2_1/m$, respectively, and that contain significant numbers of stacking faults. Our structural analysis results confirmed that Li_2TiO_3 crystal crystalizes in the C2/c structure, however, found that it contains not only a large number of stacking faults but partial Li/Ti atomic mixing is present at the TM layers. The number of stacking faults was almost unchanged irrespective of the synthesis temperature, whereas atomic disordering at the TM layer was found to grow considerably larger with increasing synthesis temperature. On the other hand, the analysis results show that Li_2RuO_3 is less likely to cause stacking faults and atomic disordering. These observations suggest that these crystal defects are inherent structural features of Li-rich Li_2MO_3 crystals, and their possibility of defects formation depends on the type of transition metal contained in the material. The results of this work clarify the difference of Li^+ diffusion mechanism in Li-rich materials and provide useful guidelines for future cathode material design.

2-5. References

[1] D. Y. W. Yu, K. Yanagida, Y. Kato and H. Nakamura, "Electrochemical Activities in Li_2MnO_3." *J. Electrochem. Soc.* **156**, A417-424, (2009).

[2] A. Boulineau, L. Croguennec, C. Delmas and F. Weill, "Structure of Li_2MnO_3 with different degrees of defects." *Solid State Ionics*. **180**, 1652-1659, (2010).

[3] T. Matsunaga, H. Komatsu, K. Shimoda, T. Minato, M. Yonemura, T. Kamiyama, S. Kobayashi, T. Kato, T. Hirayama, Y. Ikuhara, H. Arai, Y. Ukyo, Y. Uchimoto and Z. Ogumi, "Dependence of Structural Defects in Li_2MnO_3 on Synthesis Temperature." *Chem. Mater*. **28**, 4143-4150, (2016).

[4] M. Vijayakumar, S. Kerisit, Z. Yang, G. L. Graff, J. Liu, J. A. Sears, S. D. Burton, K. M. Rosso and J. Hu, "Effect of Chemical Lithium Insertion into Rutile TiO_2 Nanorods." *J. Phys. Chem. C.* **113**, 14567-14574, (2009).

[5] I. A. Leonidov, O. N. Leonidova, L. A. Perelyaeva, R. F. Samigullina, S. A. Kovyazina and M. V. Patrakeev, "Structure, ionic conduction, and phase transformations in lithium titanate $Li_4Ti_5O_{12}$." *Physics of the Solid State*. **45**, 2183-2188, (2003).

[6] X. Sun, M. Hegde, Y. Zhang, M. He, L. Gu, Y. Wang, J. Shu, P. V. Radovanovic and B. Cui, "Structure and Electrochemical Properties of Spinel $Li_4Ti_5O_{12}$ Nanocomposites as Anode for Lithium-Ion Battery." *Int. J. Electrochem. Sci*. **9**, 1583-1596, (2014).

[7] S. Li, J. Guo, Y. Yang, X. Dong, M. Yang, W. Yu, J. Wang and G. Liu, "Electrospun $Li_4Ti_5O_{12}/Li_2TiO_3$ composite nanofibers for enhanced high-rate lithium ion batteries." *J. Solid State Electrochem.* **21**, 2779-2790, (2017).

[8] A. L-Narayana, M. Dhananjaya, N. G-Prakash, O M. Hussain, A. Mauger and C. M. Julien, "Li_2TiO_3 /Graphene and Li_2TiO_3 /CNT Composites as Anodes for High Power Li-Ion Batteries." *ChemistrySelect*. **3**, 9150-9158, (2018).

[9] Y. Wang, A.Zhou, X. Dai. L. Feng, J. Li and J. Li, "Solid-state synthesis of submicron-sized $Li_4Ti_5O_{12}/Li_2TiO_3$ composites with rich grain boundaries for lithium ion batteries." *J. Power Sources*. **266**, 114-120, (2014).

[10] K. Kataoka, Y. Takahashi, N Kijima, H. Nagai, J. Akimoto, Y. Idemoto and K. Ohshima, "Crystal growth and structure refinement of monoclinic Li_2TiO_3." *Mater. Res. Bull.* **44**, 168-172, (2009).

[11] N. V. Tarakina, R. B. Neder, T. A. Denisova, L. G. Maksimova, Y. V. Baklanova, A. P. Tyutyunnika and V. G. Zubkova, "Defect crystal structure of new $TiO(OH)_2$ hydroxide and related lithium salt Li_2TiO_3." *Dalton Trans.* **39**, 8168-8176, (2010).

[12] N. V. Tarakina, T. A. Denisova, Y. V. Baklanova, L. G. Maksimova, V. G. Zubkov and R. B. Neder, "Defect Crystal Structure of Low Temperature Modifications of Li_2MO_3 (M=Ti, Sn) and Related Hydroxides." *Advances in Science and Technology*. **63**, 352-357, (2010).

[13] M. Casas-Cabanas, J. Rodríguez-Carvajal and M. R. Palacín, "FAULTS, A New Program for Refinement of Powder Diffraction Patterns from Layered Structures." *Z. Kristallogr. Suppl.* 144-145, (2006).

[14] H. M. Rietveld, "A profile refinement method for nuclear and magnetic structures." *J. Appl. Cryst.* **2**, 65-71, (1969).

[15] M. M. Treacy, J. M. Newsam and M. W. Deem, "A General Recursion Method for Calculating Diffracted Intensities from Crystals Containing Planar Faults." *Proc. R. Soc. Lond. A*, **433**, 499-520, (1991).

[16] http://www.rigaku.com/products/xrd, http://www.rigaku.com/node/4442

[17] V. Petříček M. Dušek, L. Palatinus, "Crystallographic Computing System JANA2006: General features." *Z. Kristallogr.*, **229**, 345-352, (2014).

[18] R. D. Shannon, "Revised effective ionic radii and systematic studies of interatomic distances in halides and chalcogenides." *Acta Crystallogr*. **A32**, 751-767, (1976).

[19] T. Matsunaga, Y. Umetani, N. Yamada, "Structural study of a $Ag_{3.4}In_{3.7}Sb_{76.4}Te_{16.5}$ quadruple compound utilized for phase-change optical disks." *Phys. Rev. B.* **64**, 184116, (2001).

[20] B. E. Warren, "X-ray diffraction." Addison-Wesley, Reading, Mass, (1969).

[21] L. D. Landau, A. I. Akhizer, and E. M. Lifshitz, "GENERAL PHYSICS – Mechanics and Molecular Physics –" *Pergamon Press.* (1967).

[22] Haynes, William M., ed. "CRC Handbook of Chemistry and Physics (92nd ed.)" *CRC Press*, (2011).

[23] A. Laumann, H. Boysen, M. Bremholm, K. T. Fehr, M. Hoelzel and M. Holzapfel, “Lithium Migration at High Temperatures in $Li_4Ti_5O_{12}$ Studied by Neutron Diffraction.” *Chem. Mater.*, **23**, 2753-2759, (2011).

Chapter 3. Reaction Mechanism of Electrochemical Insertion/Extraction of Magnesium Ions in Olivine-type $FePO_4$

3-1. Introduction

Magnesium rechargeable batteries are promising candidates for next-generation battery systems because the low-cost magnesium metal anode provides a high energy density and high stability [1] without any formation of dendritic structures such as those due to lithium deposition [2,3]. Although magnesium rechargeable batteries have a high potential, their performance reported so far [4] has not been comparable to that of lithium ion batteries. One serious problem is the limited number of alternative cathode materials. Compared to lithium ions, magnesium ions seem to have more difficult insertion/extraction reactions because of their stronger ionic interactions and because redistribution of the charge of the inserted multivalent cation in the cathode is more difficult [5]. Previously proposed cathode materials such as Chevrel phases [5-7], V_2O_5 [8-9], TiS_2 [10], MoS_2 [11], and MnO_2 [12] suffer from low redox potentials, low capacity, hydrous phases, or low stability. If the conventional intercalation hosts used in lithium ion batteries could be used, the performance of magnesium rechargeable battery would be drastically improved. Recently, several spinel type transition metal oxides, MgM_2O_4, (M = Co, Mn), show reversible intercalation/de-intercalation of Mg^{2+} into/from spinel host have reported experimentally [13-15]. Polyanion type cathode materials using phosphoric acid is an attractive material group as a battery material having stable structure and the high reaction potential due to the inductive effect [16]. We have reported magnesium battery cathodes using polyanion compounds which are used in lithium ion battery [17,18]. However, there is a lack of information on the reaction mechanism for the insertion/extraction of lithium ions versus magnesium ions into the same host structure.

To investigate the magnesium/lithium ion insertion mechanism, olivine-type $FePO_4$ is chosen here as a host structure. For the lithium ion insertion/extraction

reaction, a two-phase reaction between Li-rich $Li_{1-\alpha}FePO_4$ and Li-poor $Li_\beta FePO_4$ has been reported [19]. In the regions outside both endpoints of the miscibility gap, a single-phase reaction occurs [16]. The single-phase regions decrease with decreasing particle size [20, 21] or with multiple transition metal substitution [22]. Recently, the insertion/extraction reaction of sodium ions in $FePO_4$ has also been studied [23-26]. In the sodium system, $FePO_4$ shows one plateau during the sodium ion insertion process but two potential plateaus during the extraction process, which indicates the formation of the intermediate $Na_{0.7}FePO_4$ phase [23-26]. The insertion/extraction reaction mechanism in the sodium system is different from that in the lithium system because of the difference in cation sizes. For the magnesium system, Several studies reported that electrochemical magnesium ion insertion/extraction in $FePO_4$ [27,28] and that a redox potential for $Mg_{0.5}FePO_4/FePO_4$ of approximately 2.4 V (vs. Mg^{2+}/Mg) and that the volume expansion is similar to that of the $LiFePO_4/FePO_4$ system [29]. However, there are no experimental reports on the phase change behavior of $FePO_4$ during magnesium ion insertion/extraction.

This study investigated the reaction mechanism of magnesium ion insertion/extraction in $FePO_4$ prepared from carbon-coated $LiFePO_4$ by chemical delithiation. The electrochemical magnesium ion insertion/extraction reaction is demonstrated, and the valance change and crystal structure change are analyzed by X-ray absorption spectroscopy (XAS) and X-ray diffraction (XRD). This is the first report of the completely different phase transition behaviours of $FePO_4$ for magnesium ion insertion/extraction and for lithium ion insertion/extraction.

3-2. Experimental

Carbon-coated $LiFePO_4$ (C-$LiFePO_4$) was prepared by solid-state reaction. Li_2CO_3, $FeC_2O_4 \cdot 2H_2O$, and $(NH_4)_2HPO_4$ were mixed at stoichiometric ratios in ethanol using a planetary ball mill with a zirconia pot and balls for 12 h at 400 rpm. After milling and drying, the precursor was mixed with 10 wt% carbon black in the ball mill for 24 h at a rotation speed of 400 rpm. The mixture was pelletized and annealed at 600°C under a 97% argon-3% hydrogen atmosphere for 6 h. C-$FePO_4$ was prepared by chemical oxidation of the obtained C-$LiFePO_4$ using nitronium tetrafluoroborate

(NO_2BF_4) as an oxidizing agent. NO_2BF_4 was dissolved in acetonitrile, and then the C-$LiFePO_4$ powder was stirred in the solution for 48 h. The mixture was filtered and washed with acetonitrile. The particle size of the obtained C-$FePO_4$ was examined by scanning electron microscopy (SEM) at 5.0 kV (Hitachi-SU6600).

Electrochemical measurements were carried out using a three-electrode cell with an Ag^+/Ag double junction reference electrode. The working electrode was made by mixing 80 wt% the obtained C-$FePO_4$, 15 wt% acetylene black, and 5 wt% polytetrafluoroethylene and the resulting mixture was pressed by platinum meshes. The counter electrode was a magnesium rod, and the electrolyte was 0.5 M magnesium bis(trifluoromethanesulfonyl)imide in acetonitrile. A platinum substrate was employed as a current collector because of its stability in the magnesium electrolyte [30]. Galvanostatic discharge and charge measurements were performed with a C/30 rate in the potential range of –0.80 V to 1.0 V vs. Ag^+/Ag at 55°C. The equilibrium potential of the cells was obtained by performing a quasi–open-circuit-voltage (quasi-OCV) measurement, in which a series of current pulses is applied at C/30 for 3 h, followed a 20 h relaxation process. The quasi- OCV curve in the charge process was measured for a sample in which 0.4 Mg^{2+} ions per formula unit were inserted in constant current mode.

The XRD patterns were measured at room temperature at beam line BL02B2, which is equipped with a Debye-Scherrer camera, at SPring-8 in Hyogo, Japan. To minimize the effect of X-ray absorption by the samples, the wavelength of the incident X-ray beam was set to *ca.* 0.500 Å using a silicon monochromator, which was calibrated with a CeO_2 standard in the range $2\theta = 0° - 75°$ with a 2θ step size of 0.01°. Rietveld and Le Bail profile fittings were carried out with the program JANA2006 (Windows version, copyright 2008) [31] using a pseudo-Voigt profile function. For synchrotron XRD measurements, the discharged/charged electrodes were rinsed several times with acetonitrile and dried. A glass capillary was filled with the dried sample and then sealed by a resin in an argon-filled glove box.

XAS measurements of the discharged/charged electrodes was conducted in the energy region of the Fe *K*-edge at room temperature in transmission mode at beam lines BL01B1 and BL14B2 of the SPring-8 synchrotron radiation facility in Hyogo, Japan. After the electrochemical measurements, the samples were rinsed several times with

acetonitrile and dried. The dried sample was mixed with boron nitride and pelletized, then sealed in laminated packets in an argon-filled glove box.

3-3. Results and discussion

3-3-1. Sample preparation and characterization

Figure 3-1 shows the powder XRD patterns of the obtained C-$FePO_4$. The XRD pattern was indexed to the orthorhombic *Pnma* space group with lattice constants a = 9.8182(2) Å, b = 5.7931(1) Å, c = 4.7825(1) Å, and V = 272.02(1) $Å^3$, which were coincident with the values in the literature [32]. There are no detectable peaks attributed to impurities in the sample. In order to investigate the particle size of the C-$FePO_4$, a SEM image of the sample was captured (Figure 3-2). The average particle size of the as-prepared C-$FePO_4$ was about 65 nm.

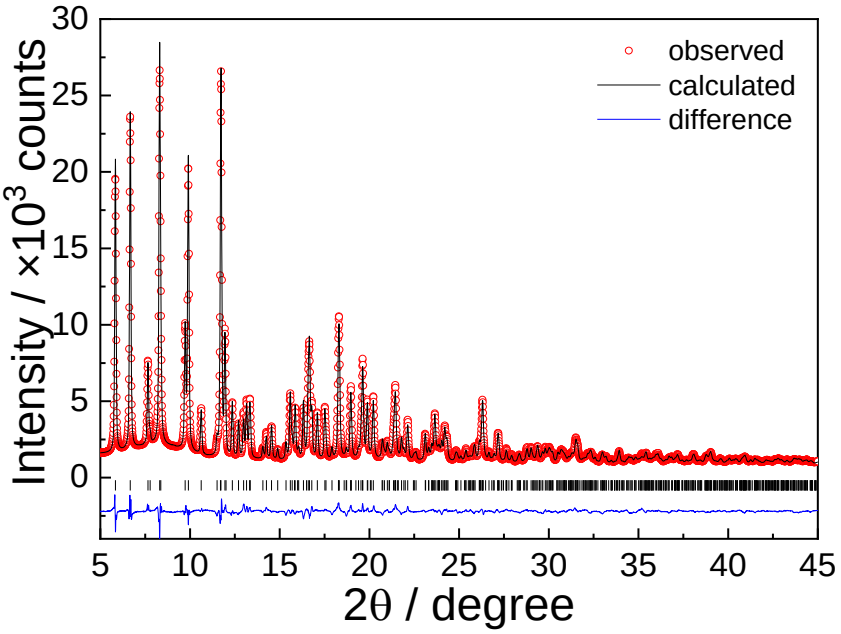

Figure 3-1. Synchrotron XRD patterns for the as-prepared C-$FePO_4$ and Rietveld fitting results for synchrotron XRD data for the C-$FePO_4$. The wavelength was set at 0.5002 Å. Goodness-of-fit: 1.74. R_{wp}: 3.83%. R_p: 3.00%. The circles and black line denote the observed and calculated intensities, respectively. Short vertical lines indicate the positions of possible Bragg reflections. The difference between the observed and calculated profiles is shown at the bottom.

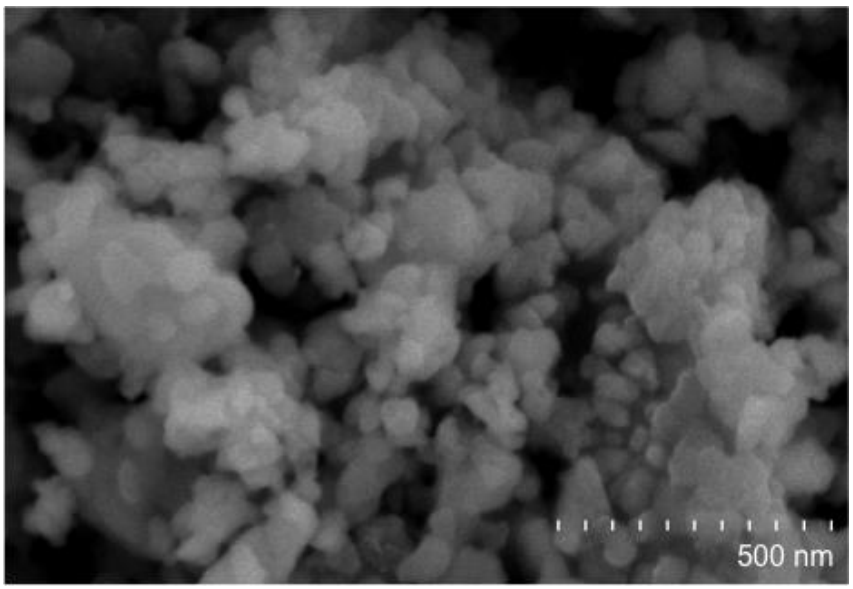

Figure 3-2. SEM image of the as-prepared C-$FePO_4$.

3-3-2. Galvanostatic and quasi-OCV measurements.

Figure 3-3 shows discharge/charge curves for the C-$FePO_4$ measured at C/30 and 55 °C. In the discharge process, the electric potential slope becomes small at -0.55 V (vs. Ag^+/Ag), and the capacity obtained for magnesium ion insertion is 147 mAh/g, which corresponds to *ca.* 0.4 Mg^{2+} ions per formula unit. In the charge process, a charge capacity of *ca.* 0.3 Mg^{2+} ions per formula unit (107 mAh/g) was obtained. The charge capacity is 40 mAh/g lower than the discharge capacity, which shows that *ca.* 0.1 Mg^{2+} ions per formula unit are not extracted from Mg_xFePO_4. This partial magnesium ion extraction from Mg_xFePO_4 is coincident with a previous report that magnesium ion insertion/extraction in $FePO_4$ is partly reversible [27]. The shape of the charge curve differs substantially from that of the discharge curve. In the initial range of charge process below 40 mAh/g, a few steps appear in the potential change. The potential slope becomes small in the range of 40 - 70 mAh/g, and finally the slope increases drastically above 70 mAh/g. The drastic increase in the potential means that some of the magnesium ions inserted in $FePO_4$ are difficult to extract from the host material. In the 2nd discharge process, the capacity is almost similar to the 1st charge capacity,

indicating that the magnesium ion extraction is more difficult than the magnesium ion insertion.

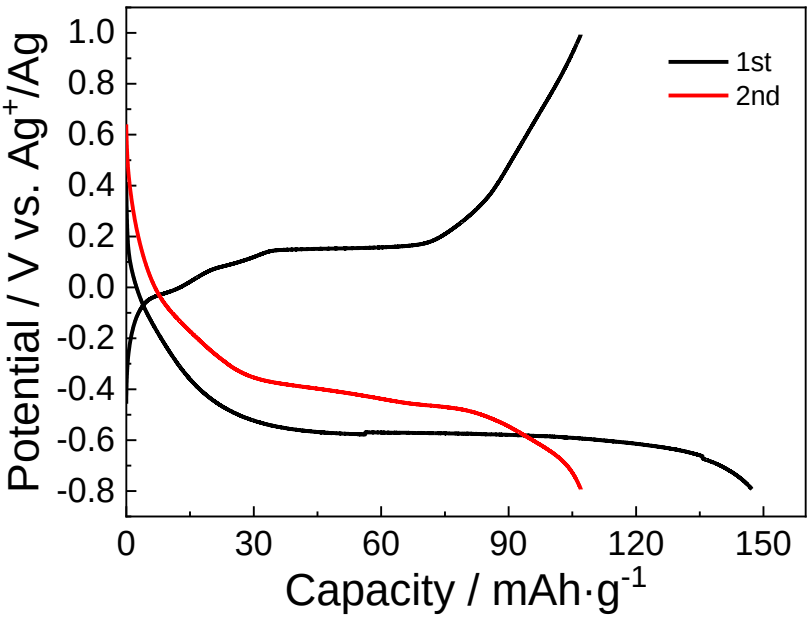

Figure 3-3. Discharge/charge curves of C-$FePO_4$ at C/30 and 55°C. The cutoff voltage was set between -0.80 V and 1.0 V vs. Ag^+/Ag.

In order to investigate the potential profile as a function of the Mg content of the $FePO_4$, we performed quasi-OCV measurements for the C-$FePO_4$ (Figure 3-4). A plateau does seem to appear in the discharge curve in Figure 3-3, but the enlarged view of the discharge process obtained from the quasi-OCV measurements (inset in Figure 3-4) show that the equilibrium potential gradually changes with magnesium ion insertion. This means that magnesium ion insertion into $FePO_4$ proceeds not by a two-phase reaction but by a single-phase reaction. During lithium ion insertion into $FePO_4$, the reaction proceeds via a two-phase process between Li-rich $Li_{1-\alpha}FePO_4$ and Li-poor $Li_\beta FePO_4$, and the equilibrium potential is very flat in the two-phase region [33,34].

In the magnesium ion extraction process, the equilibrium potential change is different from that in the insertion process. In particular, the equilibrium potentials of Mg_xFePO_4 ($0.10 < x < 0.20$) in the discharge process are 0.17-0.30 V different from those of Mg_xFePO_4 ($0.11 < x < 0.20$) in the charge process, indicating that some kind of structure

change occurs when more than 0.2 Mg^{2+} ions per formula unit are extracted from the $Mg_{0.4}FePO_4$. Similarly, different potential profiles were observed for the discharge and charge reactions for the $NaFePO_4/FePO_4$ system. In this $NaFePO_4/FePO_4$ system, it was reported that $NaFePO_4$ has to go through an intermediate $Na_{0.7}FePO_4$ state in the charge process, while in the discharge process $FePO_4$ changes directly to $NaFePO_4$ without going through an intermediate state because the activation energy for the transformation between $FePO_4$ and $Na_{0.7}FePO_4$ may be significantly larger than that for the transformation between $Na_{0.7}FePO_4$ and $NaFePO_4$ [26]. In the Mg_xFePO_4 system, an intermediate state may also appear in the charge process.

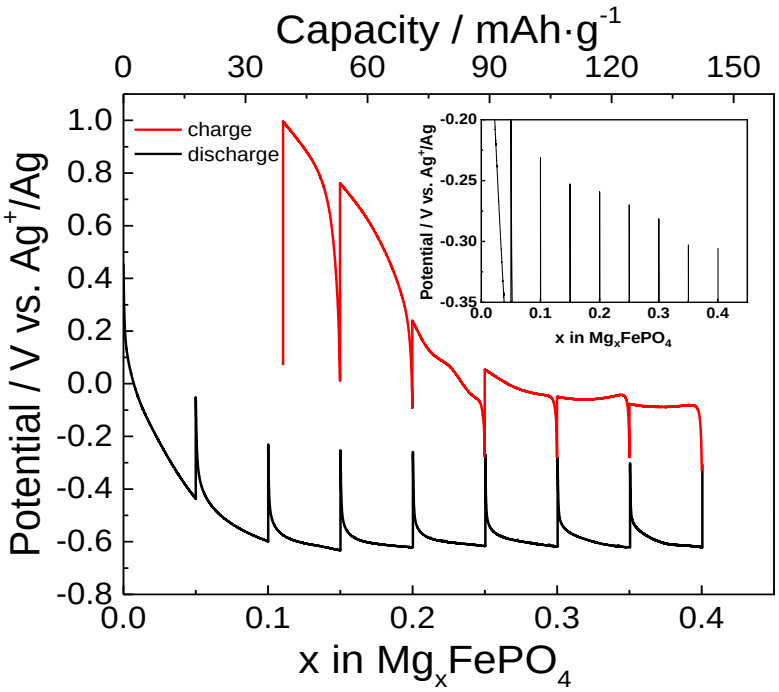

Figure 3-4. Quasi-OCV measurements of C-$FePO_4$ obtained at C/30 and 55°C. The charge process was measured for a sample in which the 0.4 Mg^{2+} ions per formula unit were inserted in constant-current mode.

3-3-3. X-ray absorption spectroscopy.

In order to confirm the contribution of Fe redox reaction of the C-$FePO_4$ to the electrochemical magnesium ion insertion/extraction process, we conducted XAS measurements of C-$FePO_4$ after both magnesium ion insertion and subsequent

extraction. The Fe *K*-edge X-ray absorption near edge structure (XANES) spectra of Mg_xFePO_4 are shown in Figure 3-5. For $FePO_4$, an edge attributed to transitions from Fe 1*s* to Fe 4*p* and to the continuum state was observed [35]. The obtained XANES spectra shifted toward the lower energy region with increasing amounts of inserted Mg^{2+}. This shift to lower energy means that the Fe ions in $FePO_4$ are reduced. Subsequently, the obtained XANES spectrum shifted to higher energy region with magnesium ion extraction, showing that the Fe ions were oxidized. Comparing the XANES spectra of Mg_xFePO_4 with that of FeO and Fe_2O_3 (Figure 3-5 (c)) also confirms that the Fe redox reaction with magnesium ion insertion/extraction. These results prove the contribution of the Fe redox reaction of the C-$FePO_4$ to the electrochemical magnesium ion insertion/extraction process. The During the lithium ion extraction from $FePO_4$, a clear isosbestic point appears at about 7127 eV, indicating a two-phase reaction between $Li_{1-\alpha}FePO_4$ and $Li_\beta FePO_4$ [36]. However, no clear isosbestic point appears during the magnesium ion insertion/extraction in $FePO_4$. Hence, it is supposed that the magnesium ion insertion/extraction reaction does not proceed via a two-phase reaction.

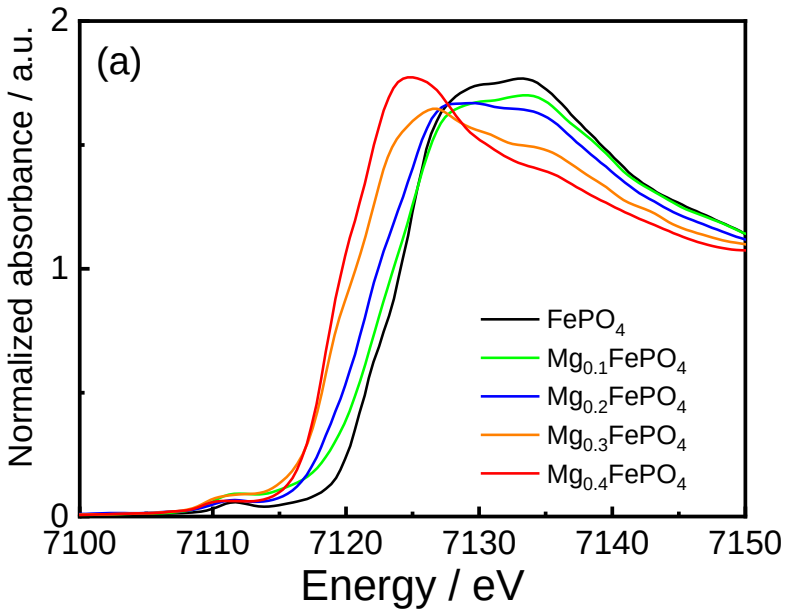

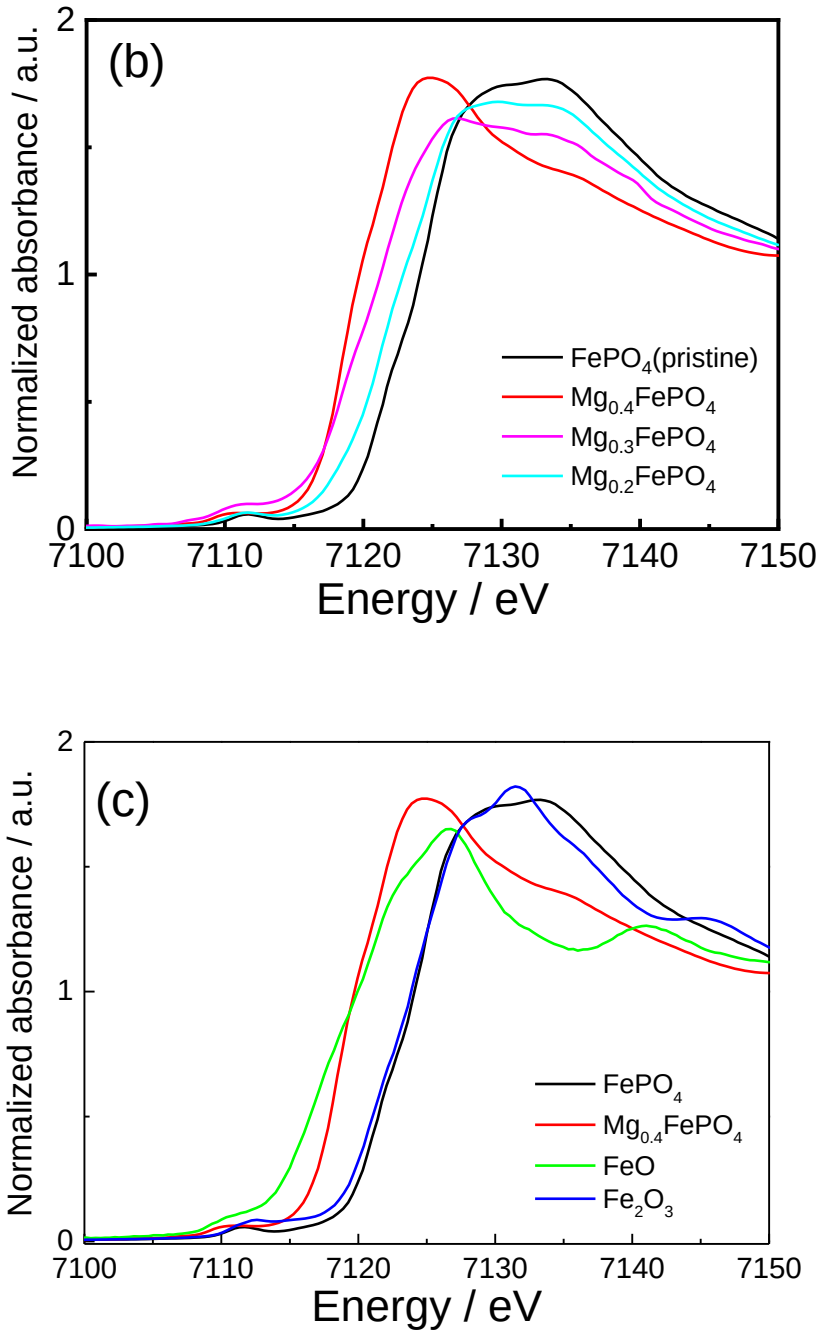

Figure 3-5. XANES spectra of Mg_xFePO_4 (x = 0 - 0.4) at the Fe *K*-edge after magnesium ion (a) insertion and (b) extraction. (c) XANES spectra of $FePO_4$, $Mg_{0.4}FePO_4$, FeO and Fe_2O_3 at the Fe *K*-edge as the references.

3-3-4. Synchrotron X-ray diffraction

To investigate the crystal structure change of Mg_xFePO_4 during magnesium ion insertion/extraction, we performed synchrotron XRD measurements of discharged and charged Mg_xFePO_4 samples. Figure 3-6 shows the XRD patterns from 5° to 15°, and Figure 3-7 shows the unit cell parameters obtained from the fitting profiles of Mg_xFePO_4 (x = 0, 0.1, 0.2, 0.4). A few extra peaks attributed to the platinum meshes appear in the profiles, but all other peaks are indexed to the orthorhombic *Pnma* space group. No peaks attributed to a second phase were observed for the magnesium ion insertion/extraction, unlike the case for lithium ion insertion into $FePO_4$. The peaks of $FePO_4$ shifted slightly toward lower angles as magnesium ions were inserted, indicating an expansion of the $FePO_4$ lattice. Subsequently, the peaks of $Mg_{0.4}FePO_4$ shifted toward higher angles during magnesium ion extraction, indicating shrinkage of the $Mg_{0.4}FePO_4$ lattice. The lattice constants are almost proportional to the amount of inserted magnesium ions, following Vegard's law (Figure 3-7). Thus, magnesium ion insertion/extraction in $FePO_4$ proceeds via a solid-solution reaction, unlike the two-phase reaction observed for lithium ion insertion. In addition, half maximum of the several peaks of the Mg_xFePO_4 were almost constant regardless of the composition of magnesium ions (Figure 3-8). This result also supports that the reaction of magnesium ion insertion/extraction in $FePO_4$ proceeds via a single-phase. This conclusion is consistent with the results of the discharge/charge measurement and the changes in the XANES spectra. Figure 3-7 also shows that the lattice constants of $Mg_{0.2}FePO_4$ after 1st discharge is different that of $Mg_{0.2}FePO_4$ after 1st charge. This result means that the crystal structure of $FePO_4$ changes during magnesium ion insertion/extraction process.

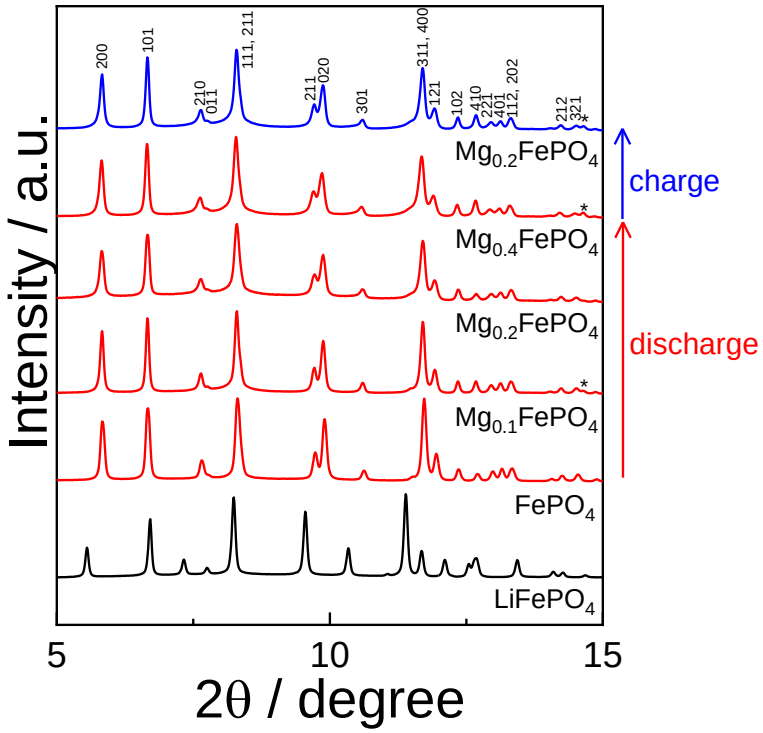

Figure 3-6. XRD patterns of Mg_xFePO_4 (x = 0 - 0.4) during Mg ion insertion/extraction and of the prepared C-$LiFePO_4$ as a reference in the range from 5° to 15°. The wavelength was set at *ca.* 0.500 Å. The stars mean extra peaks attributed to the platinum mesh.

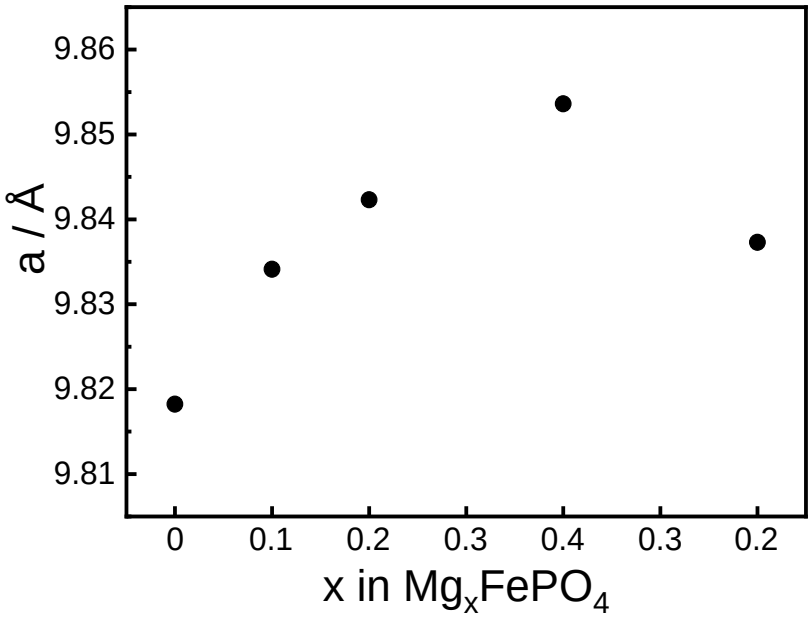
9.86
9.85
9.84
9.83
9.82
9.81
a / Å
0
0.1
0.2
0.3
0.4
0.3
0.2
x in Mg_xFePO_4

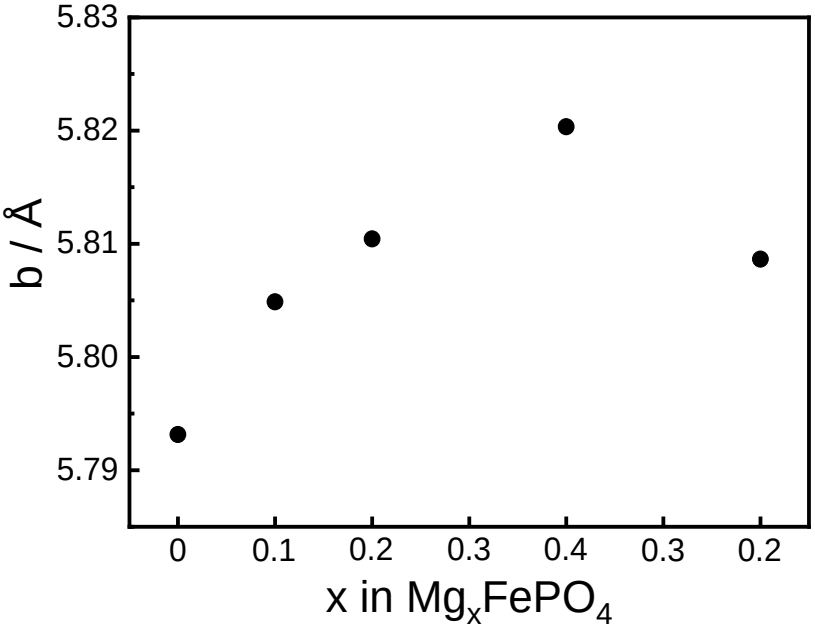
5.83
5.82
5.81
5.80
5.79
b / Å
0
0.1
0.2
0.3
0.4
0.3
0.2
x in Mg_xFePO_4

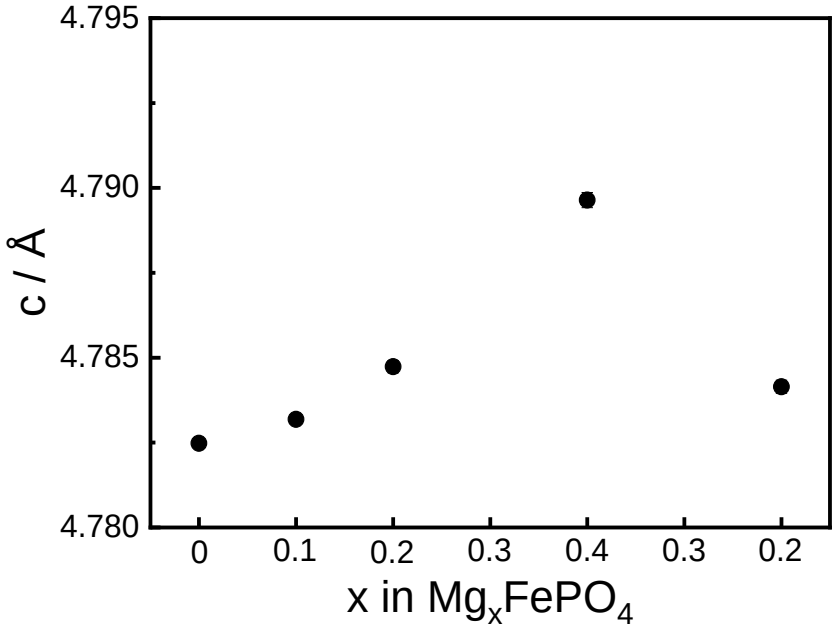

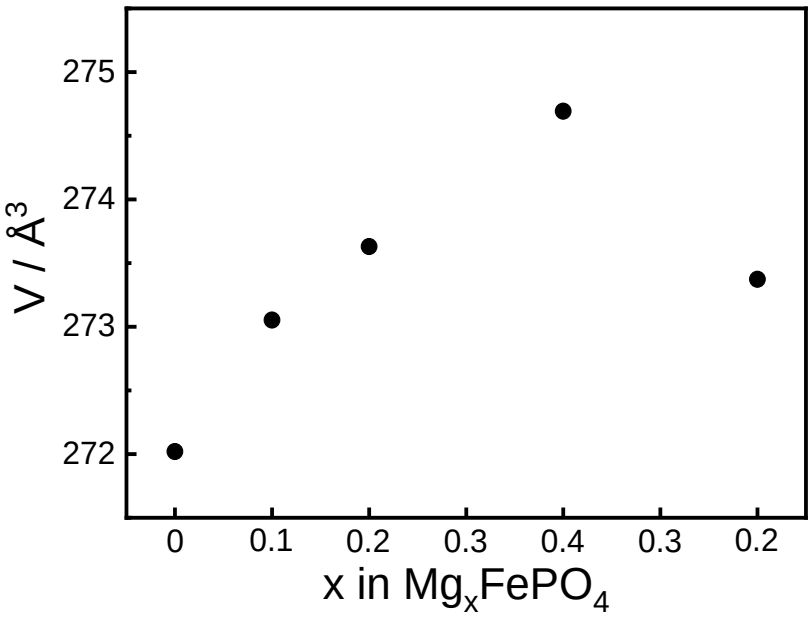

Figure 3-7. Unit cell parameters (*a*, *b* and *c*) and volume as functions of x in Mg_xFePO_4 (x = 0 - 0.4).

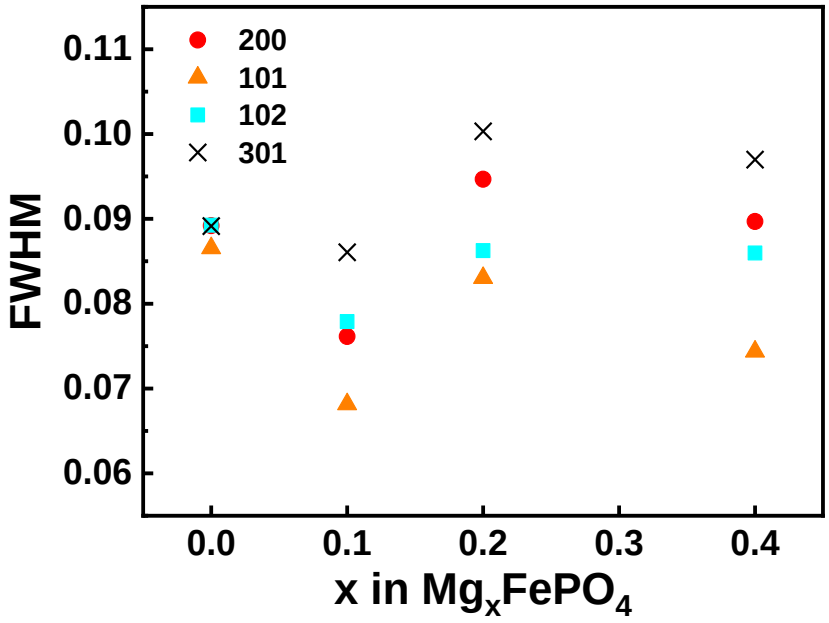

Figure 3-8. The FWHM of the several peaks of the XRD patterns of the Mg_xFePO_4 (x = 0 - 0.4) during Mg ion insertion/extraction.

The cell volumes of the $FePO_4$, $LiFePO_4$, and $Mg_{0.5}FePO_4$ extrapolated from the obtained experimental results are 272 $Å^3$, 291 $Å^3$, and 275 $Å^3$ (Figure 3-9). The point for $Mg_{0.5}FePO_4$ is extrapolated from the obtained experimental results of Mg_xFePO_4 (x=0, 0.1, 0.2, 0.4) in Figure 3-7. The cell volume change from $FePO_4$ to $Mg_{0.5}FePO_4$ is thus 1.1%, which is much smaller than that from $FePO_4$ to $LiFePO_4$ (6.9%). This is because the inserted magnesium ions attract the oxygen atoms in $FePO_4$ more strongly than lithium ions because of their higher electron density as shown in Figure 3-10. Thus, the mismatch between the cell volumes of $FePO_4$ and Mg_xFePO_4 is so small that Mg_xFePO_4 exists as a solid-solution phase without any phase separation like that seen during lithium ion insertion/extraction in $FePO_4$. The difficulty of magnesium ion extraction might cause crystal structure change of the host structure, $FePO_4$ during magnesium ion insertion/extraction. The XRD peaks obtained from the $Mg_{0.4}FePO_4$ after the second discharge were weaker and broader than those of the $Mg_{0.4}FePO_4$ after the first discharge process (Figure 3-11). This means that the crystal structure of $FePO_4$

was distorted due to magnesium ion insertion/extraction. The different quasi-OCV during the discharge and charge processes (shown in Figure 3-4) supports that some kind of structure change occurred during the charge process. Because the coulombic interactions between magnesium ions and oxygen anions in the host structure are very strong, magnesium ion extraction becomes difficult once the magnesium ions are inserted into the host structure.

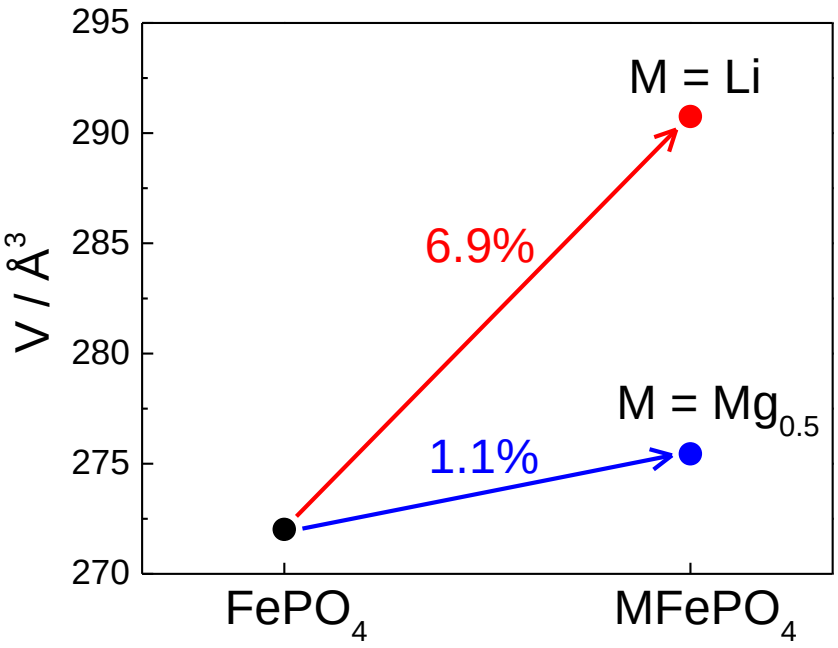

Figure 3-9. Unit cell volume of $FePO_4$, $LiFePO_4$ and $Mg_{0.5}FePO_4$. The point for $Mg_{0.5}FePO_4$ is extrapolated from the obtained experimental results of Mg_xFePO_4 (x=0, 0.1, 0.2, 0.4) in Figure 3-7.

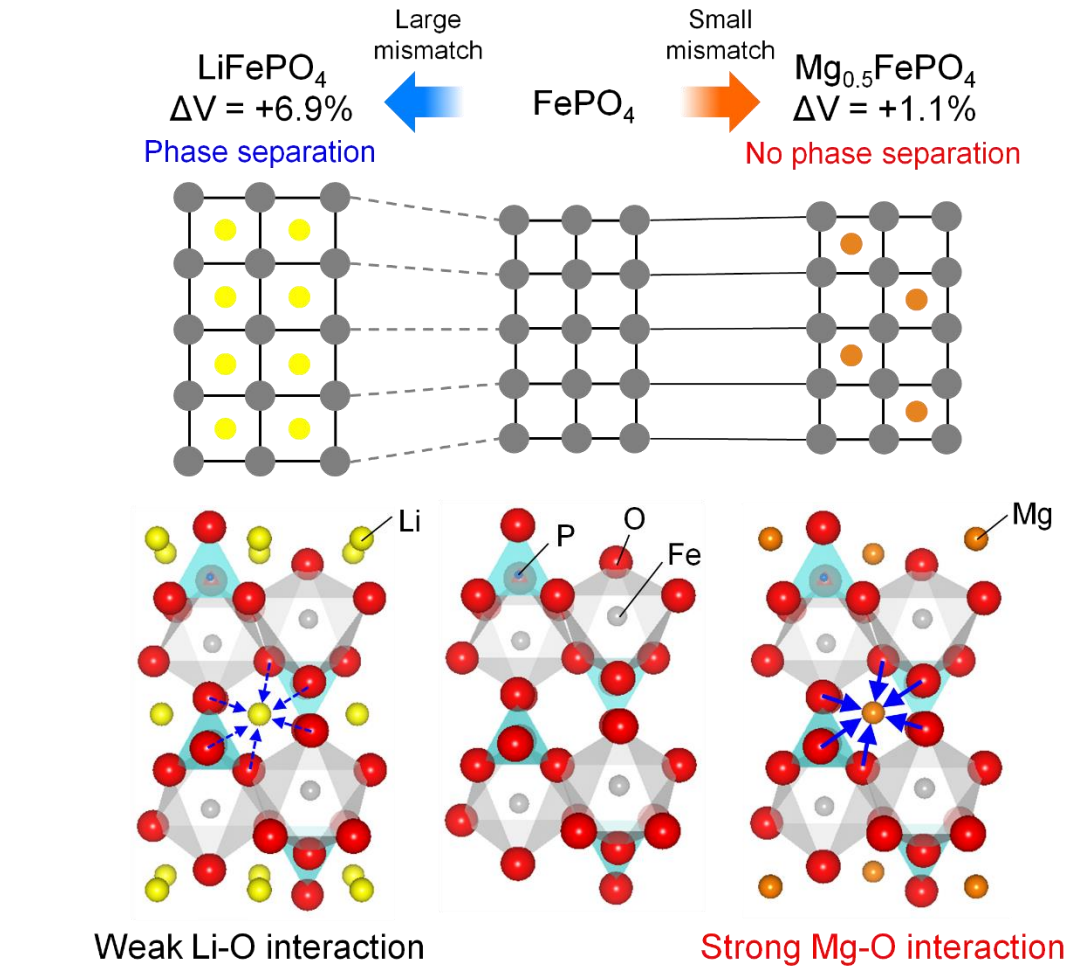

Figure 3-10. Schematic illustration comparing the volume expansion of the $FePO_4$ upon lithium ion and magnesium ion insertion. The bottom figures are drawn by using the VESTA package [37]. For lithium ion insertion, the reaction proceeds by the two-phase reaction because weaker Li-O interaction causes large lattice mismatch between $FePO_4$ and $LiFePO_4$. For magnesium ion insertion, the reaction proceeds by the single-phase because stronger Mg-O interaction suppresses the lattice mismatch between $FePO_4$ and $Mg_{0.5}FePO_4$.

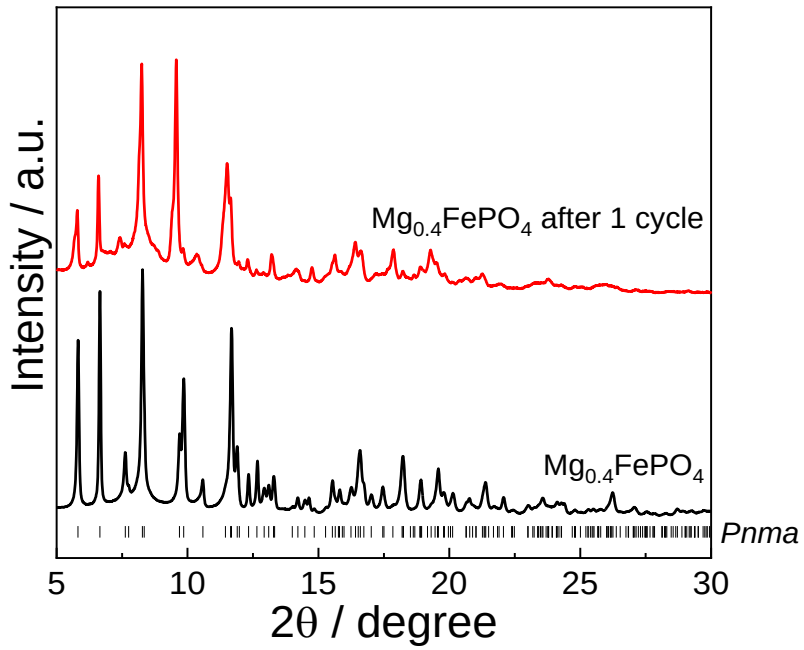

Figure 3-11. XRD profiles of the $Mg_{0.4}FePO_4$ after the first discharge and after one cycle (second discharge). The wavelength was set at 0.5004 Å for the $Mg_{0.4}FePO_4$ after one cycle.

3-4. Conclusions

In summary, we examined the electrochemical magnesium ion insertion/extraction of $FePO_4$. Compared with magnesium ion insertion, it is more difficult to extract magnesium ion from Mg_xFePO_4. The quasi-OCV measurements show that the equilibrium potential gradually changes with magnesium ion insertion. The synchrotron XRD shows only peak shift during magnesium ion insertion/extraction without the second phase formation. The magnesium ion insertion/extraction reaction in $FePO_4$ proceeds not by a two-phase reaction but by a single-phase reaction. The lattice constant changes of $FePO_4$ with inserted magnesium ions are smaller than those of lithium ions due to the strong interaction of magnesium ion, which is why the reaction proceeds in a single phase.

3-5. References

[1] J. O. Besenhard and M. Winter, “Advances in battery technology: rechargeable magnesium batteries and novel negative-electrode materials for lithium ion batteries.” *ChemPhysChem*. **3,** 155-159, (2002).

[2] D. Aurbach, Y. Cohen and M. Moshkovich, “The Study of Reversible Magnesium Deposition by *In Situ* Scanning Tunneling Microscopy.” *Electrochem. Solid-State Lett.* **4**, A113-A116, (2001).

[3] M. Matsui, “Study on electrochemically deposited Mg metal.” *J. Power Sources*. **196**, 7048-7055, (2011).

[4] D. Aurbach, Z. Lu, A. Schechter, Y. Gofer, H. Gizbar, R. Turgeman, Y. Cohen, M. Moshkovich and E. Levi, “Prototype systems for rechargeable magnesium batteries.” *Nature*. **407**, 724-727, (2000).

[5] E. Levi, M. D. Levi, O. Chasid and D. Aurbach, “A review on the problems of the solid state ions diffusion in cathodes for rechargeable Mg batteries.” *J. Electroceram.* **22**, 13-19, (2009).

[6] D. Aurbach, G. S. Suresh, E. Levi, A. Mitelman, O. Mizrahi, O. Chusid and M. Brunelli, “Progress in Rechargeable Magnesium Battery Technology.” *Adv. Mater.* **19**, 4260-4267, (2007).

[7] E. Levi and D. Aurbach, “Chevrel Phases, $M_xMo_6T_8$ (M = Metals, T = S, Se, Te) as a Structural Chameleon: Changes in the Rhombohedral Framework and Triclinic Distortion.” *Chem. Mater.* **22**, 3678-3692, (2010).

[8] D. B. Le, S. Passerini, F. Coustier, J. Guo, T. Soderstrom, B. B. Owens and W. H. Smyrl, “Intercalation of Polyvalent Cations into V_2O_5 Aerogels.” *Chem. Mater.* **10**, 682-684, (1998).

[9] D. Imamura, M. Miyayama, M. Hibino and T. Kudo, “Mg Intercalation Properties into V_2O_5 gel/Carbon Composites under High-Rate Condition.” *J. Electrochem. Soc.* **150**, A753-A758, (2003).

[10] Z.-L. Tao, L.-N. Xu, X.-L. Gou, J. Chen and H.-T. Yuan, “TiS_2 nanotubes as the cathode materials of Mg-ion batteries.” *Chem. Commun.* **18**, 2080-2081 (2004).

[11] Y. Liang, R. Feng, S. Yang, H. Ma, J. Liang and J. Chen, “Rechargeable Mg batteries with graphene-like MoS_2 cathode and ultrasmall Mg nanoparticle anode.” *Adv. Mater.* **23**, 640-643, (2011).

[12] R. Zhang, X. Yu, K.-W. Nam, C. Ling, T. S. Arthur, W. Song, A. M. Knapp, S. N. Ehrlich, X.-Q. Yang and M. Matsui “α-MnO_2 as a cathode material for rechargeable Mg batteries.” *Electrochem. Commun.* **23**, 110-113, (2012).

[13] S. Okamoto, T. Ichitsubo, T. Kawaguchi, Y. Kumagai, F. Oba, S. Yagi, K. Shimokawa, N. Goto, T. Doi and E. Matsubara, *Adv. Sci.* **2**, 1500072, (2015).

[14] T. Mandai, K. Tatesaka, K. Soh, H. Masu, A. Choudhary, Y. Tateyama, R. Ise, H. Imai, T. Takeguchi and K. Kanamura, Phys. Chem. Chem. Phys. 21 (2019) 12100.

[15] T. Hatakeyama, N. L. Okamoto, K. Shimokawa, H. Li, A. Nakao, Y. Uchimoto, H. Tanimura, T. Kawaguchi and T. Ichitsubo, *Phys. Chem. Chem. Phys.* 21 (2019) 23749.

[16] A. K. Padhi and K. S. Nanjundaswamy, “Phospho-olivines as Positive-Electrode Materials for Rechargeable Lithium Batteries.” *J. Electrochem. Soc.* **144**, 1188-1194, (1997).

[17] Y. Orikasa, T. Masese, Y. Koyama, T. Mori, M. Hattori, K. Yamamoto, T. Okado, Z.-D. Huang, T. Minato, C. Tassel, J. Kim, Y. Kobayashi, T. Abe, H. Kageyama and Y. Uchimoto, “High energy density rechargeable magnesium battery using earth-abundant and non-toxic elements.” *Sci. Rep.* **4**, 5622, (2014).

[18] Z.-D. Huang, T. Masese, Y. Orikasa, T. Mori, T. Minato, C. Tassel, Y. Kobayashi, H. Kageyama and Y. Uchimoto, “$MgFePO_4F$ as a feasible cathode material for magnesium batteries.” *J. Mater. Chem. A.* **2**, 11578-11582, (2014).

[19] A. Yamada, H. Koizumi, S.-J. Nishimura, N. Sonoyama, R. Kanno, M. Yonemura, T. Nakamura and Y. Kobayashi, “Room-temperature miscibility gap in Li_xFePO_4.” *Nat. Mater.* **5**, 357-360, (2006).

[20] N. Meethong, H.-Y. S. Huang, W. C. Carter and Y.-M. Chiang, “Size-Dependent Lithium Miscibility Gap in Nanoscale $Li_{1-x}FePO_4$.” *Electrochem. Solid-State Lett.* **10**, A134-A138, (2007).

[21] G. Kobayashi, S.-I. Nishimura, M.-S. Park, R. Kanno, M. Yashima, T. Ida and A. Yamada, “Isolation of Solid Solution Phases in Size-Controlled Li_xFePO_4 at Room Temperature.” *Adv. Funct. Mater.* **19**, 395-403, (2009).

[22] F. Omenya, N. A. Chernova, R. Zhang, J. Fang, Y. Huang, F. Cohen, N. Dobrzynski, S. Senanayake, W. Xu and M. S. Whittingham, “Why Substitution Enhances the Reactivity of $LiFePO_4$.” *Chem. Mater.* **25**, 85-89, (2013).

[23] P. Moreau, D. Guyomard, J. Gaubicher and F. Boucher, “Structure and Stability of Sodium Intercalated Phases in Olivine $FePO_4$.” *Chem. Mater.* **22**, 4126-4128, (2010).

[24] Y. Zhu, Y. Xu, Y. Liu, C. Luo and C. Wang, “Comparison of electrochemical performances of olivine $NaFePO_4$ in sodium-ion batteries and olivine $LiFePO_4$ in lithium-ion batteries.” *Nanoscale*. **5**, 780-787, (2013).

[25] M. Casas-Cabanas, V. V. Roddatis, D. Saurel, P. Kubiak, J. Carretero-González, V. Palomares, P. Serras and T. Rojo, “Crystal chemistry of Na insertion/deinsertion in $FePO_4$-$NaFePO_4$.” *J. Mater. Chem.* **22**, 17421-17423, (2012).

[26] J. Lu, S. C. Chung, S.-I. Nishimura and A. Yamada, “Phase Diagram of Olivine Na_xFePO_4 ($0 < x < 1$)” *Chem. Mater.* **25**, 4557-4565, (2013).

[27] N. Le Poul, E. Baudrin, M. Morcrette and S. Gwizdala, “Development of potentiometric ion sensors based on insertion materials as sensitive element.” *Solid State Ionics*. **159**, 149-158, (2003).

[28] G. Oyama, S. Nishimura, S. C. Chung, M. Okubo and A. Yamada, *Electrochemistry* 82(10) (2014) 855.

[29] C. Ling, D. Banerjee, W. Song, M. Zhang and M. Matsui, “First-principles study of the magnesiation of olivines: redox reaction mechanism, electrochemical and thermodynamic properties.” *J. Mater. Chem.* **22**, 13517-13523, (2012).

[30] S. Yagi, A. Tanaka, Y. Ichikawa, T. Ichitsubo and E. Matsubara, “Electrochemical Stability of Magnesium Battery Current Collectors in a Grignard Reagent-Based Electrolyte.” *J. Electrochem. Soc.* **160**, C83-C88, (2013).

[31] V. Petricek, M. Dusek and L. Palatinus, “JANA2006: The Crystallographic Computing System; Institute of Physics: Praha.” *Czech Republic*. (2006).

[32] A. Yamada, H. Koizumi, N. Sonoyama and R. Kanno, “Phase Change in Li_xFePO_4.” *Electrochem. Solid-State Lett.* **8**, A409-A413, (2005).

[33] Y. Zhu and C. Wang, “Galvanostatic Intermittent Titration Technique for Phase-Transformation Electrodes.” *J. Phys. Chem. C*. **114**, 2830-2841, (2010).

[34] T. Sasaki, Y. Ukyo and P. Novák, “Memory effect in a lithium-ion battery.” *Nat. Mater.* **12**, 569-575, (2013).

[35] A. Deb, U. Bergmann, E. J. Cairns and S. P. Cramer, “X-ray absorption spectroscopy study of the Li_xFePO_4 cathode during cycling using a novel electrochemical in situ reaction cell.” *J. Synchrotron Radiat.* **11**, 497-504, (2004).

[36] Y. Orikasa, T. Maeda, Y. Koyama, H. Murayama, K. Fukuda, H. Tanida, H. Arai, E. Matsubara, Y. Uchimoto and Z. Ogumi, “Transient Phase Change in Two Phase Reaction between $LiFePO_4$ and $FePO_4$ under Battery Operation.” *Chem. Mater.* **25**, 1032-1039, (2013).

[37] K. Momma and F. Izumi, “VESTA 3 for three-dimensional visualization of crystal, volumetric and morphology data.” *J. Appl. Cryst.* **44**, 1272-1276, (2011).

Chapter 4. Relationship between kinetics and electronic/structural changes during oxide ions redox of lithium-rich 4d/3d transition metal oxides

4-1. Introduction

Electronic devices and transportations are leading approach to suppress the greenhouse effect gas emission, and it is significant to achieve the development of larger energy storage system [1-3]. Lithium ion batteries (LIBs) have been commercialized for a quarter of century as a power source of portable electric devices such as mobile phones. LIBs are also attractive for high-energy storage system because of their highest gravimetric and volumetric and gravimetric energy density [1-3].

However, the energy density is severely restricted by the capacity of cathode materials. The typical commercialized cathode materials such as $LiCoO_2$ have already reached to the theoretical limit [4-6]. Lithium rich materials have the attention as the next generation cathodes because of their higher theoretical capacity by the presence of 'excess' lithium ion in the transition metal layer. Thackeray et al. have reported Li-rich solid solution materials, $Li_{1.2}Ni_{0.13}Co_{0.13}Mn_{0.54}O_2$ ($0.5Li_2MnO_3$-$0.5LiNi_{1/3}Co_{1/3}Mn_{1/3}O_2$) shows higher capacity than that of the conventional layered oxides [7,8]. During the charge reaction, 3*d* transition metal mainly contributes to the charge compensation of lithium ion extraction in the typical cathodes. On the other hand, in the Li-rich manganese layered oxide, $Li_{1.2}Ni_{0.13}Co_{0.13}Mn_{0.54}O_2$, shows a large capacity [7-22], which cannot be explained by the oxidization of 3*d* transition metal Co and Ni and Mn [9,10]. At the high voltage in the 1st charge reaction process, an oxygen redox and/or an oxygen evolution (oxygen loss from the lattice) reaction occur, which contributes to the charge compensation [10, 11, 12]. However, these oxygen reactions trigger a crystal rearrangement or cation migration [13,14] or oxygen evolution reaction, which limits the practical use of this cathode [15]. The origin of the irreversible reaction may be caused by the formation of a ligand hole and/or an oxygen evolution [15,19,22]. One of the main problem of the materials for practical use is low rate capability. Li et al. have

reported that oxygen loss could be attributed to the high kinetic barriers because low Li^+ diffusion coefficients in the plateau region [21]. So the rate performance of Mn-based solid solution cathode still needs to be improved.

In order to stabilize the anionic redox and improve the rate performance, the use of Li-rich layered material with 4*d* transition metal is an attractive approach. By the strong overlap between Ru-4*d* and O-2*p* orbitals, containing 4*d* transition metal Li-rich cathode Li_2RuO_3 has illustrated good cycle stability [23-28]. Li_2RuO_3 and Ru-based Li-rich cathode materials show typical two plateau during the 1st charge-discharge reaction. The first plateau area is attributed to transition metals, which is mainly Ru redox reaction ($Ru^{4+} \leftrightarrow Ru^{5+}$), and the other plateau area is oxygen redox [23-28]. The presence of Ru ions also could enhance the rate capability [23].

Containing only 3*d* transition metals oxide, the hole formation reaction on O-2*p* orbitals and oxygen evolution reaction occurred simultaneously. However, in case of containing 4*d* transition metals oxide, the hole formation reaction occurred on the electronic bands because of the wide band structure of 4*d* transition metals. In order to clarify the reason of polarization, relationship between the local distortions during charge-discharge must be clarified.

In this work, we investigated what is the major factor to determine the rate capability in Li-rich cathode materials. We synthesized two types Li-rich layered cathode materials; $Li_{1.2}Ni_{0.13}Co_{0.13}Mn_{0.54}O_2$ containing 3*d* transition metals, and $Li_{1.2}Ni_{0.13}Co_{0.13}Ru_{0.54}O_2$ containing 3*d* and 4d transition metals. We measured the electrochemical properties of the $Li_{1.2}Ni_{0.13}Co_{0.13}Mn_{0.54}O_2$ cathode and the $Li_{1.2}Ni_{0.13}Co_{0.13}Ru_{0.54}O_2$ cathode, discussed the relationship among electrochemical performance, charge compensation mechanism and local structure changes. The $Li_{1.2}Ni_{0.13}Co_{0.13}Ru_{0.54}O_2$ cathode material indicates a higher rate performance and better reversibility compared to the $Li_{1.2}Ni_{0.13}Co_{0.13}Mn_{0.54}O_2$ cathode due to the reversible charge compensation of Ru, Ni, and Co, and a strong overlap between the Ru-4*d* and O-2*p* orbitals. The result of Soft X-ray Absorption Spectroscopy (XAS) suggests that the formation of a localized hole on O-2*p* orbital is restrained, which contributes to improve the stability and rate performance during the 1st charge/discharge reaction. $Li_{1.2}Ni_{0.13}Co_{0.13}Ru_{0.54}O_2$ cathode also had less distorted local structure than that of

$Li_{1.2}Ni_{0.13}Co_{0.13}Mn_{0.54}O_2$ cathode, which takes advantage for Li diffusion and it showed the high rate performance.

4-2. Experimental

4-2-1. Synthesis

The powder of $Li_{1.2}Ni_{0.13}Co_{0.13}Mn_{0.54}O_2$ was synthesized by the polymerized complex method as previously reported [29]. First, stoichiometric nickel acetate tetrahydrate, cobalt acetate tetrahydrate, lithium acetate and manganese acetate tetrahydrate were dissolved into nitric acid aqueous solution. Then excess citric acid and ethylene glycol were added into the solution and mixed at 200 rpm at 200 ^oC until finished polymerization well. After the polymerization, obtained black gel was calcined at 400 ^oC for 3 hours to make precursor powder. The precursor powder was pelletized and burnt at 850 ^oC for 12 hours, and then the $Li_{1.2}Ni_{0.13}Co_{0.13}Mn_{0.54}O_2$ powder was finally prepared.

$Li_{1.2}Ni_{0.13}Co_{0.13}Ru_{0.54}O_2$ was synthesized by the same method, in which ruthenium trichloride hydrate was used as the starting material instead of manganese acetate tetrahydrate. The precursor powder was pelletized and burnt at 900 ^oC for 24 hours, and then the $Li_{1.2}Ni_{0.13}Co_{0.13}Ru_{0.54}O_2$ powder was finally prepared.

4-2-2. Characterization

Synchrotron radiation X-ray powder diffraction (XRD) experiments with the Imaging Plate were carried out using a large Debye-Scherrer camera at SPring-8 BL19B2. The wavelength of the X-ray was 0.7 Å and the scannning range was between $2\theta = 2.1°$ and $2\theta = 78.1°$. The pristine powder samples were prepared by sealing in a glass capillary. Particle morphologies of the samples were observed using a scanning electron microscope (S-3400N, HITACHI).

4-2-3. Electrochemical measurement

Each compound electrode was fabricated from mixtures composed of 80 wt% active material, 10 wt% acetylene black as the conductive aid and 10 wt% polyvinilidene difluoride as the binder. The electrochemical cell consisted of a cathode,

a lithium metal anode, porous polypropylene film as a separator and 1 mol dm^{-3} $LiPF_6$ in ethylene carbonate (EC) /ethylmethyl carbonate (EMC) (3:7 by volume). The cut-off voltage was between 2.0-4.8 V vs Li/Li^+ ($Li_{1.2}Ni_{0.13}Co_{0.13}Mn_{0.54}O_2$ cathode) while 2.0-4.6 V vs Li/Li^+ ($Li_{1.2}Ni_{0.13}Co_{0.13}Ru_{0.54}O_2$ cathode). Current densities are determined by the hypothesis that all Li ion can be removed in charge-discharge process (i.e. 1C=377 mA g^{-1} in $Li_{1.2}Ni_{0.13}Co_{0.13}Mn_{0.54}O_2$ cathode and 1C=292 mAh g^{-1} in $Li_{1.2}Ni_{0.13}Co_{0.13}Ru_{0.54}O_2$ cathode). In this work, the current rate was changed at 0.03C, 0.1C, 0.5C, 1C and 3C. For galvanostatic intermittent titration technique (GITT) experiment, the cell was charged for 30 min at a rate of 0.1 C followed by residence time of 4 hours. All measurements were implemented at 25 °C.

4-2-4. X-ray Absorption Spectroscopies

The cell for the *operando* soft XAS measurement was set up to investigate oxygen redox reaction [29]. Composite electrodes were pasted on Pt-sputtered Si_3N_4 window with thickness of 100 nm. For $Li_{1.2}Ni_{0.13}Co_{0.13}Ru_{0.54}O_2$ composite electrodes, half charged-$Li_4Ti_5O_{12}$ composite electrodes, which consist of 80 wt% $Li_4Ti_5O_{12}$, 10 wt% acetylene black and 10 wt% PVdF, were used as a counter electrode, and 1 M $LiPF_6$ / acetonitrile was used as an electrolyte solution. Soft XAS measurements for O *K*-edge was performed at BL27SU in SPring-8, Japan. *operando* Hard XAS measurements for Ni *K*-edge, Co *K*-edge and Ru *K*-edge were performed at BL14B2 in SPring-8, Japan. The absorption spectra were collected with a transmission mode. Lithium foil was used as an anode, and 1 M $LiPF_6$ / EC: EMC (3:7 by volume) was used as an electrolyte solution. Laminated-type cells were assembled in the Ar-filled grove box. The absorption spectra were collected during galvanostatic measurement at a rate of 1/20 C rate at 25 °C.

4-3. Results and discussion

4-3-1. Characterization

The result of XRD pattern of $Li_{1.2}Ni_{0.13}Co_{0.13}Mn_{0.54}O_2$ and $Li_{1.2}Ni_{0.13}Co_{0.13}Ru_{0.54}O_2$ are shown in Figure 4-1(a) and (b). Both samples crystallize into a layered structure. The XRD pattern of $Li_{1.2}Ni_{0.13}Co_{0.13}Mn_{0.54}O_2$ was indexed by the *C*2/*m* space

group [23] without impurities. The $Li_{1.2}Ni_{0.13}Co_{0.13}Ru_{0.54}O_2$ was indexed by the *C2/c* space group without impurities. The scanning electron microscope (SEM) image of the prepared sample is shown in the Figure 4-1(c) and (d). Both of the cathode material powders are controlled to have a particle size of less than 1 μm, and their morphological influence on the electrochemical performance is considered to be small.

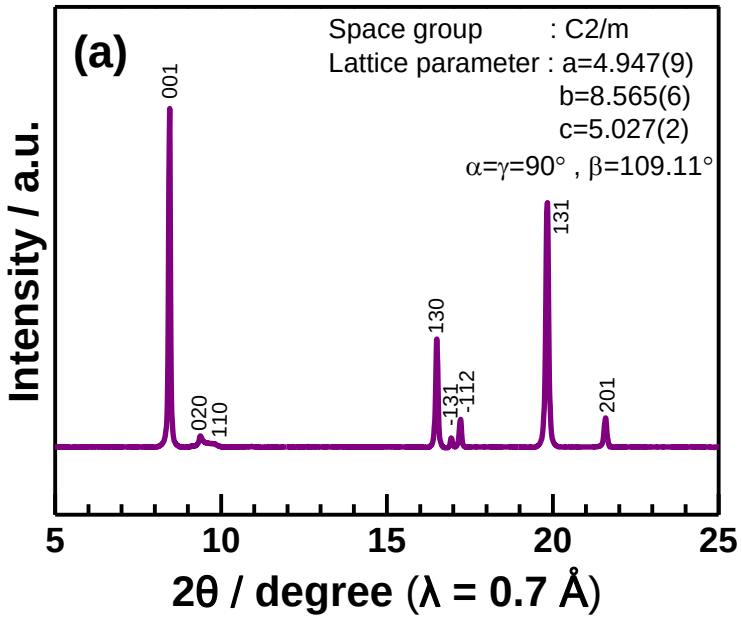

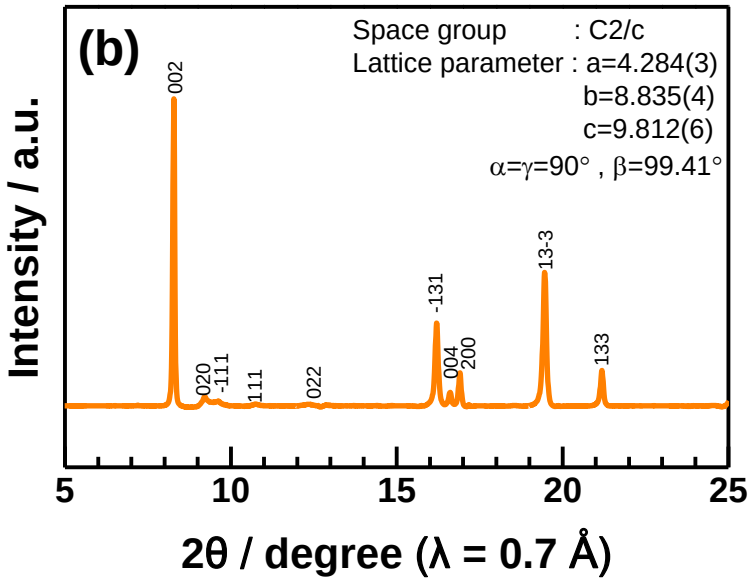

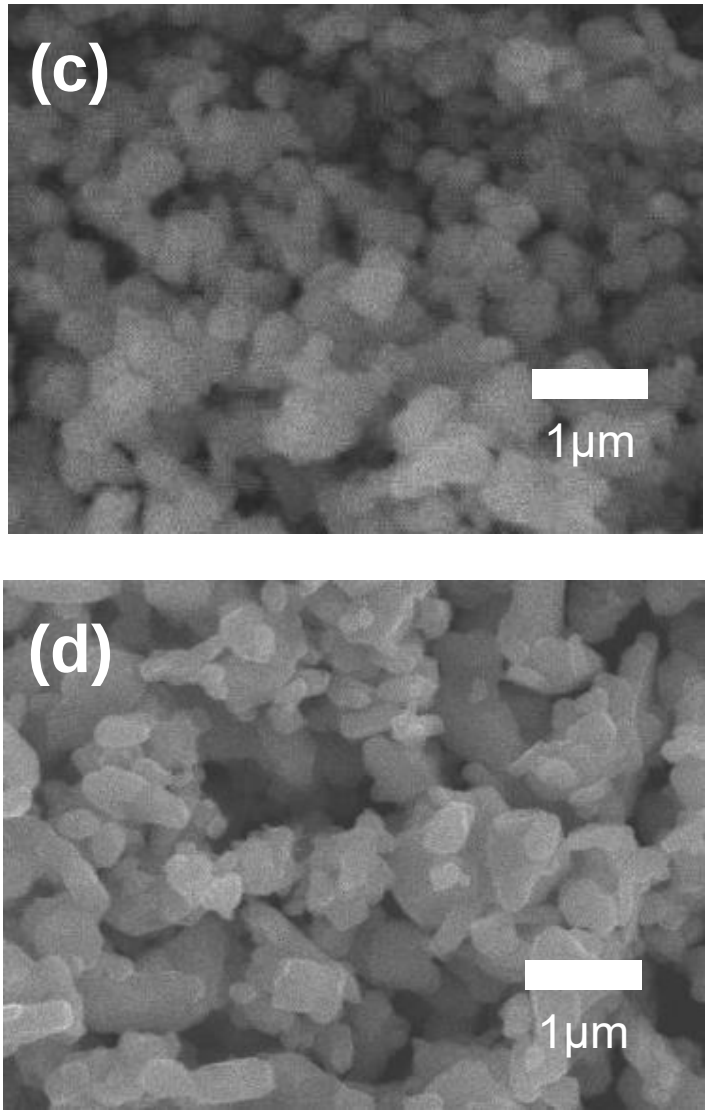

Figure 4-1: Material characterization. Synchotron X-ray diffraction patterns of (a) $Li_{1.2}Ni_{0.13}Co_{0.13}$ $Mn_{0.54}O_2$ and (b) $Li_{1.2}Ni_{0.13}Co_{0.13}$ $Ru_{0.54}O_2$. The SEM images of (c) $Li_{1.2}Ni_{0.13}Co_{0.13}Mn_{0.54}O_2$ and (d) $Li_{1.2}Ni_{0.13}Co_{0.13}Ru_{0.54}O_2$.

4-3-2. Charge and discharge measurement

Charge and discharge curves during the 1st and 2nd cycle were shown in Figure 4-2; for the case of (a) $Li_{1.2}Ni_{0.13}Co_{0.13}Mn_{0.54}O_2$ cathode and (b) $Li_{1.2}Ni_{0.13}Co_{0.13}Ru_{0.54}O_2$ cathode. The $Li_{1.2}Ni_{0.13}Co_{0.13}Mn_{0.54}O_2$ cathode showed 330 mAh g^{-1} capacity with a voltage slope by 4.5 V and a plateau at 4.5 V in the 1st charge

process. The discharge capacity rapidly decreased to 220 mAh g^{-1} in the 1st discharge process. In the second cycle, the $Li_{1.2}Ni_{0.13}Co_{0.13}Mn_{0.54}O_2$ cathode showed different charge-discharge curve from 1st cycle. These results corresponds to the previous reports [7-14].

On the other hand, in the Figure 4-2 (b), $Li_{1.2}Ni_{0.13}Co_{0.13}Ru_{0.54}O_2$ cathode showed the gradual voltage change without plateau area during the 1st charge reaction. In the 1st cycle, the charge capacity is about 240 mAh g^{-1} and the discharge capacity is about 220 mAh g^{-1}, and the reversibility is higher than $Li_{1.2}Ni_{0.13}Co_{0.13}Mn_{0.54}O_2$ cathode at 0.1 C rates. Furthermore, in the 2nd discharge process, the capacity is almost similar to the 1st charge capacity. Figure 4-3 (a) shows the 1st discharge capacity dependence on the C rate. In case of the higher C rate, both cathodes showed the capacity fade, however, the capacity of $Li_{1.2}Ni_{0.13}Co_{0.13}Mn_{0.54}O_2$ cathode faded more drastically than $Li_{1.2}Ni_{0.13}Co_{0.13}Ru_{0.54}O_2$ cathode. At the 0.1 C rate, the discharge capacity of $Li_{1.2}Ni_{0.13}Co_{0.13}Mn_{0.54}O_2$ cathode and $Li_{1.2}Ni_{0.13}Co_{0.13}Ru_{0.54}O_2$ cathode were 218 mAh g^{-1} and 220 mAh g^{-1}, respectively. And at the 3 C rate, the discharge capacity of $Li_{1.2}Ni_{0.13}Co_{0.13}Mn_{0.54}O_2$ cathode and $Li_{1.2}Ni_{0.13}Co_{0.13}Ru_{0.54}O_2$ cathode were 94 mAh g^{-1} and 140 mAh g^{-1}, respectively. Figure 4-3(b) showed GITT experiments for 1st cycle of $Li_{1.2}Ni_{0.13}Co_{0.13}Mn_{0.54}O_2$ cathode and $Li_{1.2}Ni_{0.13}Co_{0.13}Ru_{0.54}O_2$ cathode at 0.1 C current rate. Figure 4-3 (b) suggested that $Li_{1.2}Ni_{0.13}Co_{0.13}Ru_{0.54}O_2$ cathode showed smaller polarization especially in the plateau area compared with the $Li_{1.2}Ni_{0.13}Co_{0.13}Mn_{0.54}O_2$ cathode [14,21]. These results suggests that $Li_{1.2}Ni_{0.13}Co_{0.13}Ru_{0.54}O_2$ cathode has advantage of the charge-discharge process at larger current density, compared to $Li_{1.2}Ni_{0.13}Co_{0.13}Mn_{0.54}O_2$ cathode [21].

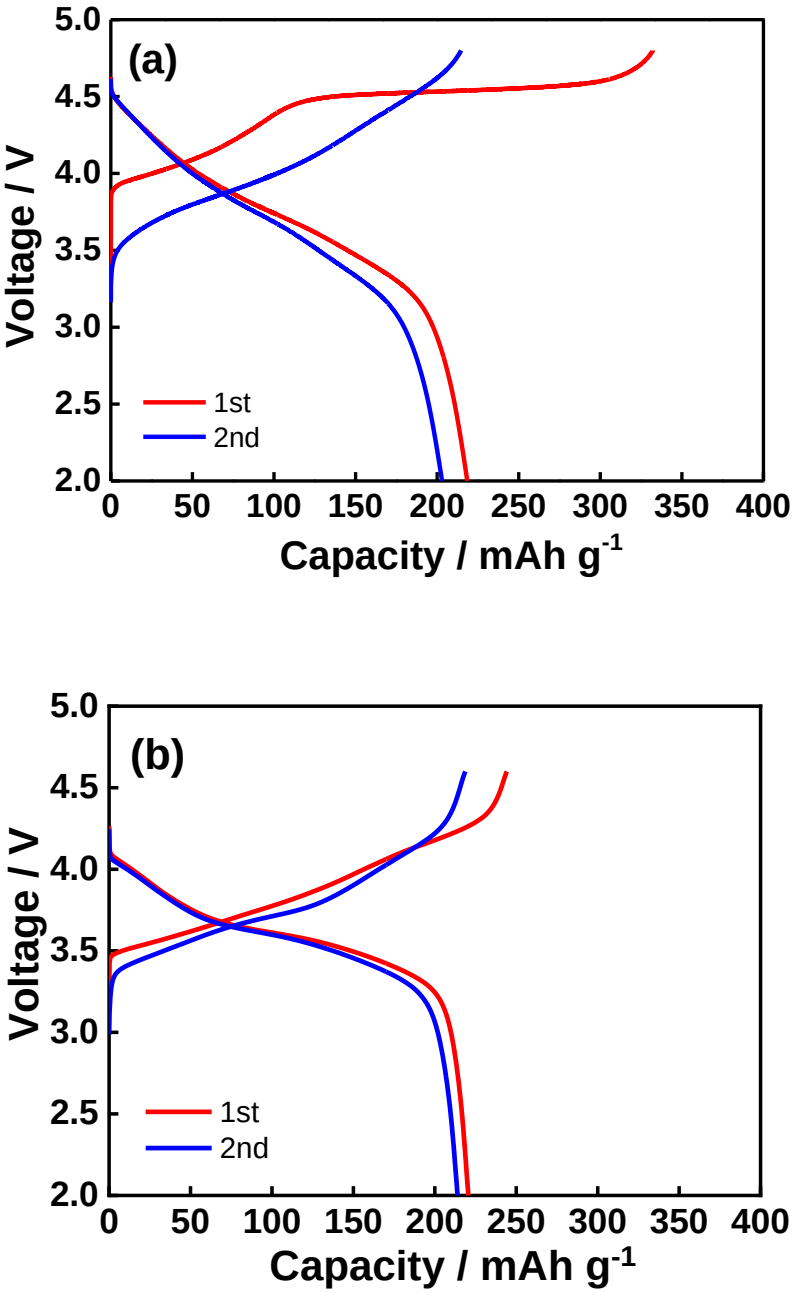

Figure 4-2. The charge-discharge curves for (a) $Li_{1.2}Ni_{0.13}Co_{0.13}Mn_{0.54}O_2$ cathode and (b) $Li_{1.2}Ni_{0.13}Co_{0.13}Ru_{0.54}O_2$ cathode measured at 0.1C rate, 25 °C.

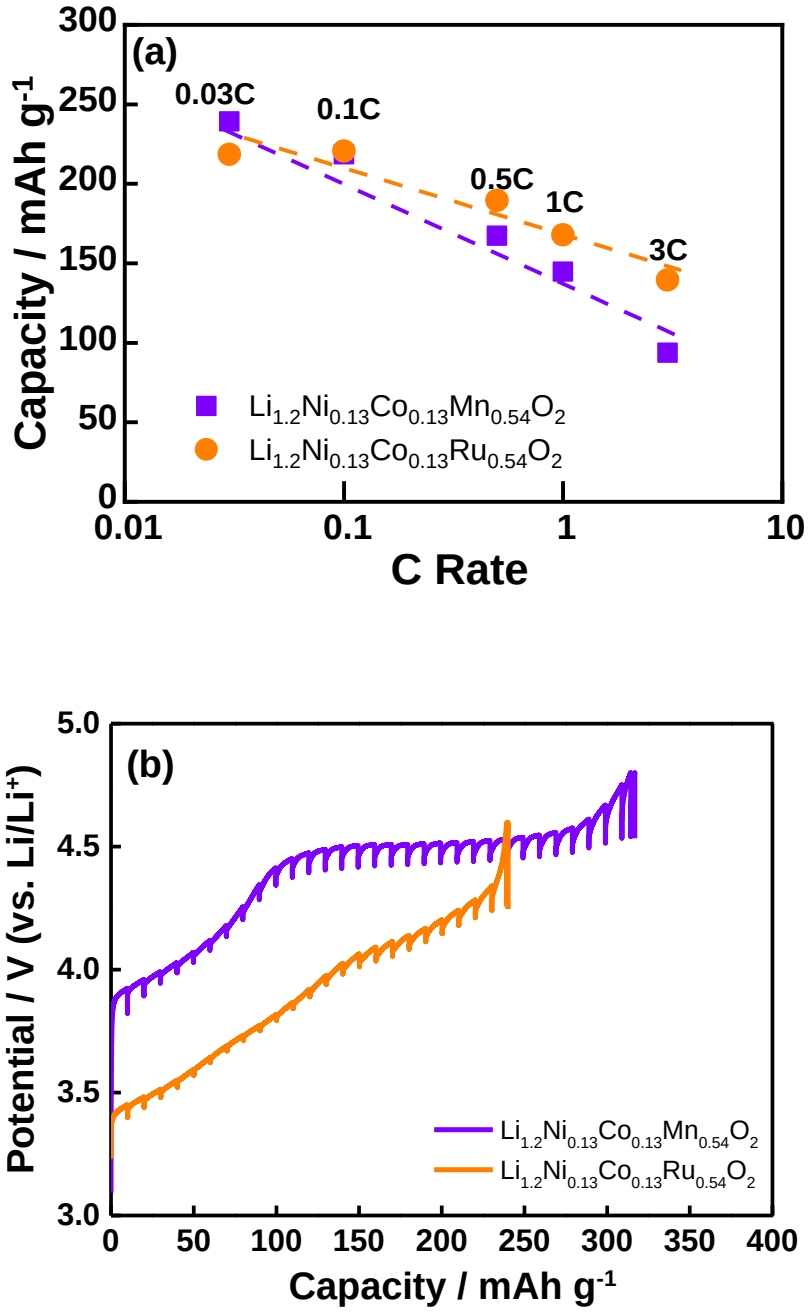

Figure 4-3. (a) Capacity dependence on C rate for $Li_{1.2}Ni_{0.13}Co_{0.13}Mn_{0.54}O_2$ cathode and $Li_{1.2}Ni_{0.13}Co_{0.13}Ru_{0.54}O_2$ cathode. (b) The GITT measurement of 1st charge process for $Li_{1.2}Ni_{0.13}Co_{0.13}Mn_{0.54}O_2$ cathode and $Li_{1.2}Ni_{0.13}Co_{0.13}Ru_{0.54}O_2$ cathode.

4-3-3. X-ray absorption spectroscopy measurement

In order to analyze the electronic structure of the cathode materials, XAFS measurements of the *K*-edge of the transition metals were performed. Figure 4-4 shows the changes of peak top energies of 1st charge-discharge Ni and Co *K*-edge XANES.
In case of $Li_{1.2-x}Ni_{0.13}Co_{0.13}Mn_{0.54}O_2$ cathode, the peak energies of Ni *K*-edge XANES spectra were shifted higher side from x = 0 (before charge) to x = 0.4 and were invariant from x = 0.4 to x = 1.1. These results meant the Ni ions contributed to charge compensation from x = 0 to x = 0.4, then did not contributed from x = 0.4 to x = 1.1. During the 1st discharge reaction, the peak energy of Ni *K*-edge XANES spectra was shifted lower side from x = 1.1 (before discharge) to x = 0.5 and were invariant from x = 0.5 to x = 0.3.

The peak energies of Co *K*-edge XANES spectra were shifted higher side from x = 0 (before charge) to x = 0.4 and were invariant from x = 0.4 to x = 1.1. These results meant the Co ions contributed to charge compensation from x = 0 to x = 0.4, then did not contributed from x = 0.4 to x = 1.1. During the discharge process, Co *K*-edge XANES spectra were invariant from x = 1.1 to x = 0.8 and were shifted lower side from x = 0.8 to x = 0.3. These results suggest that the mechanism of Ni and Co valence changes are different between 1st charge reaction and 1st discharge reaction, that is, there were large hysteresis during the 1st cycle. The tendency of valence changes of Ni and Co of $Li_{1.2}Ni_{0.13}Co_{0.13}Mn_{0.54}O_2$ were coincided with the previous results [11,15].

On the other hand, the $Li_{1.2}Ni_{0.13}Co_{0.13}Ru_{0.54}O_2$ cathode showed different tendency compared with $Li_{1.2}Ni_{0.13}Co_{0.13}Mn_{0.54}O_2$. The peak energies of Ni *K*-edge XANES spectra were shifted higher side from x = 0 (before charge) to x = 0.6 and were invariant from x = 0.6 to x = 0.9. These results meant the Ni ions contributed to charge compensation from x = 0 to x = 0.6, then did not contributed from x = 0.6 to x = 0.9. During the 1st discharge reaction, the peak energy of Ni *K*-edge XANES spectra were shifted lower energy side from x = 0.9 (before discharge) to x = 0.2.

Co *K*-edge XANES spectra were also shifted higher side from x = 0 (before charge) to x = 0.9. These results meant the Co ions contributed to charge compensation from x = 0 to x = 0.9. During the 1st discharge reaction, the peak energy of Co *K*-edge XANES spectra were shifted lower energy side from x = 0.9 (before discharge) to x =

0.2. It showed relatively reversible valence charge of Ni and Co compared with $Li_{0.7}Ni_{0.13}Co_{0.13}Mn_{0.54}O_2$, in addition, Co could contributed to charge compensation in whole 1st charge reaction. The tendency of valence changes of Ni and Co of $Li_{1.2}Ni_{0.13}Co_{0.13}Ru_{0.54}O_2$ were different, and smaller hysteresis compared with $Li_{0.7}Ni_{0.13}Co_{0.13}Mn_{0.54}O_2$ cathode.

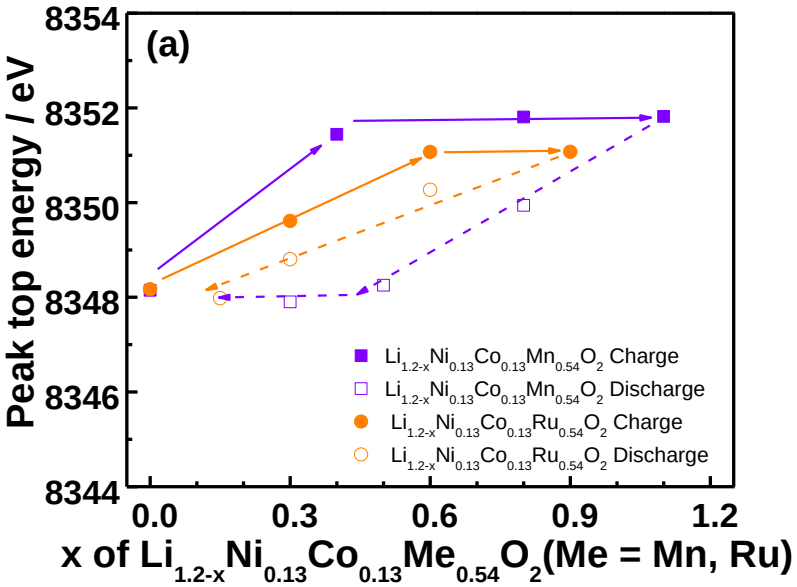

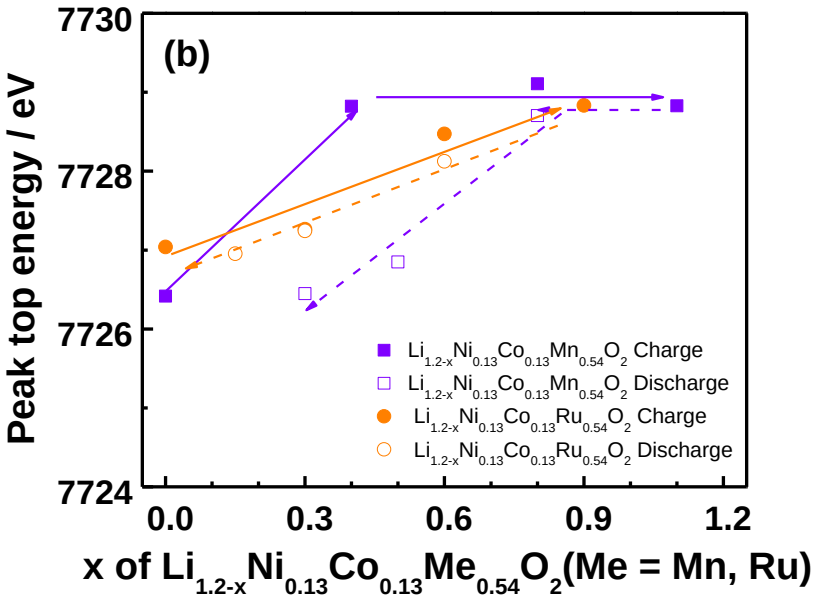

Figure 4-4. The Changes on peak top energies of XANES in 1st charge-discharge reaction for (a) Ni *K*-edge (b) Co *K*-edge in $Li_{1.2}Ni_{0.13}Co_{0.13}Mn_{0.54}O_2$ cathode and $Li_{1.2}Ni_{0.13}Co_{0.13}Ru_{0.54}O_2$ cathode.

The results of Mn *K*-edge XANES spectra of $Li_{1.2}Ni_{0.13}Co_{0.13}Mn_{0.54}O_2$ were shown in Figure 4-5 (a) and (b). It has been reported that the peak top energies of Mn *K*-edge XANES changes during the charge-discharge process, but it is due to the strain of MnO_6 [11]. Therefore, the valence of Mn was tetravalent at the pristine state [9,11,15] and during the 1st charge reaction, the valence was invariant, i.e., Mn did not contribute to the charge compensation [9,11,15]. During the discharge process, Mn valence did not change and not contribute to the charge compensation [9,15]. The Ru *K*-edge XANES spectra of $Li_{1.2}Ni_{0.13}Co_{0.13}Ru_{0.54}O_2$ cathode are shown in Figure 4-5 (c) and (d). Compared with the RuO_2 spectrum, the valence of Ru was tetravalent before charge reaction. During the charge process, the Ru *K*-edge XANES spectra gradually shifted to the higher energy, that is, oxidized to hexavalent after charge reaction [28]. In the discharge process, Ru was reduced to tetravalent, i.e., the reversible redox reaction occurs in the 1st charge/discharge reaction ($Ru^{4+} \leftrightarrow Ru^{5+}$). The results suggests that during the 1st charge-discharge reaction, charge was compensated by the Ru redox reaction.

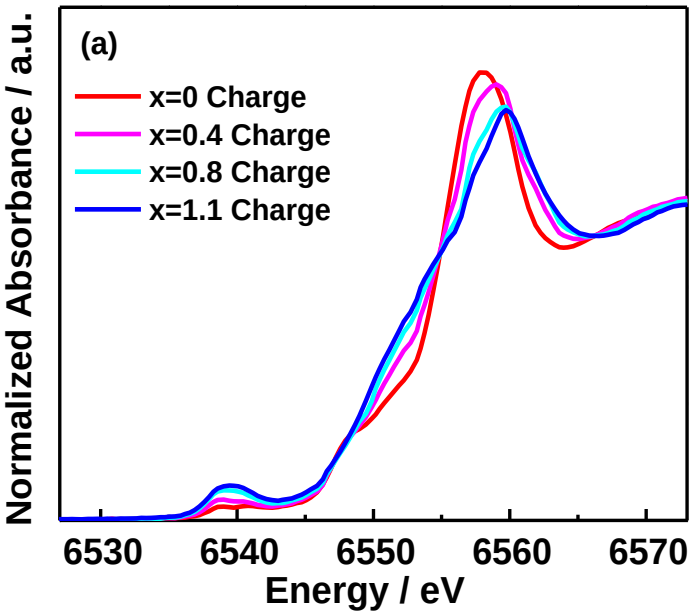

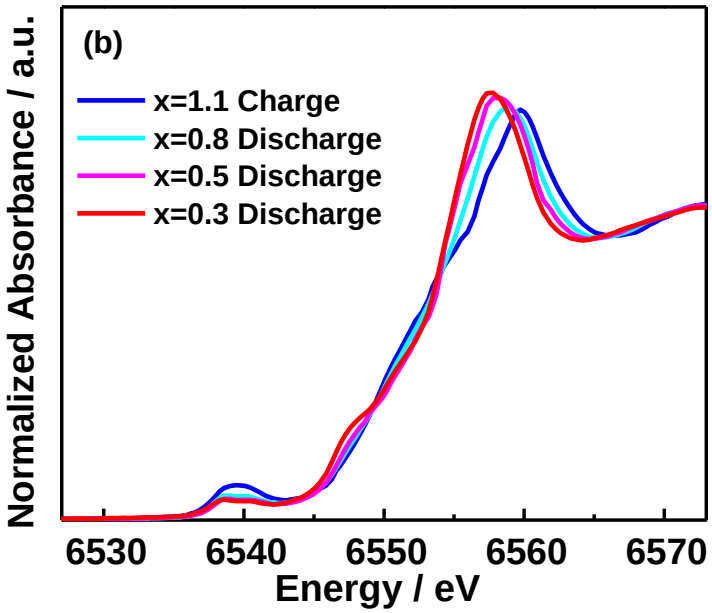
(b)
x=1.1 Charge
x=0.8 Discharge
x=0.5 Discharge
x=0.3 Discharge
Normalized Absorbance / a.u.
6530
6540
6550
6560
6570
Energy / eV

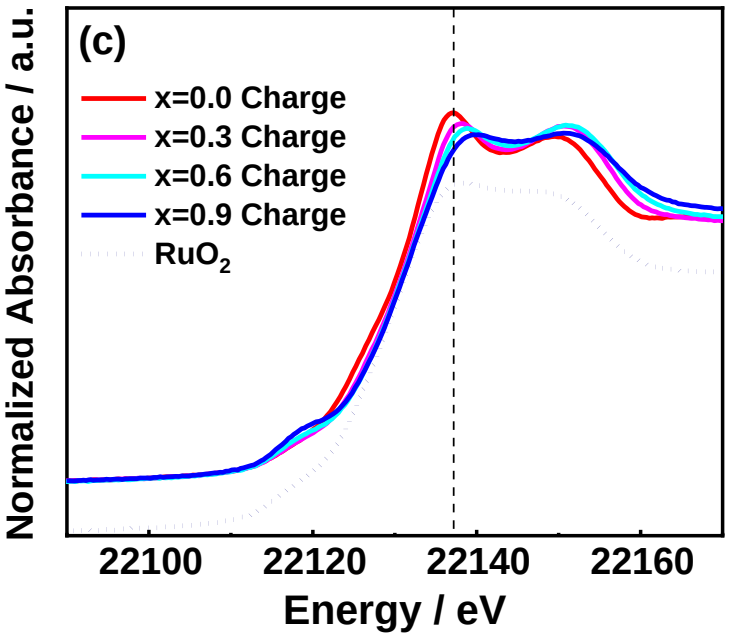
(c)
x=0.0 Charge
x=0.3 Charge
x=0.6 Charge
x=0.9 Charge
RuO2
Normalized Absorbance / a.u.
22100
22120
22140
22160
Energy / eV

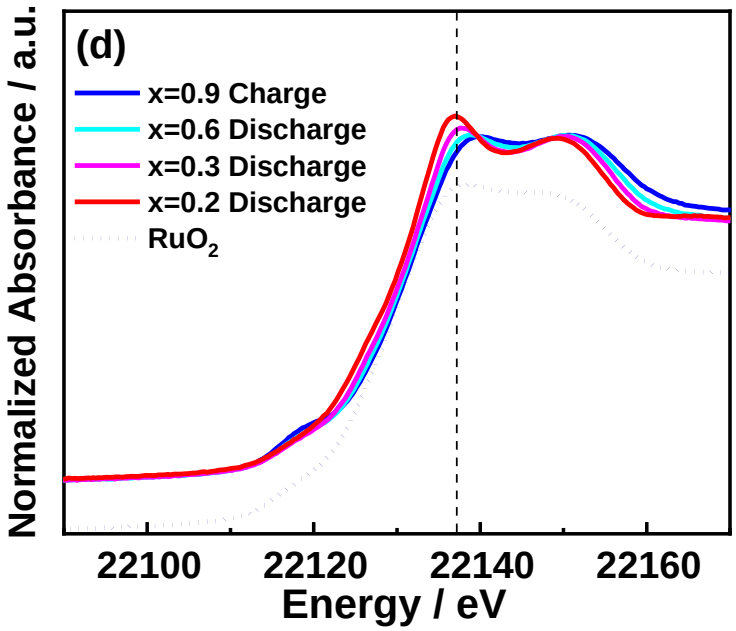

Figure 4-5: (a)-(b) X-ray absorption near edge structures for Mn *K*-edge of $Li_{1.2-x}Ni_{0.13}Co_{0.13}Mn_{0.54}O_2$ cathode, (a) 1st charge process (b) 1st discharge process. (c)-(d) X-ray absorption near edge structures for Ru *K*-edge of $Li_{1.2-x}Ni_{0.13}Co_{0.13}Ru_{0.54}O_2$ cathode, (c) 1st charge process (d) 1st discharge process.

Figure 4-6 (a) shows O *K* pre-edge XANES of the $Li_{1.2}Ni_{0.13}Co_{0.13}Mn_{0.54}O_2$ cathode during the 1st charge reaction. The O *K* pre-edge peak consists of two peaks at 529 eV and 531 eV, which are attributed to the transitions from the O 1*s* level to the hybridized states of the Mn 3*d* and O 2*p* orbitals [30,31]. In the former state of charge process, the top energy of the peak at 529 eV was shifted to the lower side by the oxidization of Ni and Co ions [30]. In the latter state of charge process, an additional peak at 530 eV appeared. This peak is attributed to the formation of peroxide states in charged states [31]. In case of the $Li_{1.2}Ni_{0.13}Co_{0.13}Ru_{0.54}O_2$ cathode, O *K* pre-edge XANES also consists of two peaks at 529 eV and 531 eV, which attributed to the transitions from the O 1*s* level to the hybridized states of the Ru 4*d* and O 2*p* orbitals [28,32,33]. The top energy of the peak at 529 eV was shifted to the lower side by the oxidization of Ru, Ni and Co ions [30]. However, an additional peak as seen in $Li_{1.2}Ni_{0.13}Co_{0.13}Mn_{0.54}O_2$ near 530 eV was not observed during the 1st charge reaction,

indicating that the peroxide states were not formed (Figure. 4-6 (b)). The band structure model of both cathodes were shown in Figure 4-6 (c). In case of $Li_{1.2}Ni_{0.13}Co_{0.13}Mn_{0.54}O_2$, 3*d* transition metals Ni^{2+} and Co^{3+} were near the Fermi level at pristine state because Ni^{2+} and Co^{3+} were oxidized to tetravalent at first, based on the Ni and Co *K*-edge XANES results and then, oxygen oxidization occurred ,which leaded to the formation of peroxide species. These results are consistent with the reported band model [12]. While in the case of $Li_{1.2}Ni_{0.13}Co_{0.13}Ru_{0.54}O_2$ cathode, Ru^{4+}, Ni^{2+} and Co^{3+} were oxidized to Ru^{5+}, Ni^{4+} and Co^{4+} during charge reaction based on Ru, Ni and Co *K*-edge XANES results. The peroxide species were not formed and oxygen contributed little to charge compensation during the 1st charge reaction because the energy level of O-2*p* orbital is lower than those of transition metals as shown in Figure 4-6 (c). The contribution of the oxygen to the redox band is lower than that of the 4*d* transition metal as reported [27]. The result indicates the charge compensation of $Li_{1.2}Ni_{0.13}Co_{0.13}Ru_{0.54}O_2$ cathode was introduced by the transition metal redox reaction, and the contribution of oxygen redox reaction was almost nonexistent.

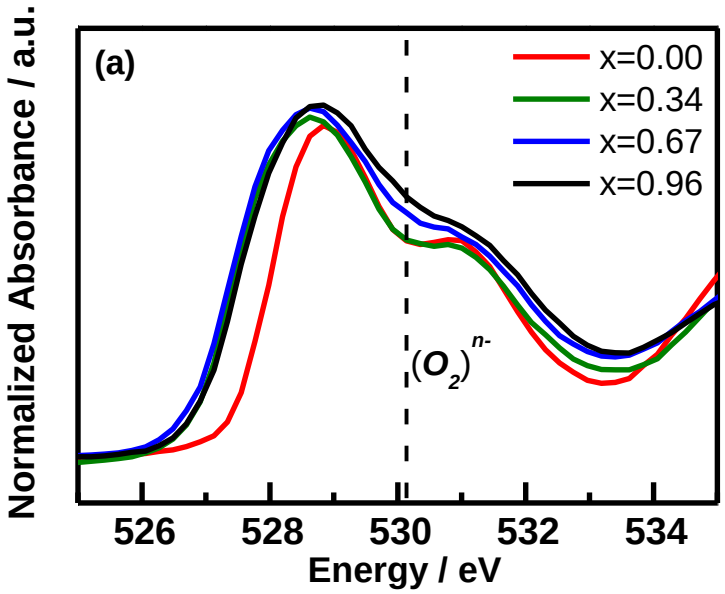

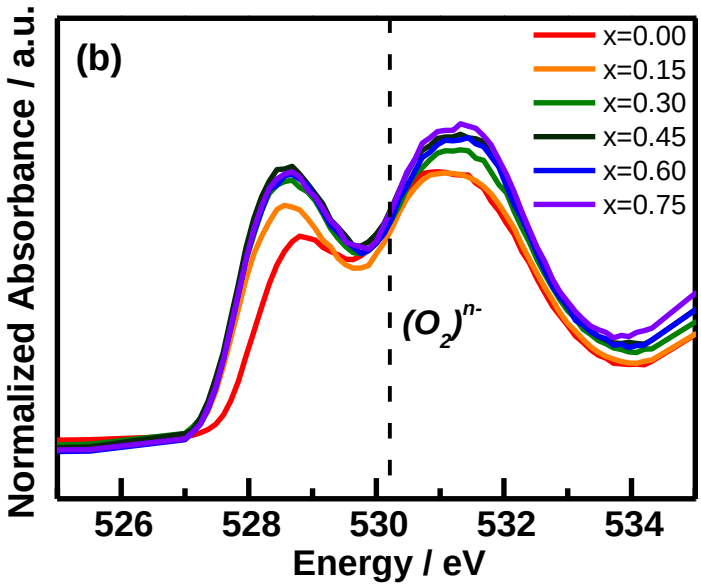

(c)

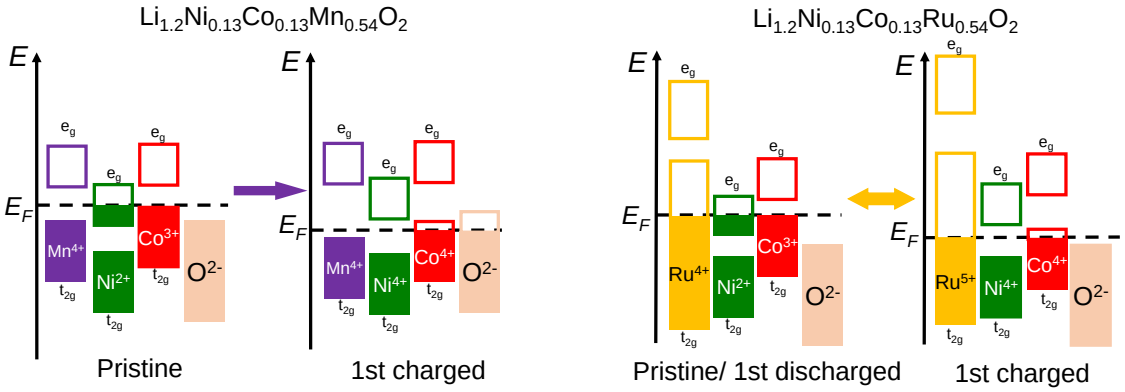

Figure 4-6. O *K* pre-edge XANES spectra for (a) $Li_{1.2-x}Ni_{0.13}Co_{0.13}Mn_{0.54}O_2$ cathode and (b) $Li_{1.2-x}Ni_{0.13}Co_{0.13}Ru_{0.54}O_2$ cathode during the 1st charge process. (c) Charge compensation mechanism of $Li_{1.2}Ni_{0.13}Co_{0.13}Mn_{0.54}O_2$ cathode and $Li_{1.2}Ni_{0.13}Co_{0.13}Ru_{0.54}O_2$ cathode.

Local structures of the $Li_{1.2}Ni_{0.13}Co_{0.13}Mn_{0.54}O_2$ cathode and $Li_{1.2}Ni_{0.13}Co_{0.13}Ru_{0.54}O_2$ cathode were analyzed by the Fourier transformation of the Mn, Ru, Ni and Co *K*-edge extended X-ray absorption fine structure (EXAFS) spectra. Figure 4-7 (a) and (c) show the change of the atomic distance and Debye-Waller factor

(DW factor) of Me-O (Me = Mn, Ni and Co) in $Li_{1.2}Ni_{0.13}Co_{0.13}Mn_{0.54}O_2$ cathode. The DW factor means a local distortion of Me-O.

The Mn-O distances were almost constant during the 1st charge and discharge process as shown in Figure 4-7 (a), because the valence of Mn was not changed from tetravalent. In the charge process, the Ni-O distances were decreased in the region x = 0 - 0.4 because of oxidation of Ni ions and almost constant in the region x = 0.4 - 1.1. In the discharge process, the Ni-O distances were increased in the region x = 1.1 - 0.5 because of reduction of Ni ions and almost constant in the region x = 0.5 - 0.3. The Co-O distances were decreased from x = 0 - 0.4 in the charge process because of oxidation of Co ions and almost constant in the region x = 0.4 - 1.1. In the discharge process, Co-O distances were almost constant in the region x = 1.1 - 0.8 and increased from x = 0.8 - 0.3 with reduction of Co ions. These results followed the valence changes as shown in Figure 4-4 and Figure 4-5.

Mn-O DW factors increased during the charge process (from x = 0 to x = 1.1) and decreased during the discharge process (from x = 1.1 to x = 0.3) even though the valence of Mn did not change during the charge and discharge process. The DW factor increasing is attributed to redox of oxygen, which increases the strain in the charged state. The oxygen hole formation occurred around the Mn atom because of Mn ionic character [11,28]. Ni-O DW factors increased during the charge process from x = 0.4 to x = 1.1 and decreased during the discharge process from x = 0.8 to x = 0.3. Co-O DW factors also increased during the charge process (from x = 0 to x = 1.1) and decreased during the charge process (from x = 0.8 to x = 0.3).

Figure 4-7 (b) show the change of the atomic distance of Me-O (Me = Ru, Ni and Co) in $Li_{1.2}Ni_{0.13}Co_{0.13}Ru_{0.54}O_2$ cathode. In the charge process, the Ru-O distances decreased in the region x = 0 - 0.9 because of oxidation of Ru ions. In the discharge process, the Ru-O distances increased in the region x = 0.9 - 0.2 because of reduction of Ru ions. The Ni-O distances decreased in the region x = 0 - 0.6 with oxidation of Ni ions in the charge process and almost constant in the region x = 0.6 - 0.9. In the discharge process, the Ni-O distances increased in the region x = 0.9 - 0.2 with reduction of Ni ions. The Co-O distances decreased from x = 0 - 0.9 in the charge process. In the charge process, the Co-O distances increased from x = 0.9 - 0.2 with

reduction of Co ions. The tendency of the distance changes of Ru-O, Ni-O and Co-O are coincided with the valence changes in charge and discharge process as shown in Figure 4-4 and Figure 4-5. The changes of Ni-O and Co-O distance are more steep in $Li_{1.2}Ni_{0.13}Co_{0.13}Mn_{0.54}O_2$ cathode than those of $Li_{1.2}Ni_{0.13}Co_{0.13}Ru_{0.54}O_2$ cathode because of the hysteresis of valence changes (see Figure 4-4).

Figure 4-7 (d) shows the DW factor of Ru-O, Ni-O and Co-O in $Li_{1.2}Ni_{0.13}Co_{0.13}Ru_{0.54}O_2$ cathode. Ru-O DW factors increased during the charge process and decreased during the discharge process. Ni-O DW factors are increased during the charge process (from x = 0 to x = 0.9) and decreased during the discharge process (from x = 0.9 to x = 0.2). There was little change of Co-O DW factor in $Li_{1.2}Ni_{0.13}Co_{0.13}Ru_{0.54}O_2$ cathode with different x values during the 1st charge and discharge process. The main difference of the result is the Ru-O DW factor of $Li_{1.2}Ni_{0.13}Co_{0.13}Ru_{0.54}O_2$ cathode were smaller compared with the Mn-O DW factor of $Li_{1.2}Ni_{0.13}Co_{0.13}Mn_{0.54}O_2$ cathode. These results suggested that the $Li_{1.2}Ni_{0.13}Co_{0.13}Ru_{0.54}O_2$ cathode had less distorted local structure than the $Li_{1.2}Ni_{0.13}Co_{0.13}Mn_{0.54}O_2$ cathode, which had more stable local structure.

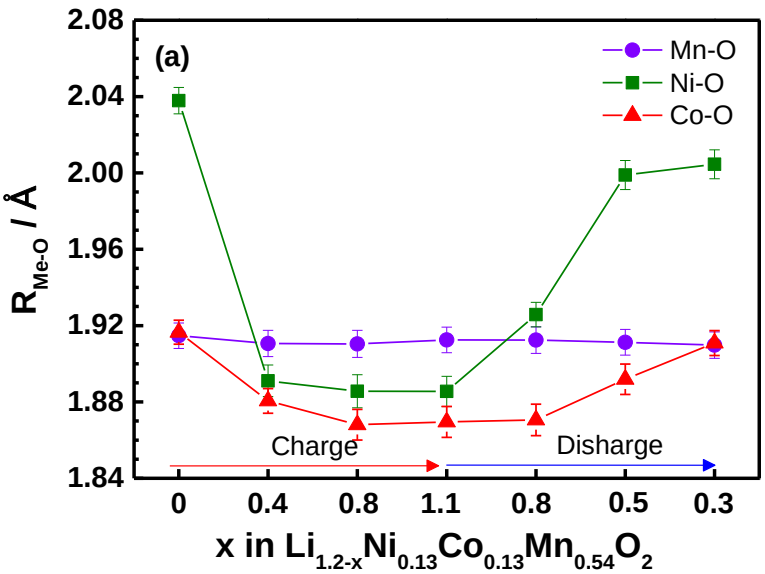

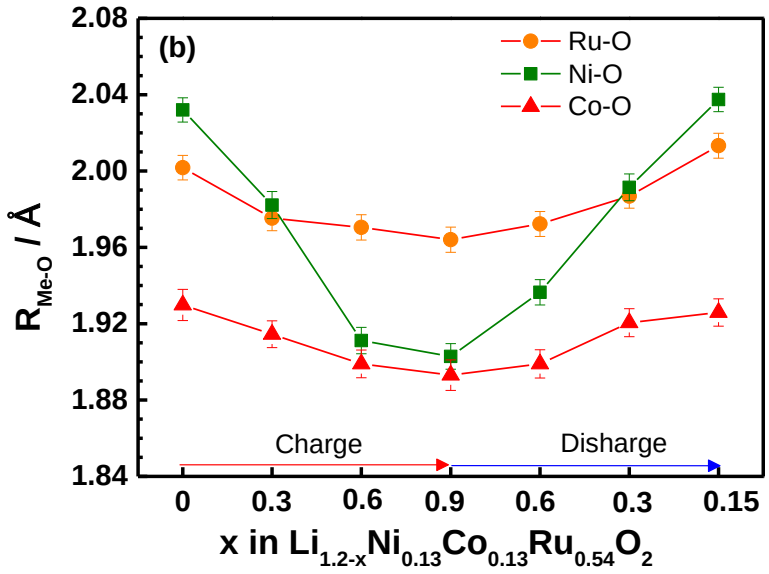
(b)
Ru-O
Ni-O
Co-O
R_{Me-O} / Å
2.08
2.04
2.00
1.96
1.92
1.88
1.84
Charge
Disharge
0
0.3
0.6
0.9
0.6
0.3
0.15
x in $Li_{1.2-x}Ni_{0.13}Co_{0.13}Ru_{0.54}O_2$

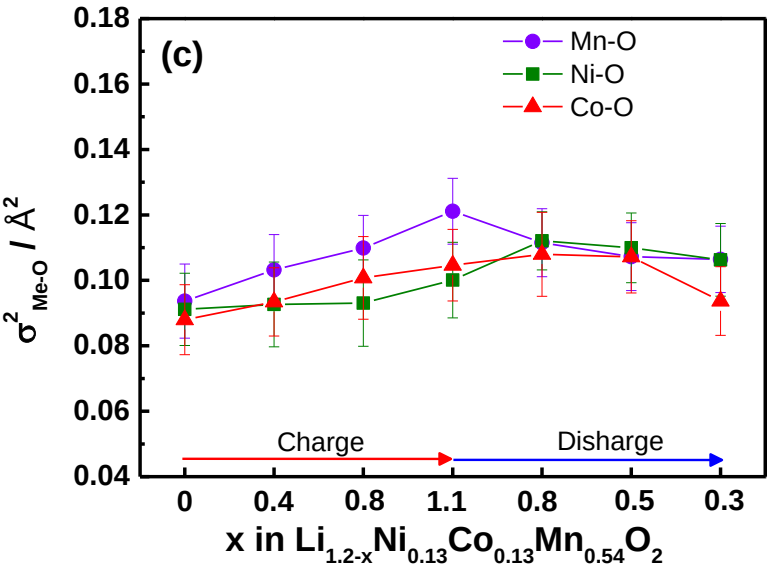
(c)
Mn-O
Ni-O
Co-O
σ^2_{Me-O} / Å^2
0.18
0.16
0.14
0.12
0.10
0.08
0.06
0.04
Charge
Disharge
0
0.4
0.8
1.1
0.8
0.5
0.3
x in $Li_{1.2-x}Ni_{0.13}Co_{0.13}Mn_{0.54}O_2$

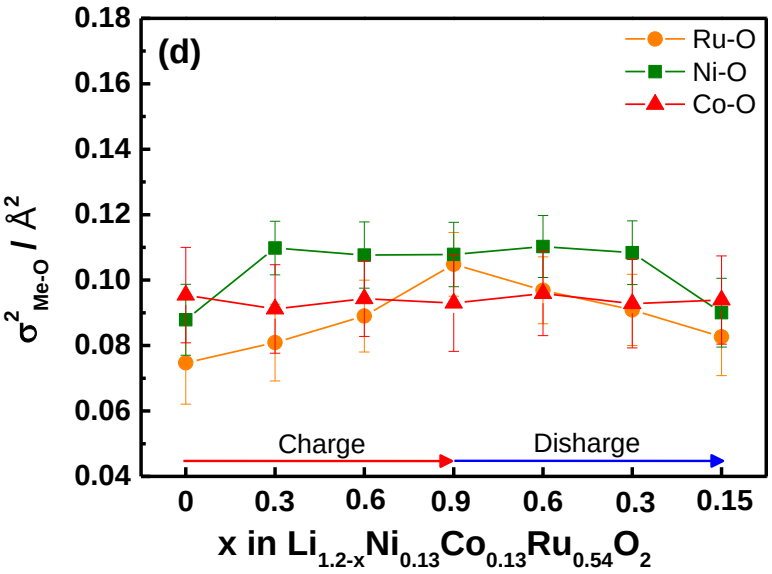

Figure 4-7. The atomic distance of (a) Mn-O, Ni-O and Co-O of $Li_{1.2}Ni_{0.13}Co_{0.13}Mn_{0.54}O_2$ cathode, (b) Ru-O, Ni-O and Co-O of $Li_{1.2}Ni_{0.13}Co_{0.13}Mn_{0.54}O_2$ cathode, and the Debye-Waller factors of (c) Mn-O, Ni-O and Co-O of $Li_{1.2}Ni_{0.13}Co_{0.13}Mn_{0.54}O_2$ cathode, (d) Ru-O, Ni-O and Co-O of $Li_{1.2}Ni_{0.13}Co_{0.13}Mn_{0.54}O_2$ cathode. Fourier transformed Mn, Ru, Ni and Co *K*-edge EXAFS spectra of $Li_{1.2}Ni_{0.13}Co_{0.13}Mn_{0.54}O_2$ cathode and $Li_{1.2}Ni_{0.13}Co_{0.13}Ru_{0.54}O_2$ cathode during the 1st charge-discharge reaction. These parameters were obtained by curve fitting with FEFF [34].

The charge compensation mechanism and local structure changes during the 1st charge-discharge process were different for $Li_{1.2}Ni_{0.13}Co_{0.13}Mn_{0.54}O_2$ and $Li_{1.2}Ni_{0.13}Co_{0.13}Ru_{0.54}O_2$. The choice of transition metals, which accept electrons from oxide ions on charge, is an essential key to determine whether to stabilize oxidation of oxide ions. In case of $Li_{1.2}Ni_{0.13}Co_{0.13}Mn_{0.54}O_2$, 3*d* transition metals Ni^{2+} and Co^{3+} were near the Fermi level at pristine state because Ni^{2+} and Co^{3+} were oxidized to tetravalent at first, based on the Ni and Co *K*-edge XANES results. In the middle of charge reaction, oxygen oxidization occurred and it leaded to the formation of peroxide species (as shown in Figure 4-6). Localized electron holes are formed on the O ions coordinated by Mn^{4+} because the Mn-O interactions are more ionic (less covalent) than Ni-O and Co-O

interactions [11]. Finally, oxygen evolution that is equivalent to oxygen loss from lattice [10]. On the other hand, in the case of $Li_{1.2}Ni_{0.13}Co_{0.13}Ru_{0.54}O_2$ cathode, Ru^{4+}, Ni^{2+} and Co^{3+}, were near the Fermi level at the pristine state, because Ru^{4+}, Ni^{2+} and Co^{3+} were oxidized to Ru^{5+}, Ni^{4+} and Co^{4+} during charge reaction based on Ru, Ni and Co *K*-edge XANES results. The peroxide species were not formed and oxygen contributed little to charge compensation during the 1st charge reaction (Figure 4-6 (b)).This result suggests that the energy level of O-2*p* orbital is lower than those of transition metals as shown in Figure 4-6 (c). In the discharge process, Ru^{5+}, Ni^{4+} and Co^{4+} were reduced to Ru^{4+}, Ni^{2+} and Co^{3+}, then the 1st discharged state was almost same state to pristine.

While the charge compensation of $Li_{1.2}Ni_{0.13}Co_{0.13}Mn_{0.54}O_2$ is explained by the redox reaction of transition metals (Ni, Co) and oxygen, the charge compensation mechanism of $Li_{1.2}Ni_{0.13}Co_{0.13}Ru_{0.54}O_2$ cathode is explained by the transition metals redox reaction and there is no compensation of oxygen redox as mentioned above. Figure 4-8 shows the difference of local structures on $Li_{1.2}Ni_{0.13}Co_{0.13}Mn_{0.54}O_2$ and $Li_{1.2}Ni_{0.13}Co_{0.13}Ru_{0.54}O_2$. In case of $Li_{1.2}Ni_{0.13}Co_{0.13}Mn_{0.54}O_2$, localized electron holes are formed on the O ions coordinated by Mn because of Mn high ionic character causing local distortion around Mn ions (Fig. 4-7 (c)). As a result, the strain around Ru is smaller than the strain around Mn. On the other hand, localized electron holes are not formed on the O ions coordinated by Ru in $Li_{1.2}Ni_{0.13}Co_{0.13}Ru_{0.54}O_2$, because of Ru high covalent character. Transition metal redox reaction is more kinetic than the oxygen reaction (the hole formation on O-2*p* orbital and/or oxygen evolution) [35]. Without an anion redox reaction and smaller local strains are considered to have led to an improvement in $Li_{1.2}Ni_{0.13}Co_{0.13}Ru_{0.54}O_2$ performance.

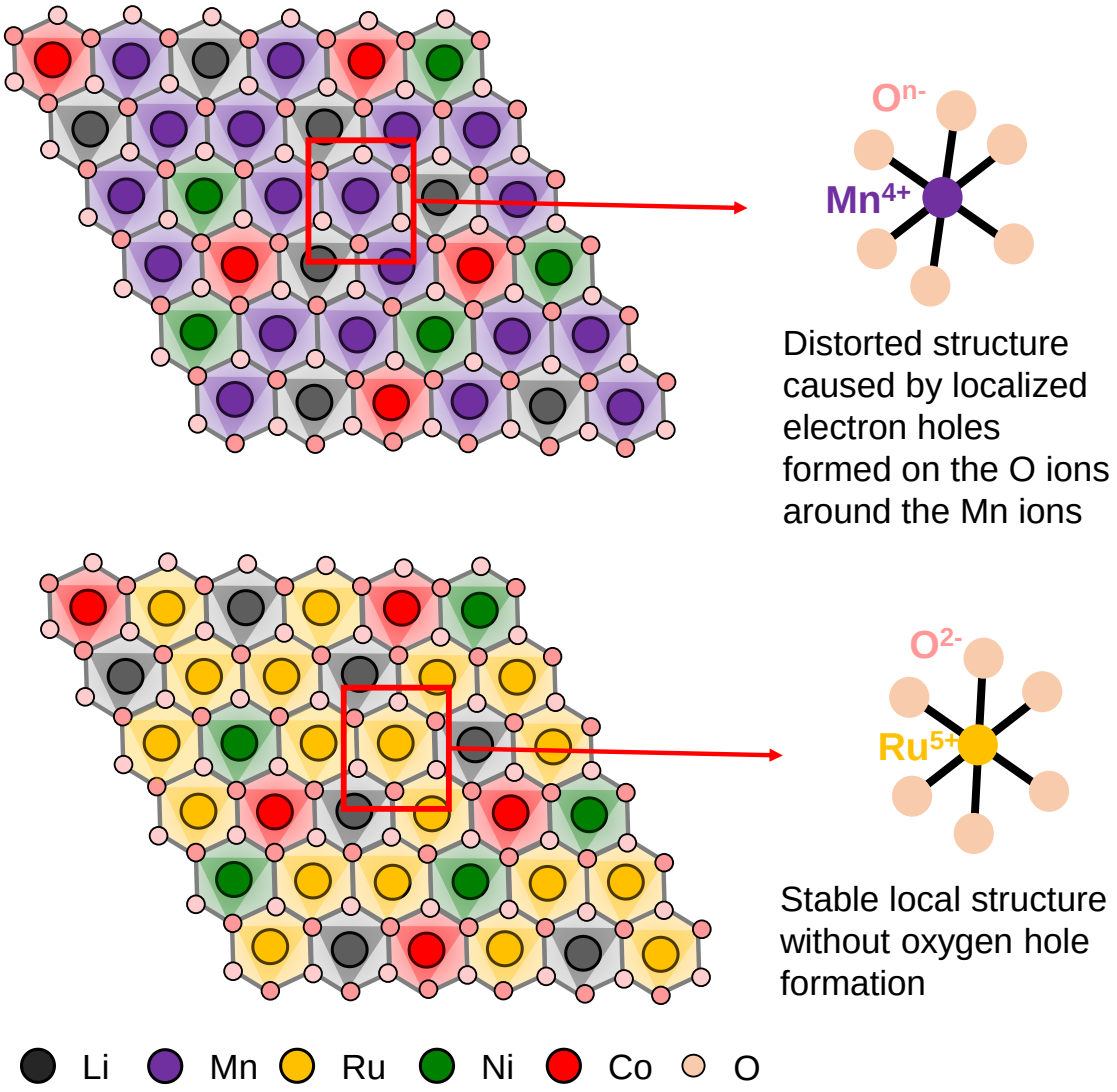

Figure 4-8. Difference of local structures on $Li_{1.2}Ni_{0.13}Co_{0.13}Mn_{0.54}O_2$ and $Li_{1.2}Ni_{0.13}Co_{0.13}Ru_{0.54}O_2$.

4-4. Conclusion

We synthesized two Li-rich solid solution cathodes $Li_{1.2}Ni_{0.13}Co_{0.13}Mn_{0.54}O_2$ and $Li_{1.2}Ni_{0.13}Co_{0.13}Ru_{0.54}O_2$, and then investigated their charge compensation mechanism by *operando* X-ray spectroscopy. The $Li_{1.2}Ni_{0.13}Co_{0.13}Ru_{0.54}O_2$ cathode material indicated high rate performance and good reversibility compared to $Li_{1.2}Ni_{0.13}Co_{0.13}Mn_{0.54}O_2$ cathode which was attributed to the reversible charge compensation of Ru, Ni, and Co with strong overlap feature between Ru-4*d* and O-2*p* orbitals and smaller hysteresis of valence changes. $Li_{1.2}Ni_{0.13}Co_{0.13}Ru_{0.54}O_2$ cathode also

had the less distorted structure, which takes advantage for Li diffusion, then it showed the higher rate performance than $Li_{1.2}Ni_{0.13}Co_{0.13}Mn_{0.54}O_2$ cathode. The result of O *K* pre-edge XANES suggested that the formation of localized hole on O-2*p* orbital was restrained which could offer the advantage of stability and rate performance during the 1st charge-discharge reaction. To design the next generation solid solution cathode materials, the strong overlap with O-2*p* orbital could be the key to stabilize the structure and improve the rate performance.

4-5. References

[1] B. Dunn, H. Kamath and J-M. Tarascon, “Electrical energy storage for the grid: a battery of choices.” *Science.* **334**, 928-935, (2011).

[2] M. S. Whittingham, “Materials challenges facing electrical energy storage.” *MRS Bull.* **33**, 411-419, (2008).

[3] M. Armand and J-M. Tarascon, “Building better batteries.” *Nature.* **451**, 652-657 (2008).

[4] T. Ohzuku and Y. Makimura, “Layered Lithium Insertion Material of $LiCo_{1/3}Ni_{1/3}Mn_{1/3}O_2$ for Lithium-Ion Batteries” *Chem. Lett.* **30**, 642-643, (2001).

[5] N. Yabuuchi and T. Ohzuku, “Novel lithium insertion material of $LiCo_{1/3}Ni_{1/3}Mn_{1/3}O_2$ for advanced lithium-ion batteries.” *J. Power Sources.* **119-121**, 171-174, (2003).

[6] K. Mizushima, P. C.Jones, P. J.Wiseman, and J. B. Goodenough, “LI_XCOO_2 ($0<x\leq1$)—a new cathode material for batteries of high-energy density.” *Mater. Res. Bull.* **15**, 783-789, (1980).

[7] Z. Lu and J.R. Dahn, “Understanding the Anomalous Capacity of $Li/Li[Ni_xLi_{(1/3-2x/3)}Mn_{(2/3-x/3)}]O_2$ Cells Using In Situ X-Ray Diffraction and Electrochemical Studies.” *J. Electrochem. Soc.* **149**, A815-A822, (2002).

[8] M.M. Thackeray, S.H. Kang, C.S. Johnson, J.T. Vaughey, R. Benedek, S.A. Hackney, “Li_2MnO_3-stabilized $LiMO_2$ (M = Mn, Ni, Co) electrodes for lithium-ion batteries.” *J. Mater. Chem.* **17**, 3112-3125, (2007).

[9] M. Oishi, T. Fujimoto, Y. Takanashi, Y. Orikasa, A. Kawamura, T. Ina, H. Yamashige, D. Takamasu, K. Sato, H. Murayama, H. Tanida, H. Arai, H. Ishii, C. Yogi, I. Watanabe, T. Ohta, A. Mineshige, Y. Uchimoto and Z. Ogumi, “Charge compensation mechanisms in $Li_{1.16}Ni_{0.15}Co_{0.19}Mn_{0.50}O_2$ positive electrode material for Li-ion batteries analyzed by a combination of hard and soft X-ray absorption near edge structure.” *J. Power Sources.* **222**, 45-51, (2013).

[10] A.R. Armstrong, M. Holzapfel, P. Novak, C.S. Johnson, S.H. Kang,M.M. Thackeray and P.G. Bruce, “Demonstrating Oxygen Loss and Associated Structural Reorganization in the Lithium Battery Cathode $Li[Ni_{0.2}Li_{0.2}Mn_{0.6}]O_2$.” *J. Am. Chem. Soc.* **128**, 8694-8698, (2006).

[11] K. Luo, M. R. Roberts, R. Hao, N. Guerrini, D. M. Pickup, Y-S. Liu, K. Edstrom, J. Guo, A. V. Chadwick, L. C. Duda and P. G. Bruce, "Charge-compensation in 3d-transition-metal-oxide intercalation cathodes through the generation of localized electron holes on oxygen." *Nat. Chem.* **8**, 684-691, (2016).

[12] D. H. Seo, J. Lee, A. Urban, R. Malik, S. Y. Kang and G. Ceder, "The structural and chemical origin of the oxygen redox activity in layered and cation-disordered Li-excess cathode materials." *Nat. Chem.* **8**, 692-697, (2016).

[13] N. Yabuuchi, K. Yoshii, S-T. Myung, I. Nakai, and S. Komaba, "Detailed Studies of a High-Capacity Electrode Material for Rechargeable Batteries, Li_2MnO_3-$LiCo_{1/3}Ni_{1/3}Mn_{1/3}O_2$." *J. Am. Chem. Soc.* **133**, 4404-4419, (2011).

[14] G. Assat, C. Delacourt, D. A. Dalla Corte and J-M. Tarascon, "Practical Assessment of Anionic Redox in Li-Rich Layered Oxide Cathodes: A Mixed Blessing for High Energy Li-Ion Batteries." *J. Electrochem. Soc.* **163**, A2965-A2976 (2016).

[15] M. Oishi, C. Yogi, I. Watanabe, T. Ohta, Y. Orikasa, Y. Uchimoto and Z. Ogumi, "Direct observation of reversible charge compensation by oxygen ion in Li-rich manganese layered oxide positive electrode material, $Li_{1.16}Ni_{0.15}Co_{0.19}Mn_{0.50}O_2$." *J. Power Sources.* **276**, 89-94, (2015).

[16] T. Ohzuku, M. Nagayama, K. Tsuji and K. Ariyoshi, "High-capacity lithium insertion materials of lithium nickel manganese oxides for advanced lithium-ion batteries: toward rechargeable capacity more than 300 mA h g^{-1}." *J. Mater. Chem.* **21**, 10179-10188, (2011).

[17] H. Koga, L. Croguennec, M. Menetrier, K. Douhil, S. Belin, L. Bourgeois, E. Suard, F. Weill and C. Delmas, "Reversible oxygen participation to the redox processes revealed for $Li_{1.20}Mn_{0.54}Co_{0.13}Ni_{0.13}O_2$." *J. Electrochem. Soc.* **160**, A786-A792, (2013).

[18] N. Yabuuchi, K. Yoshii, S-T. Myung, I. Nakai, and S. Komaba, "Detailed Studies of a High-Capacity Electrode Material for Rechargeable Batteries, Li_2MnO_3−$LiCo_{1/3}Ni_{1/3}Mn_{1/3}O_2$." *J. Am. Chem. Soc.* **133**, 4404-4419, (2011).

[19] K. Luo, M.R. Roberts, R. Hao, N. Guerrini, D. M. Pickup, Y. S. Liu, K. Edstrom, J. H. Guo, A. V. Chadwick, L. C. Duda and P. G. Bruce, "Charge-compensation in

3d-transition-metaloxide intercalation cathodes through the generation of localized electron holes on oxygen." *Nat. Chem.* **8**, 684-691 (2016).

[20] J. Jiang, and J. R. Dahn, "Insignificant impact of designed oxygen release from high capacity $Li[(Ni_{1/2}Mn_{1/2})_xCo_y(Li_{1/3}Mn_{2/3})_{1/3}]O_2$ (x + y = 2/3) positive electrodes during the cycling of Li-ion cells." *Electrochim. Acta.* **51**, 3413-3416, (2006).

[21] Z. Li, F. Du, X. Bie, D. Zhang, Y. Cai, X. Cui, C. Wang, G. Chen and Y. Wei, "Electrochemical Kinetics of the $Li[Li_{0.23}Co_{0.3}Mn_{0.47}]O_2$ Cathode Material Studied by GITT and EIS." *J. Phys. Chem. C*. **114**, 22751-22757, (2010).

[22] E. McCalla, A. M. Abakumov, M. Saubanere, D. Foix, E. J Berg, G. Rousse, M-L.Doublet, D. Gonbeau, P. Novak, G. V.Tendello, R. Dominko and J-M. Tarascon, "Visualization of O-O peroxo-like dimers in high-capacity layered oxides for Li-ion batteries." *Scienc*e. **18**, 1516-1521, (2015).

[23] M. Sathiya, K. Ramesha, G. Rousse, D. Foix, D. Gonbeau, A. S. Prakash, M-L. Doublet, K. Hemalatha and J-M. Taracson, "High Performance $Li_2Ru_{1-y}Mn_yO_3$ ($0.2 \leq y \leq 0.8$) Cathode Materials for Rechargeable Lithium-Ion Batteries: Their Understanding." *Chem. Mater.* **25**, 1121-1131, (2013).

[24] M. Sathiya, G. Rousse, K. Ramesha, C. P. Laisa, H. Vezin, M. T. Sougrati, M-L. Doublet, D. Foix, D. Gonbeau, A. Walker, A. S. Prakash, M.B. Hassine, L. Dupont and J-M. Tarascon, "Reversible anionic redox chemistry in high-capacity layered-oxide electrodes." *Nat, Mater.* **12**, 827-835, (2013).

[25] M. Sathiya, A. M. Abakumov, D. Foix, G. Rousse, K. Ramesha, M. Saubanere, M-L. Doublet, H. Vezin, C. P. Laisa, A.S. Prakash, D. Gonbeau, G. VanTendeloo and J-M. Tarascon, "Origin of voltage decay in high-capacity layered oxide electrodes." *Nat. Mater*. **14**, 230-238, (2014).

[26] B. Li, R. Shao, H. Yan, L. An, B. Zhang, H. Wei, J. Ma, D. Xia and X. Han, "Understanding the Stability for Li-Rich Layered Oxide Li_2RuO_3 Cathode." *Adv. Funct. Mater.* **26**, 1330-1337, (2016).

[27] M. Saubanere, E. McCalla, J-M. Tarascon, and M-L. Doublet, "The intriguing question of anionic redox in high-energy density cathodes for Li-ion batteries." *Energy Environ. Sci.* **9**, 984-991, (2016).

[28] K. Yamamoto, Y. Zhou, N. Yabuuchi, K. Nakanishi, T. Yoshinari, T. Kobayashi, Y. Kobayashi, R. Yamamoto, A. Watanabe, Y. Orikasa, K. Tsuruta, J. Park, H. R. Byon, Y. Tamenori, T. Ohta and Y. Uchimoto, "Charge Compensation Mechanism of Lithium-excess Metal Oxides with Different Covalent and Ionic Characters revealed by *operando* Soft and Hard X-ray Absorption Spectroscopy." *Chem. Mater.*, in press.

[29] F.Amalraj, D. Kovacheva, M. Talianker, L. Zeiri, J. Grinblat, N. Leifer, G. Goobes, B. Markovsky and D. Aurbach, *J. Electrochem. Soc.*, **157**, (10) A1121-A1130, (2010)

[30] W. S. Yoon, M. Balasubramanian, K. Y. Chung, X. Q. Yang, J. McBreen; C. P. Grey, D. A. Fischer, "Investigation of the charge compensation mechanism on the electrochemically Li-Ion deintercalated $Li_{1-x}Co_{1/3}Ni_{1/3}Mn_{1/3}O_2$ electrode system by combination of soft and hard X-ray absorption spectroscopy." *J. Am. Chem. Soc.* **127**, 17479–17487, (2005).

[31] M.Oishi, K.Yamanaka, I. Watanabe, K.Shimoda, T. Matsunaga, H. Arai, Y. Ukyo, Y. Uchimoto, Z. Ogumi, T. Ohta, Direct observation of reversible oxygen anion redox reaction in Li- rich manganese oxide, Li2MnO3, studied by soft X-ray absorption spectroscopy. *J. Mater. Chem. A*, **4**, 9293−9302, (2016).

[32] Z. Hu, H. von Lips, M. S. Golden, J. Fink, G. Kaindl, F. M. F. de Groot, S. Ebbinghaus, A. Reller, Multiplet effects in the Ru $L_{2,3}$ X-ray-absorption spectra of Ru(IV) and Ru(V) compounds. *Phys. Rev. B: Condens. Matter Mater. Phys.* **61**, 5262−5266, (2000).

[33] J. G. Zhou, H. T. Fang, Y. F. Hu, T. K. Sham, C. X.Wu, M. Liu, F. Li, Immobilization of RuO_2 on carbon nanotube: An X-ray absorption near-edge structure study. *J. Phys. Chem. C*, **113**, 10747−10750, (2009).

[34] J.J. Rehr, R. C. Albers, Theoretical approaches to x-ray absorption fine structure. *Rev. Mod. Phys.* **72**, 621−654, (2000).

[35] P. Rozier and J-M. Tarascon, Review—Li-Rich Layered Oxide Cathodes for Next-Generation Li-Ion Batteries: Chances and Challenges. *J. Electrochem. Soc.*, **162** (14) A2490-A2499, (2015).

Chapter 5. Capacity Improvement by Nitrogen-doping to Lithium Rich Cathode Materials with Stabilization Effect of Oxide Ions Redox

5-1. Introduction

Lithium-ion batteries (LIBs) are widely used for electronic devices and desired to expand in larger-scale applications such as vehicles, public transportations or energy storage systems [1]. Capacity improvement is thus required for the commercialized LIBs, however, further increase in their energy density is severely restricted by the theoretical limits for cathodes [2]. Conventional cathode materials such as $LiCoO_2$, transition metals mainly contribute to the charge compensation during charge/discharge reactions, which restricts their theoretical capacity. On the other hand, lithium-rich materials such as Li_2MnO_3 based materials provide high theoretical capacity, compared to the conventional cathode materials, because the oxide ions as well as the transition metal contributes charge compensation during charge/discharge reactions [3-5]. However, oxidation of oxide ions often causes irreversible oxygen loss [6] accompanied by a phase transition [7] typically in Li_2MnO_3-systems. Stabilization of the oxide ions redox would be essential to design and develop new cathode materials with high energy density.

To stabilize the oxygen redox, various types of lithium rich cathode materials formed by the substitution of transition metals have been extensively studied [8-29]. Among these materials, Yabuuchi *et al*. reported that $Li_{1.2}Ti_{0.4}Mn_{0.4}O_2$ shows high capacity over 300 mAh g^{-1} and low 1st irreversible capacity [17,29]. The charge compensation mechanism of $Li_{1.2}Ti_{0.4}Mn_{0.4}O_2$ cathode is Mn oxidization and oxygen hole formation [17]. Our group revealed that high ionic character of Ti^{4+} stabilizes the localization of electrons on the oxide ions [29]. In order to achieve a high capacity, it is important to enhance electron localization on anion in the structure. The substitution of transition metal and the change of the composition ratio, which have been performed so far, lack the decisive factor at present.

Considering nitrogen ions can exist at lower valence than oxide ions, nitrogen doping could be an effective method to improve the capacity of the oxide ions redox reaction. However, the oxide ions redox mechanism of nitrogen-doped lithium rich cathodes still remains to be clarified because the lithium-rich cathodes in which oxygen release reaction occurs were used for the host material [30-32]. In order to clarify the effect of nitrogen doping for the anion redox, nitrogen doping must be conducted into the bulk of the lithium-rich cathodes in which oxygen release reaction does not occur such as $LiTi_{0.4}Mn_{0.4}O_2$ [27]. In this work, we conducted nitrogen doping into the bulk of $LiTi_{0.4}Mn_{0.4}O_2$ and examined the electrochemical property, electronic and local structures. Anionic substituted oxides, such as fluorine, nitrogen doping, have been reported [30-35]. Fluorine doping can decrease the valence of transition metals, improving the capacity of cationic redox. Nitrogen-doping into lithium rich cathode materials also have been reported[30-32]. The nitrogen-doping improves rate capabilities and suppresses the voltage fading of the lithium rich material electrodes because lithium diffusion is accelerated due to the existence of nitrogen in the surface layer [31]. The purpose of this research is to control the oxide ions redox in the $Li_{1.2}Ti_{0.4}Mn_{0.4}O_2$ by doping nitrogen into the bulk, which is different from previous nitrogen doping [30-32].

5-2. Experimental

Nitrogen-doped cathode materials $Li_{1.2}Ti_{0.4}Mn_{0.4}O_{2-0.015x}N_{0.01x}$ (x = 5, 10 … 40) based on the cation-disordered rocksalt-type cathode material $Li_{1.2}Ti_{0.4}Mn_{0.4}O_2$ [17] were synthesized by mechanochemical ball-milling method from stoichiometric amounts of lithium oxide, titanium oxide (anatase), manganese oxide (trivalent: 3+) and lithium nitride [36]. The pellets of mixed powders were heated at 900 °C for 1 hour (for x = 5, 10 … 40) or 12 hours (for x = 0). The chemical composition of the prepared $Li_{1.2}Ti_{0.4}Mn_{0.4}O_{2-0.015x}N_{0.01x}$ in the x-range from 0 to 30 was determined by Inductivity Coupled Plasma Optical Emission Spectrometer (ICP-OES). All obtained powders were characterized by synchrotron radiation (SR) X-ray powder diffraction (XRD) experiments at SPring-8 BL02B2.

Compound cathodes were prepared from the paste which was produced by mixing 70 wt% of as-prepared cathode materials (carbon-coated), 20 wt% of acetylene

black and 10 wt% of polyvinylidene difluoride binder in 1-methyl-2-pyrrolidone solvent, and then this paste was coated on the Al foil. We assembled the cell with cathodes, Li foil as the anode and 1 mol dm^{-3} $LiPF_6$ in an acetonitrile solvent was used as an electrolyte. The galvanostatic charge and discharge measurements were performed at the current rate, C/20. The cut-off voltage was between 1.5 V and 4.8 V (vs. Li/Li^+) and the constant-current charge and discharge measurements were operated at 50 °C.

Soft X-ray absorption spectroscopy (XAS) measurements for Ti *L*-edge, Mn *L*-edge and O *K*-edge were performed in SPring-8 BL27SU. Three electrodes ($Li_{1.2}Ti_{0.4}Mn_{0.4}O_2$, $Li_{1.2}Ti_{0.4}Mn_{0.4}O_{1.93}N_{0.05}$ and $Li_{1.2}Ti_{0.4}Mn_{0.4}O_{1.85}N_{0.10}$) were prepared for the ex-situ XAS measurement in the same condition of the galvanostatic charge-discharge measurements. After having finished the charge discharge measurements, the cells were dissembled in an argon-filled glove box. Then electrodes were flushed the electrolyte with the dimethyl carbonate three times and dried in the Ar atmosphere with vacuum. To prevent the electrode samples from being exposed to the air, they were transferred to a high-vacuum sample chamber by using a transfer vessel filled with Ar gas.

5-3. Results and discussion

Crystal structures of the prepared $Li_{1.2}Ti_{0.4}Mn_{0.4}O_{2-0.015x}N_{0.01x}$ were characterized by X-ray diffraction (XRD) as shown in Figure 5-1. The $Li_{1.2}Ti_{0.4}Mn_{0.4}O_{2-0.015x}N_{0.01x}$ in the range from x = 0 to x = 30 had the cation-disordered rocksalt structure which was classified to a single phase of the *Fm-3m* space group [17]. The diffraction shifted to lower angle with the amount of nitrogen as shown in the inset of Figure 5-1(a). In the range over x = 30, some additional peaks were observed as impurity. The lattice constant calculated from the XRD patterns increased in the range from x = 0 to x = 30, and remained constant in the range from x = 30 to x = 40 (Figure 5-1(b)). The lattice constant increase indicates that nitrogen doping into $Li_{1.2}Ti_{0.4}Mn_{0.4}O_2$ materials succeeded because the ionic radius of nitrogen ion (1.46 Å) is larger than oxide ion (1.40 Å) [37].

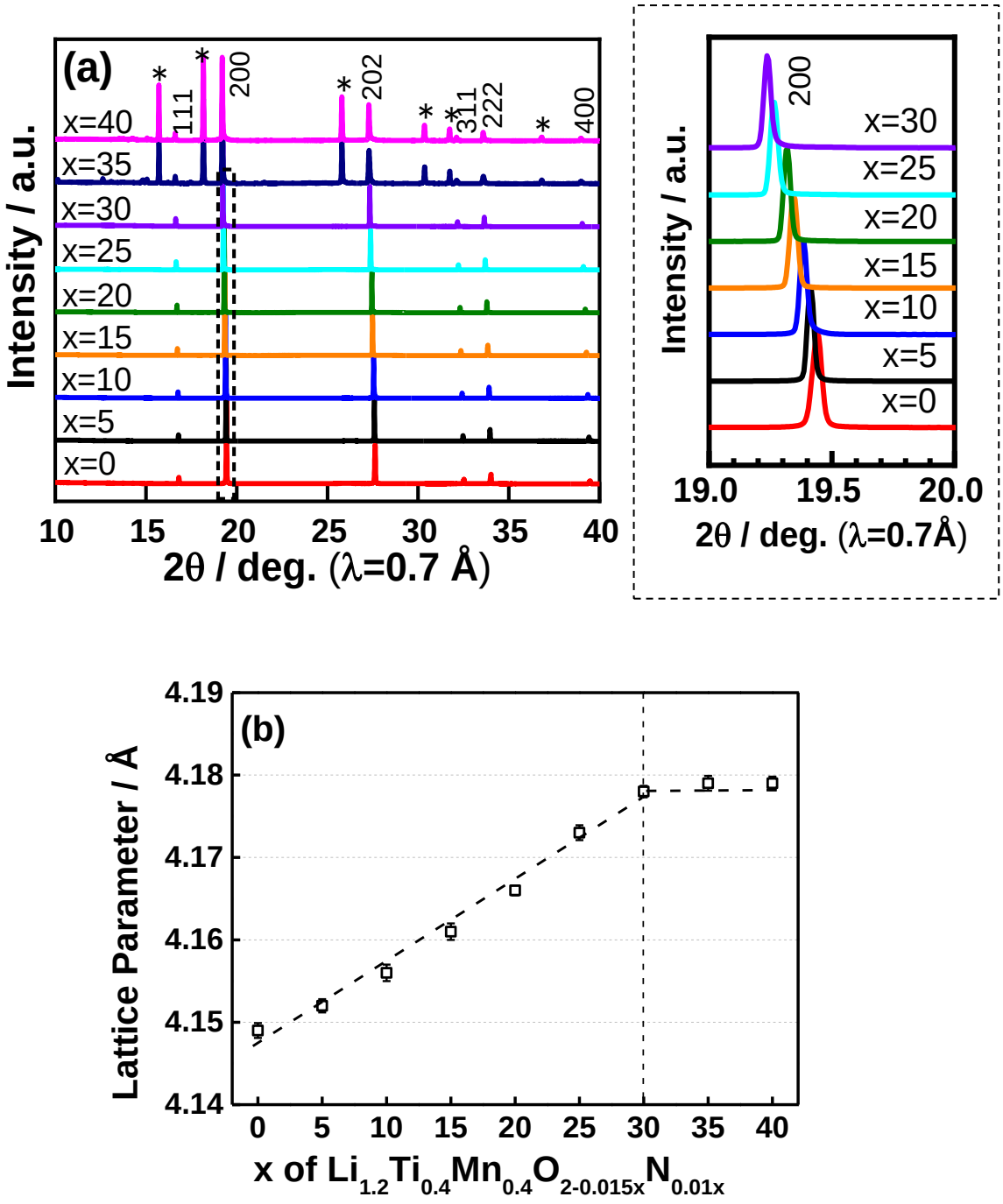

Figure 5-1. Synchrotron XRD spectra for $Li_{1.2}Ti_{0.4}Mn_{0.4}O_{2-0.015x}N_{0.01x}$. (a) XRD spectra indicating a single phase of *Fm-3m* space group with x = 0, 5, 10, ··· 40 with some impurities peaks in x = 35 and x = 40 data designated by asterisks. Inset shows enlarged spectra in the dotted frame ranging from 2θ = 19.0° to 20.0°. (b) Dependence of lattice parameters on the amount of nitrogen doping *x*.

The results of X-ray photoelectron spectroscopies were shown in Figure 5-2. Although a nitrogen peak was observed in x = 30, the peak was not observed in x = 0 and x = 10. These results indicate that the nitrogen doping occurs in the bulk of $Li_{1.2}Ti_{0.4}Mn_{0.4}O_2$, not to the surface. The chemical composition of each cathode was summarized in Table 5-1, characterized by inductivity coupled plasma optical emission spectrometer. The ratio of metals was constant from the molar ratio of starting materials regardless of the amount of the nitrogen doping (Li: Ti: Mn =1.2: 0.4: 0.4 with x = 0, 10, 20 and 30).

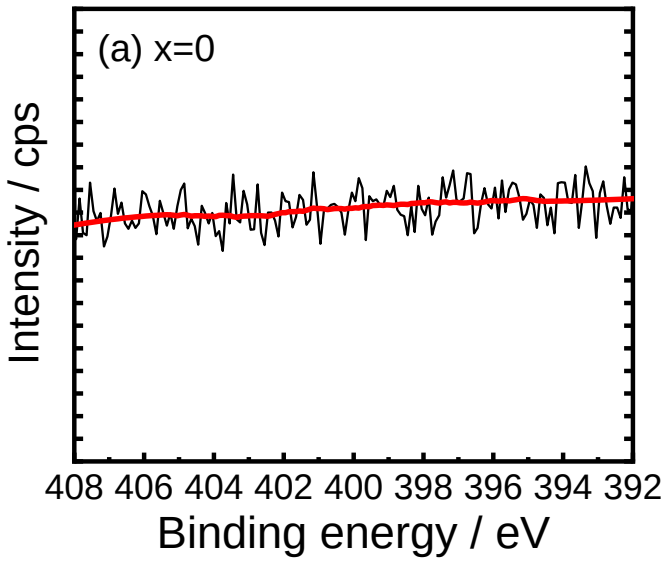

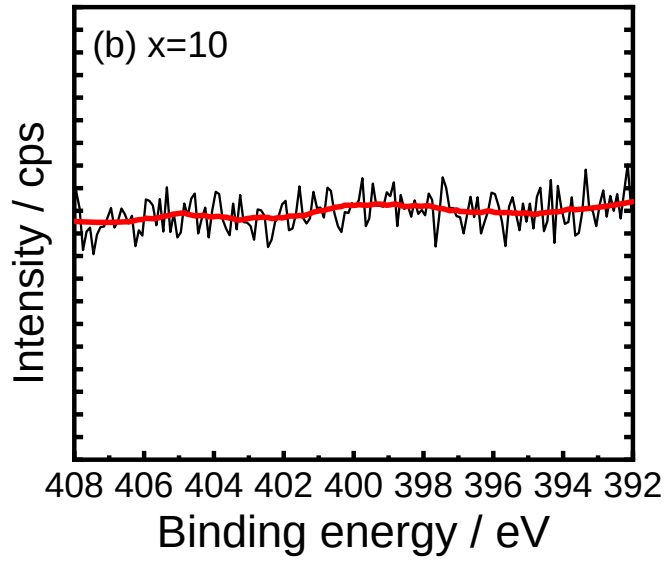

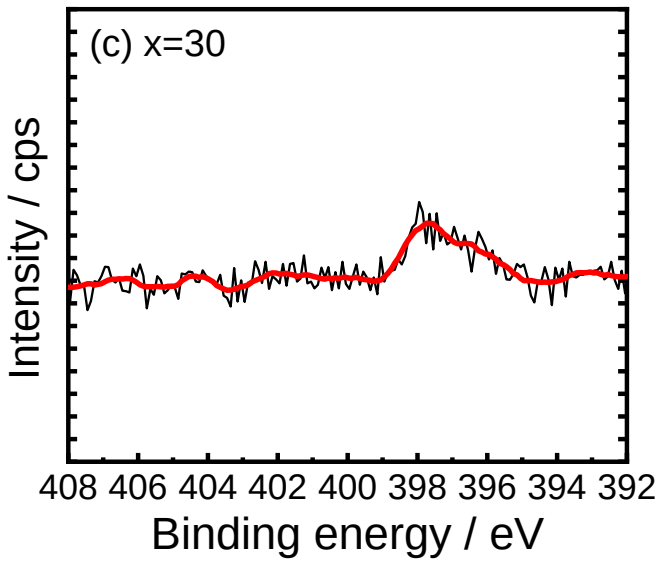

Figure 5-2. The results of XPS measurement of N 1s peak, (a) $Li_{1.2}Ti_{0.4}Mn_{0.4}O_2$ (b) $Li_{1.2}Ti_{0.4}Mn_{0.4}O_{1.85}N_{0.10}$ and (c) $Li_{1.2}Ti_{0.4}Mn_{0.4}O_{1.55}N_{0.30}$.

Table 5-1. The chemical composition of $Li_{1.2}Ti_{0.4}Mn_{0.4}O_{2-0.015x}N_{0.01x}$ cathode by ICP-OES.

Material	The molar ratio of Li : Ti : Mn
x = 0	1.2 : 0.398 : 0.400
x = 10	1.2 : 0.399 : 0.400
x = 20	1.2 : 0.401 : 0.401
x = 30	1.2 : 0.399 : 0.401

The electrochemical performance of the prepared $Li_{1.2}Ti_{0.4}Mn_{0.4}O_{2-0.015x}N_{0.01x}$ was measured by galvanostatic charge and discharge measurements at the C/20 rate (1C rate = 395 mA g^{-1}) at 50 °C as shown in Figure 5-3. The $Li_{1.2}Ti_{0.4}Mn_{0.4}O_2$ cathode showed similar charge/discharge curves as observed in previous report [17], which shows a long plateau attributed to oxygen redox at approximately 4.5 V (Figure 5-3 (a)). The 1st charge capacities in the low voltage region (3.0 – 4.2 V) and high voltage region (4.2 – 4.8 V) were 132 mAh g^{-1} and 166 mAh g^{-1}, respectively (Figure 5-3 (a) and (c)). Nitrogen doping in the range from x = 0 to x=10 improved the electrochemical

performance. The nitrogen-doped cathode with x = 10, $Li_{1.2}Ti_{0.4}Mn_{0.4}O_{1.85}N_{0.10}$, showed smaller polarization than $Li_{1.2}Ti_{0.4}Mn_{0.4}O_2$, and larger charge capacities in the 3.0-4.2 V region (153 mAh g^{-1}) as well as 4.2-4.8 V region (196 mAh g^{-1}) in the 1st charge process (Figure 5-3 (b) and (c)). The $Li_{1.2}Ti_{0.4}Mn_{0.4}O_{1.85}N_{0.10}$ also showed larger charge capacity (349 mAh g^{-1}) than the $Li_{1.2}Ti_{0.4}Mn_{0.4}O_2$ (299 mAh g^{-1}).

The 1st charge capacity of the $Li_{1.2}Ti_{0.4}Mn_{0.4}O_{2-0.015x}N_{0.01x}$ increased in the x range from x = 0 to x = 10. However, more amount of nitrogen doping (x ≥ 15) decreased 1st charge capacity as shown in Figure 5-3 (c). Although it is worth clarifying the reason the capacity decreasing by large amount of nitrogen doping, we focus on the reason the capacity increasing by small amount of nitrogen doping in this study. Therefore, the $Li_{1.2}Ti_{0.4}Mn_{0.4}O_2$ and $Li_{1.2}Ti_{0.4}Mn_{0.4}O_{1.85}N_{0.10}$ cathodes were chosen for detailed investigation.

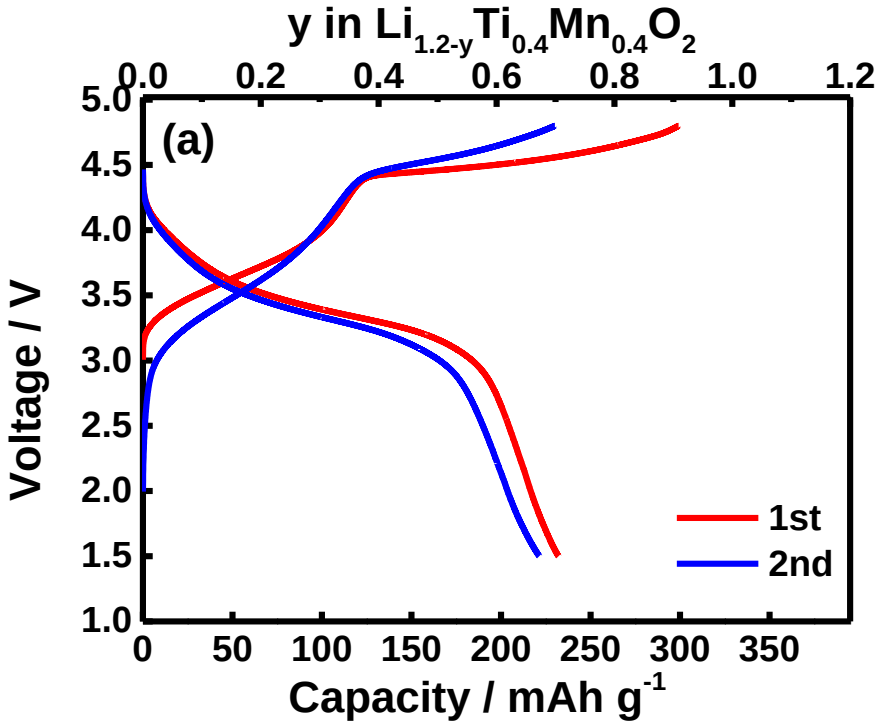

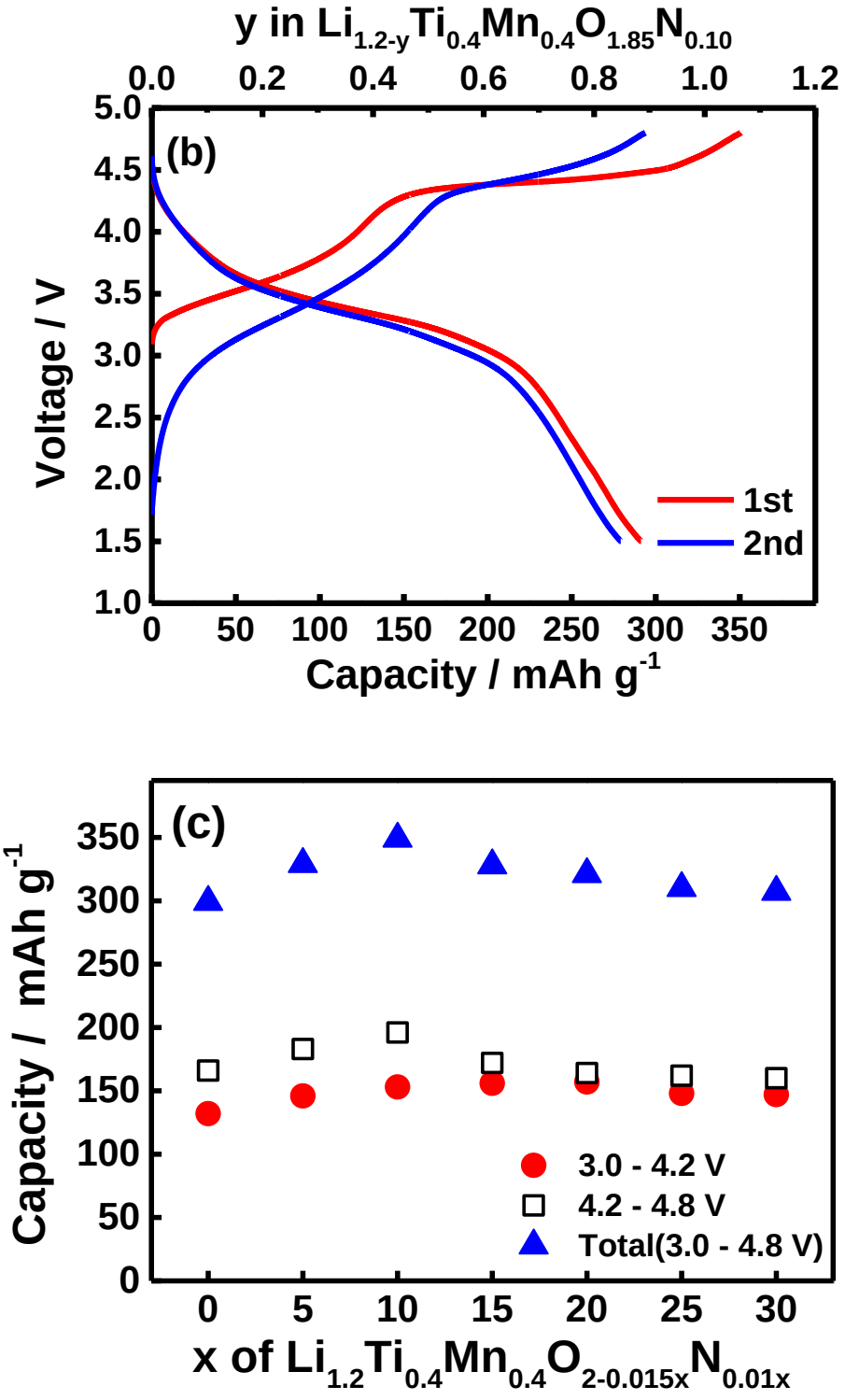

Figure 5-3. C/20 rate galvanostatic charge-discharge curves measured at 50°C for (a) $Li_{1.2}Ti_{0.4}Mn_{0.4}O_2$ cathode, (b) $Li_{1.2}Ti_{0.4}Mn_{0.4}O_{1.85}N_{0.10}$ cathode. (c) Dependence of the 1st charge capacity of each cathode on the amount of nitrogen-doping.

To clarify the electronic structure change of $Li_{1.2-y}Ti_{0.4}Mn_{0.4}O_{1.85}N_{0.10}$ during 1st charge process, soft X-ray absorption spectroscopies (XAS) was performed. Soft XAS for Mn *L*-edge and Ti *L*-edge for $Li_{1.2}Ti_{0.4}Mn_{0.4}O_{1.85}N_{0.10}$ during 1st charge process was performed at different charge states to examine a contribution of transition metal ion (Figure 5-4 and Figure 5-5). Figure 3 shows the Mn *L*-edge XANES spectra of the $Li_{1.2}Ti_{0.4}Mn_{0.4}O_2$ cathode and the $Li_{1.2}Ti_{0.4}Mn_{0.4}O_{1.85}N_{0.10}$ cathode during the 1st charge reaction. In an XAS spectrum of Mn L_{III}-edge for the $Li_{1.2}Ti_{0.4}Mn_{0.4}O_2$ at initial state, a board peak was observed at around 642 eV (Figure 5-4 (a)). The valence of the Mn in the $Li_{1.2}Ti_{0.4}Mn_{0.4}O_2$ was characterized trivalent because the peak shape and energy position was similar to Mn_2O_3 spectra. The peak was separated to two peaks and shifted to a higher energy region after 160 mAh g^{-1} charging (y = 0.49), and the shape and energy position were similar to MnO_2 spectra. This result indicates that Mn ions were oxidized into a tetravalent state. The two peaks were unchanged on a subsequent charge process, proving that Mn ions are not responsible for charge compensation. Similar changes in Mn L_{III}-edge XAS spectra have been also reported in the literature [17]. The Ti *L*-edge XAS spectra did not change during charging process (Figure 5-5), indicating that the Ti ions did not contribute to charge compensation. Nitrogen doping reduced the Mn valence in the $Li_{1.2}Ti_{0.4}Mn_{0.4}O_2$. In an XAS spectrum of Mn L_{III}-edge for the $Li_{1.2}Ti_{0.4}Mn_{0.4}O_{1.85}N_{0.10}$ at initial state, a small peak at 640 eV as well as the broad peak around 640 eV. The small peak position was similar to $MnCO_3$ spectra, indicating that Mn was partly reduced from trivalent to divalent by nitrogen-doping. In the charge process, although the peak was separated to two peaks and shifted to a higher energy region in the charge process, the spectrum changed to 240 mAh g^{-1} (y = 0.73). This result indicates that more electron from Mn ions in the $Li_{1.2}Ti_{0.4}Mn_{0.4}O_{1.85}N_{0.10}$ contributed to the charge compensation during 1st charge process, compared to $Li_{1.2}Ti_{0.4}Mn_{0.4}O_2$. These results correspond to the galvanostatic measurements. The contribution of Ti ions for charge compensation was not confirmed from Ti *L*-edge XAS spectra (Figure 5-5).

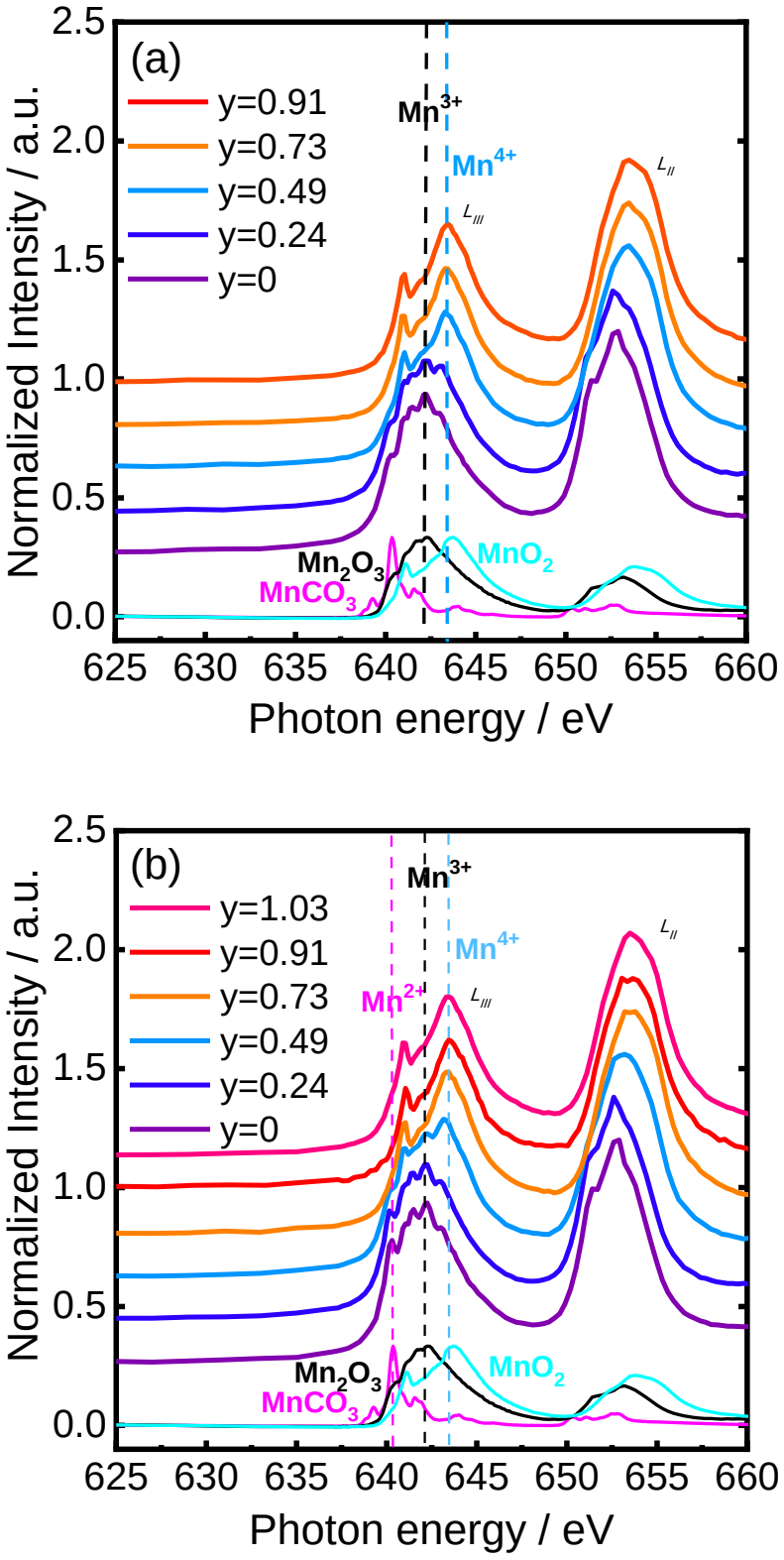

Figure 5-4. Mn *L*-edge XANES spectra during the 1st charge reaction for (a) $Li_{1.2-y}Ti_{0.4}Mn_{0.4}O_2$ cathode and (b) $Li_{1.2-y}Ti_{0.4}Mn_{0.4}O_{1.85}N_{0.10}$ cathode.

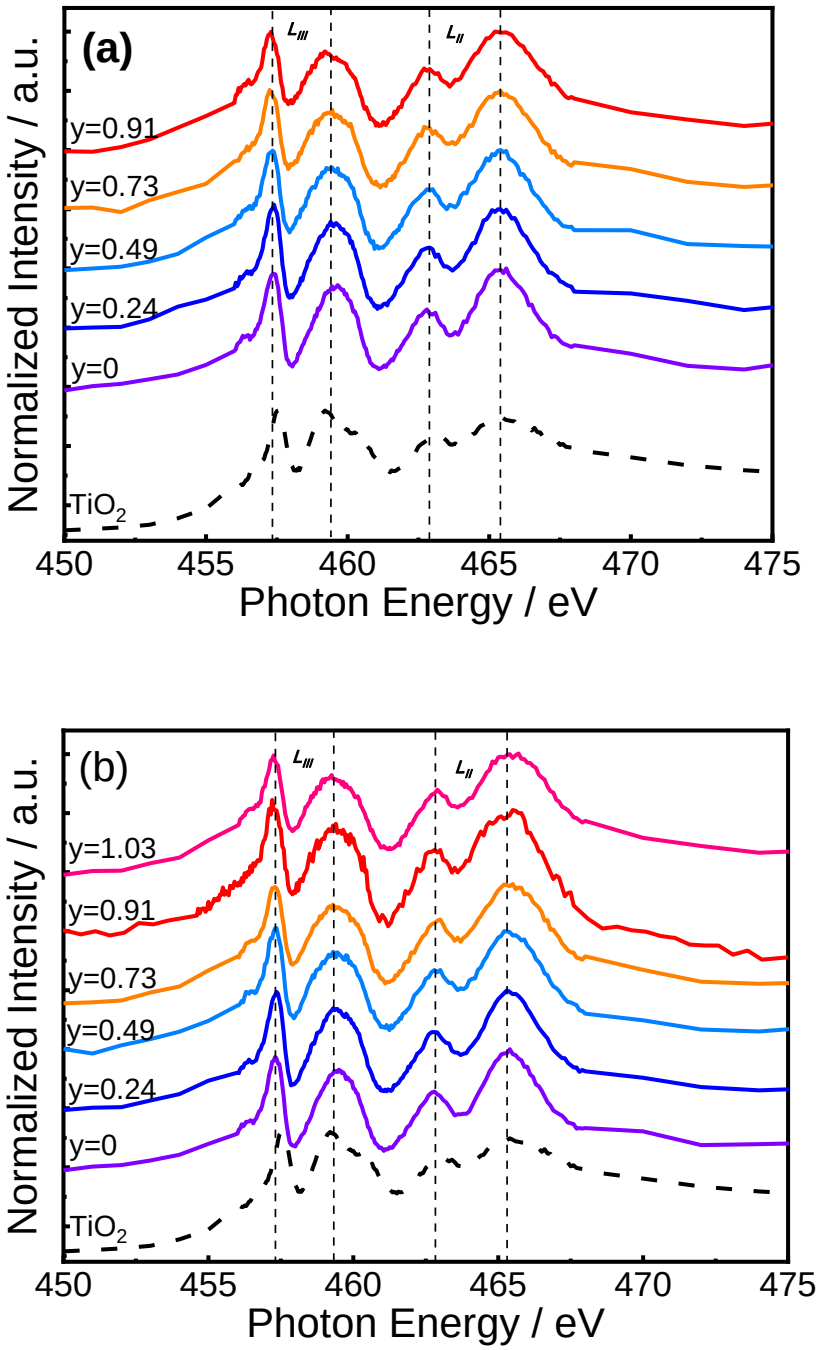

Figure 5-5. Changes in Ti *L*-edge XANES spectra during the 1st cycle for (a) $Li_{1.2-y}Ti_{0.4}Mn_{0.4}O_2$ cathode and (b) $Li_{1.2-y}Ti_{0.4}Mn_{0.4}O_{1.85}N_{0.10}$ cathode.

Contribution of anion for the charge compensation was examined by O *K*-edge XAS measurements. We could not collect N *K*-edge XANES spectra because all the

compound cathode materials contained much more amount of carbon than that of nitrogen. In an XAS spectrum of O *K*-edge for the $Li_{1.2}Ti_{0.4}Mn_{0.4}O_2$, two peaks were observed at 531 eV and 534 eV in the pre-edge region at initial state (Figure 5-6 (a)). The pre-edge peak is attributed to the transitions from the O 1*s* level to the hybridized states of the Mn 3*d* and O 2*p* orbitals [38]. The intensity at 530 eV increased after 160 mAh g^{-1} (y = 0.49), and this change originates from spin multiplicity and crystal field effect with oxidation of Mn ions (Mn^{3+} to Mn^{4+}) as observed in the Mn-L_{III} XANES spectra [17,29,39]. On subsequent charge, the peak intensity at 531 eV increased in the charge capacity from 160 mAh g^{-1} (y = 0.49) to 300 mAh g^{-1} (y = 0.91). This change is attributed to oxidation of oxygen in the $Li_{1.2}Ti_{0.4}Mn_{0.4}O_2$ because oxidation of Mn ions was not observed in the Mn-L_{III} XANES spectra [17,29,39]. In case of the $Li_{1.2}Ti_{0.4}Mn_{0.4}O_{1.85}N_{0.10}$, two peaks were also observed at 531 eV and 534 eV in the pre-edge region at initial state (Figure 5-6 (b)). The intensity at 530 eV increased after 240 mAh g^{-1} (y = 0.73) because of oxidation of Mn ions as observed in the Mn-L_{III} XANES spectra. On subsequent charge, the peak intensity at 531 eV increased in the charge capacity from 240 mAh g^{-1} (y = 0.73) to 300 mAh g^{-1} (y = 0.91), indicating oxidation of oxygen. To evaluate quantitatively hole formation in oxygen for both samples, the peak area charge in the pre-edge region (from 527 eV to 536 eV) on the charge process was estimated by peak integration. The tendency of area changes a difference appeared between $Li_{1.2}Ti_{0.4}Mn_{0.4}O_2$ and $Li_{1.2}Ti_{0.4}Mn_{0.4}O_{1.85}N_{0.10}$ during charge reaction. Compared with the former, the latter has a smaller peak area because Mn is reduced in the initial state, and the increase of the peak area accompanying the oxidation of Mn progresses later. In the range of y> 0.49, the reaction in which oxygen hole formation mainly progresses, and a new peak appears around 531 eV. Therefore, the change in the peak area reflects the reaction of hole formation.The increase of peak area is suppressed in the $Li_{1.2}Ti_{0.4}Mn_{0.4}O_{1.85}N_{0.10}$ by 300 mAh g^{-1} (y = 0.91) charge capacity, compared to the $Li_{1.2}Ti_{0.4}Mn_{0.4}O_2$ (Figure 5-6 (c)). These results indicate that hole formation in oxide ions is relatively suppressed in $Li_{1.2}Ti_{0.4}Mn_{0.4}O_{1.85}N_{0.10}$. Nitrogen doping slowed down the reaction of generating holes in the O-2*p* orbital at the end of the charging process, and made it possible to increase the charge capacity at the same cutoff voltage.

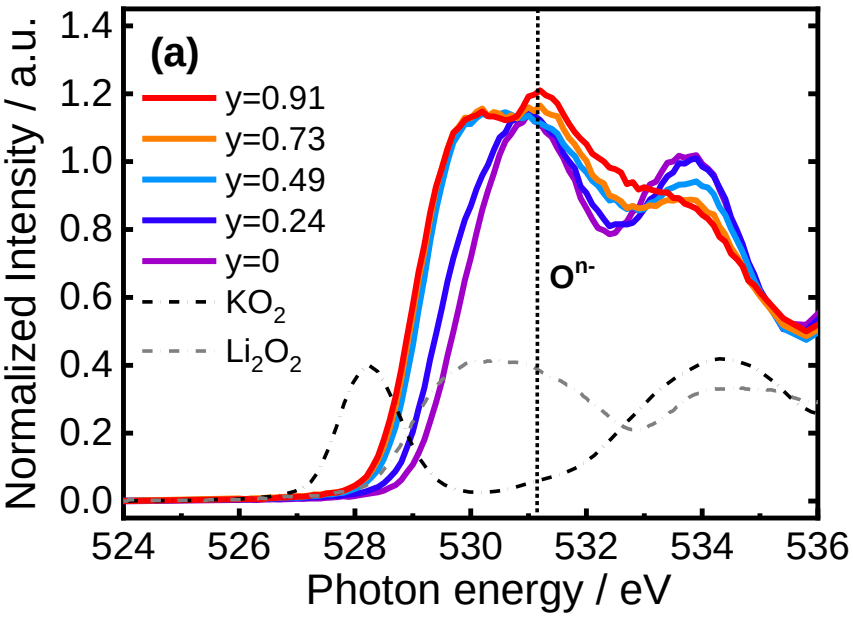
(a)
y=0.91
y=0.73
y=0.49
y=0.24
y=0
KO2
Li2O2
On-
Normalized Intensity / a.u.
Photon energy / eV
0.0
0.2
0.4
0.6
0.8
1.0
1.2
1.4
524
526
528
530
532
534
536

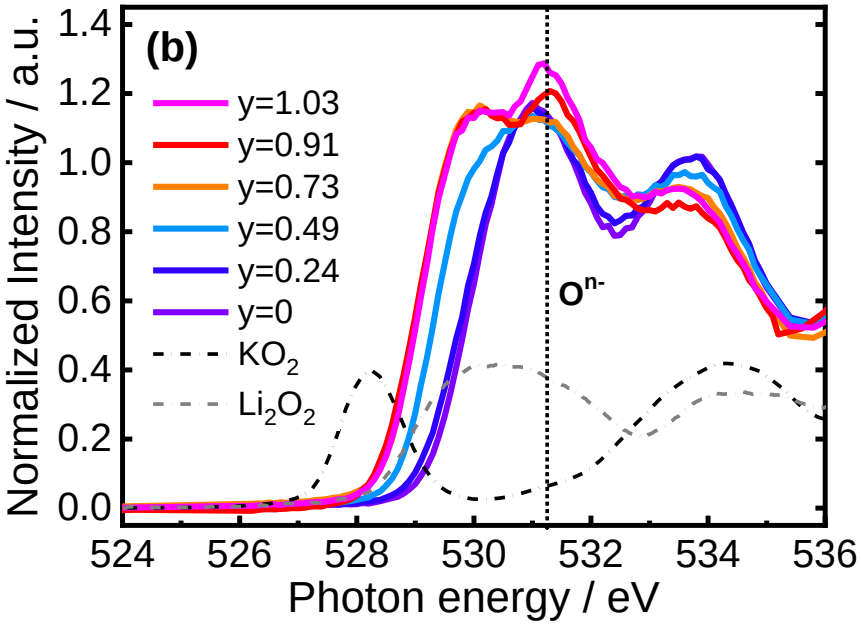
(b)
y=1.03
y=0.91
y=0.73
y=0.49
y=0.24
y=0
KO2
Li2O2
On-
Normalized Intensity / a.u.
Photon energy / eV
0.0
0.2
0.4
0.6
0.8
1.0
1.2
1.4
524
526
528
530
532
534
536

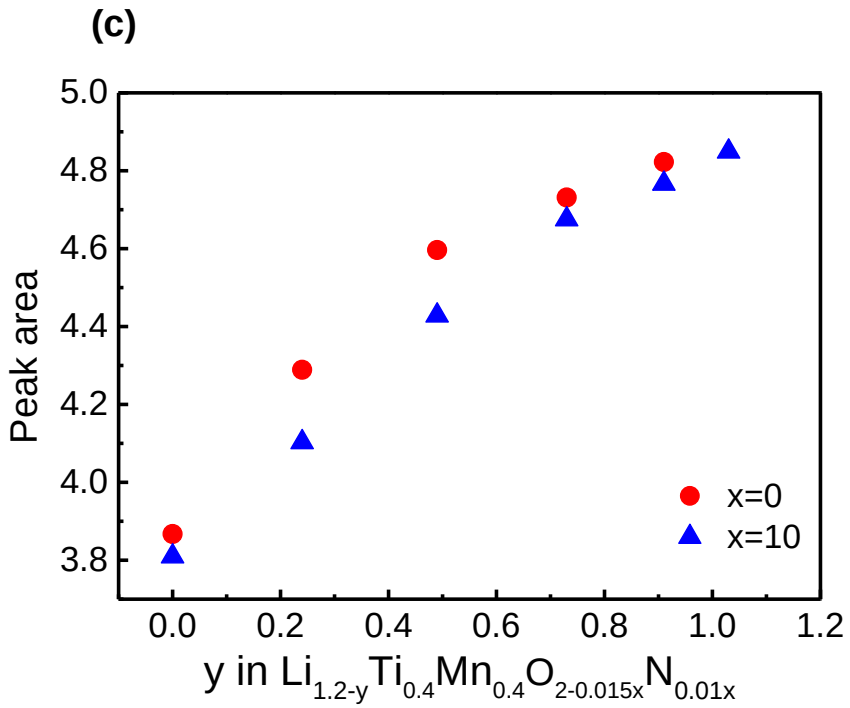

Figure 5-6. Changes in O *K* pre-edge XANES spectra during the 1st charge reaction for (a) $Li_{1.2-y}Ti_{0.4}Mn_{0.4}O_2$ cathode and (b) $Li_{1.2-y}Ti_{0.4}Mn_{0.4}O_{1.85}N_{0.10}$ cathode. (c) Comparison of peak area of O *K* pre-edge XANES (from 527 eV to 536 eV).

5-4. Conclusion

In this study, we proposed nitrogen-doping to the lithium rich cathode materials to charge the state of p-orbitals electron. In the nitrogen cathode, the charge compensation of cathode materials was performed by the Mn oxidization and hole formation on O-2*p* orbital. The obtained nitrogen-doped lithium rich cation-disordered cathodes with optimized composition, $Li_{1.2}Ti_{0.4}Mn_{0.4}O_{1.85}N_{0.10}$, demonstrated the higher capacity of 350 mAh g^{-1} because of the effective reduction of Mn compared with the non-doped cathode and the promotion of oxygen hole formation during the charge reaction. The nitrogen-doping cathodes have potential to create new lithium rich cathode materials which achieves greater electrochemical performance without using the high-cost transition metals.

5-5. References

[1] B. Dunn, Kamath, and J.-M Tarascon, “Electrical energy storage for the grid: a battery of choices. ” *Science*. **334**, 928–93, (2011).

[2] K. Mizushima, P. C. Jones, P. J. Wiseman and J. B. Goodenough, “$LI_XCOO_2(0 < x \leq 1)$: a new cathode material for batteries of high-energy density.” *Mater. Res. Bull.* **15,** 783-789, (1980).

[3] A. D. Robertson and P. G. Bruce, “Mechanism of electrochemical activity in Li_2MnO_3.” *Chem. Mater.*, **15**, 1984−1992, (2003).

[4] Z. Lu and J.R. Dahn, “Layered Cathode Materials Li $[NixLi_{(1/3-2x/3)}Mn_{(2/3-x/3)}]O_2$ for Lithium-Ion Batteries.” *Electrochem. Solid. St.*, **4**, A191-A194, (2001).

[5] T. Ohzuku, M. Nagayama, K. Tsuji and K. Ariyoshi, “High-capacity lithium insertion materials of lithium nickel manganese oxides for advanced lithium-ion batteries: toward rechargeable capacity more than 300 mA h g^{-1}.” *J. Mater. Chem.* **21**, 10179-10188, (2011).

[6] A.R. Armstrong, M. Holzapfel, P. Novak, C.S. Johnson, S.H. Kang,M.M. Thackeray and P. G. Bruce, “Demonstrating Oxygen Loss and Associated Structural Reorganization in the Lithium Battery Cathode $Li[Ni_{0.2}Li_{0.2}Mn_{0.6}]O_2$.” *J. Am. Chem. Soc.* **128**, 8694-8698, (2006).

[7] N. Yabuuchi, K. Yoshii, S-T. Myung, I. Nakai, and S. Komaba, “Detailed Studies of a High-Capacity Electrode Material for Rechargeable Batteries, Li_2MnO_3−$LiCo_{1/3}Ni_{1/3}Mn_{1/3}O_2$.” *J. Am. Chem. Soc.* **133**, 4404-4419, (2011).

[8] M. Sathiya, K. Ramesha, G. Rousse, D. Foix, D. Gonbeau, A. S. Prakash, M-L. Doublet, K. Hemalatha and J-M. Taracson, “High Performance $Li_2Ru_{1-y}Mn_yO_3$ ($0.2 \leq y \leq 0.8$) Cathode Materials for Rechargeable Lithium-Ion Batteries: Their Understanding.” *Chem. Mater.* **25**, 1121-1131, (2013).

[9] M. Sathiya, “Reversible anionic redox chemistry in high capacity layered-oxide electrodes.” *Nat. Mater.* **12**, 827-835, (2013).

[10] J. Lee, A. Urban, X. Li, D. Su, G. Hautier and G. Ceder, “Unlocking the Potential of Cation-Disordered Oxides for Rechargeable Lithium Batteries.” *Science.* **343**, 519-522, (2014).

[11] M. Sathiya, A. M. Abakumov, D. Foix, G. Rousse, K. Ramesha, M. Saubanere, M-L. Doublet, H. Vezin, C. P. Laisa, A.S. Prakash, D. Gonbeau, G. VanTendeloo and J-M. Tarascon, “Origin of voltage decay in high-capacity layered oxide electrodes.” *Nat. Mater*. **14**, 230-238, (2014).

[12] R. Wang, X. Li, L. Liu, J. Lee, D-H. Seo, S-H. Bo, A. Urban and G. Ceder, “A disordered rock-salt Li-excess cathode material with high capacity and substantial oxygen redox activity: $Li_{1.25}Nb_{0.25}Mn_{0.5}O_2$.” *Electrochem. Commun.*, **60**, 70−73, (2015).

[13] J. Lee, D. H. Seo, M. Balasubramanian, N. Twu, X. Li and G. Ceder, “A new class of high capacity cation-disordered oxides for rechargeable lithium batteries: Li-Ni-Ti-Mo oxides.” *Energy Environ. Sci.* **8**, 3255-3265, (2015).

[14] E. McCalla, A. M. Abakumov, M. Saubanere, D. Foix, E. J Berg, G. Rousse, M-L.Doublet, D. Gonbeau, P. Novak, G. V.Tendello, R. Dominko and J-M. Tarascon, “Visualization of O-O peroxo-like dimers in high-capacity layered oxides for Li-ion batteries.” *Science*. **18**, 1516-1521, (2015).

[15] E. McCalla, A. Abakumov, G. Rousse, M. Reynaud, M.T. Sougrati, B. Budic, A. Mahmoud, R. Dominko, G. V. Tendeloo, R. P. Hermann and J-M.Tarascon, “Novel complex stacking of fullyordered transition metal layers in Li_4FeSbO_6 materials.” *Chem. Mater.*, **27**, 1699−1708, (2015).

[16] N. Yabuuchi, N. Takeuchi, M. Nakayama, H. Shiiba, M. Ogawa, K. Yamanaka. T.Ohta, D. Endo, T. Ozaki, T. Inamasu, K. Sato and S. Komaba, “High-capacity electrode materials for rechargeable lithium batteries: Li_3NbO_4 -based system with cation-disordered rocksalt structure.” *Proc. Natl Acad. Sci. USA.* **112**, 7650-7655 (2015).

[17] N. Yabuuchi, M. Nakayama, M. Takeuchi, S. Komaba, Y. Hashimoto, T. Mukai, H. Shiiba, K. Sato, Y. Kobayashi, A. Nakao, M. Yonemura, K. Yamanaka, K. Mitsuhara and T. Ohta, “Origin of stabilization and destabilization in solid-state redox reaction of oxide ions for lithium-ion batteries.” *Nat. Commun*. **7**, 13814, (2016).

[18] N. Yabuuchi, Y. Tahara, S. Komaba, S. Kitada and Y. Kajiya, “Synthesis and electrochemical properties of Li_4MoO_5-NiO binary system as positive electrode materials for rechargeable lithium batteries.” *Chem. Mater*., **28**, 416−419, (2016).

[19] P. E. Pearce, A. J. Perez, G. Rousse, M. Saubanère, D. Batuk, D. Foix, E. McCalla, A. M. Abakumov, G.V. Tendeloo, M-L.Doublet and J-M. Tarascon, “Evidence for anionic redox activity in a tridimensional-ordered Li-rich positive electrode β-Li_2IrO_3.” *Nat. Mater*., **16**, 580−586, (2017).

[20] A. J. Perez, Q. Jacquet, D. Batuk, A. Iadecola, M. Saubanère, G. Rousse, D.Larcher, H. Vezin, M-L. Doublet and J-M. Tarascon, “Approaching the limits of cationic and anionic electrochemical activity with the Li-rich layered rocksalt Li_3IrO_4.” *Nat. Energy*, **2**, 954−962 (2017).

[21] M. Saubanere, E. McCalla, J-M. Tarascon, and M-L. Doublet, “The intriguing question of anionic redox in high-energy density cathodes for Li-ion batteries.” *Energy Environ. Sci.* **9**, 984-991, (2016).

[22] K. Luo, M.R. Roberts, R. Hao, N. Guerrini, D. M. Pickup, Y. S. Liu, K. Edstrom, J. H. Guo, A. V. Chadwick, L. C. Duda and P. G. Bruce, “Charge-compensation in 3d-transition-metaloxide intercalation cathodes through the generation of localized electron holes on oxygen.” *Nat. Chem.* **8**, 684-691, (2016).

[23] D. H. Seo, J. Lee, A. Urban, R. Malik, S. Y. Kang and G. Ceder, “The structural and chemical origin of the oxygen redox activity in layered and cation-disordered Li-excess cathode materials.” *Nat. Chem.* **8**, 692-697, (2016).

[24] N. Yabuuchi, “Solid-state redox reaction of oxide ions for rechargeable batteries.” *Chem. Lett.,* **46**, 412−422 (2017).

[25] G. Assat, J-M. Tarascon, “Fundamental understanding and practical challenges of anionic redox activity in Li-ion batteries.” *Nat. Energy,* **3**, 373−386, (2018).

[26] J. Hong, W. E. Gent, P. Xiao, K. Lim, D-H. Seo, J. Wu, P. M. Csernica, C. J.Takacs, D. Nordlund, C-J. Sun, K. H. Stone,D. Passarello,W. Yang, D. Prendergast, G. Ceder, M. F. Toney, W. C. William C. Chueh, “Metal-oxygen decoordination stabilizes anion redox in Li-rich oxides.” *Nat. Mater.*, **18**, 256−265, (2019).

[27] M. B. Yahia, J. Vergnet, M. Saubanère, and M-L. Doublet, “Unified picture of anionic redox in Li/Na-ion batteries.” *Nat. Mater.,* **18**, 496−502 (2018).

[28] N. Yabuuchi, “Material design concept of lithium-excess electrode materials with rocksalt-related structures for rechargeable non-aqueous batteries.” *Chem. Rec.*, **19**, 690−707, (2019).

[29] K. Yamamoto, Y. Zhou, N. Yabuuchi, K. Nakanishi, T. Yoshinari, T. Kobayashi, Y. Kobayashi, R. Yamamoto, A. Watanabe, Y. Orikasa, K. Tsuruta, J. Park, H. R. Byon, Y. Tamenori, T. Ohta and Y. Uchimoto, “Charge Compensation Mechanism of Lithium-excess Metal Oxides with Different Covalent and Ionic Characters revealed by *operando* Soft and Hard X-ray Absorption Spectroscopy.” *Chem. Mater.*, in press.

[30] J. O. Binder, S. P. Culver, R. Pinedo, D. A. Weber, M. S. Friedrich, K. I. Gries, K. Volz, W. G. Zeier and J. Janek, Investigation of “Fluorine and Nitrogen as Anionic Dopants in Nickel-Rich Cathode Materials for Lithium-Ion Batteries.” *ACS Appl. Mater. Interfaces.* **10**, 44452-44462, (2018).

[31] H. Z. Zhang, Q. Q. Qiao, G. R. Li, S. H. Ye and X. P. Gao, “Surface nitridation of Li-rich layered $Li(Li_{0.17}Ni_{0.25}Mn_{0.58})O_2$ oxide as cathode material for lithium-ion battery.” *J. Mater. Chem.* **22**, 13104-13109, (2012).

[32] E. M. Erickson, H. Sclar, F. Schipper, J. Liu, R. Tian, C. Ghanty, L. Burstein, N. Leifer, J. Grinblat, M. Talianker, J. Y. Shin, J. K. Lampert, B. Markovsky, A. I. Frenkel and D. Aurbach, “High-Temperature Treatment of Li-Rich Cathode Materials with Ammonia: Improved Capacity and Mean Voltage Stability during Cycling.” *Adv. Energy Mater.* **7**, 1700708, (2017).

[33] X. Li, Z. Xie, W. Liu, W. Ge, H. Wang and M. Qu, “Effects of fluorine doping on structure, surface chemistry, and electrochemical performance of $LiNi_{0.8}Co_{0.15}Al_{0.05}O_2$.” *Electrochim. Acta.* **174**, 1122-1130, (2015).

[34] F. Kong, C. Liang, R.C. Longo, D. H. Yeon, Y. Zheng, J. H. Park, S. G. Doo and K. Cho, “Conflicting Roles of Anion Doping on the Electrochemical Performance of Li-Ion Battery Cathode Materials.” *Chem. Mater.* **28**, 6942-6952, (2016).

[35] J. Lee, J. K. Papp, R. J. Clement, S. Sallis, D. H. Kwon, T. Shi, W. Yang, B. D. McCloskey and G. Ceder, “Mitigating oxygen loss to improve the cycling performance of high capacity cation-disordered cathode materials.” *Nat. Commun.* **8**, 981, (2017).

[36] A. Fukushima, A Hayashi, H. Yamamura and M. Tatsumisago, “Mechanochemical synthesis of high lithium ion conducting solid electrolytes in a Li_2S-P_2S_5-Li_3N system.” *Solid State Ionics.* **304**, 85-89, (2017).

[37] R. D. Shannon, “Revised effective ionic radii and systematic studies of interatomic distances in halides and chalcogenides.” *Acta Crystallogr*. **A32**, 751-767, (1976).

[38] W. S. Woon, M. Balasubramanian, K. Y. Chung, X. Q. Yang, J. McBreen, C. P. Grey and D. A. Fischer, “Investigation of the Charge Compensation Mechanism on the Electrochemically Li-Ion Deintercalated $Li_{1-x}Co_{1/3}Ni_{1/3}Mn_{1/3}O_2$ Electrode System by Combination of Soft and Hard X-ray Absorption Spectroscopy.” *J. Am. Chem. Soc*. **127**, 17479-17487, (2005).

[39] M. Oishi, K. Yamanaka, I. Watanabe, K. Shimoda, T. Matsunaga, H. Arai, Y. Ukyo, Y. Uchimoto, Z. Ogumi and T. Ohta, “Direct observation of reversible oxygen anion redox reaction in Li-rich manganese oxide, Li_2MnO_3, studied by soft X-ray absorption spectroscopy.” *Mater. Chem. A*. **4**, 9293-9302, (2016).

Chapter 6. Improvement of Rate Performance by Nitrogen-doping to Lithium Rich Cathode Materials

6-1. Introduction

Conventional cathode materials such as layered oxide $LiCoO_2$, spinel $LiMn_2O_4$ and olivine $LiFePO_4$ have been successfully applied in lithium ion batteries as mentioned in Chapter 1. These cathode materials typically deliver capacities about 150 mAh g^{-1}. To satisfy the requirements for electric vehicles, it is desired to develop new cathode materials with superior performance such as higher capacities, lower cost, and better rate performances.

Lithium-rich materials are representatives for the next generation cathode because of their high theoretial capacity over 300 mAh g^{-1} [1-3]. The charge compensation mechanism of lithium rich cathodes are cationic redox reaction and/or anionic redox reaction [1-3]. However, anionic redox reaction leads to phase transition [4] and irreversible oxygen loss [5]. The Li_2MnO_3-systems shows typical plateau at the 4.5 V, which is compensated by oxygen oxidization [1-3]. However, the Li^+ diffusion coefficients in the plateau region of the first charge were very small, which could be attributed to the high kinetic barriers associated with the concurrent Li^+ extraction, oxygen loss, and structural rearrangement [6]. Then, to stabilize the anionic redox reaction would be essential to design and develop new cathode materials with high rate performance.

For the improvement of rate performance, supressing the oxygen loss from lattice is the common approach. Then, various types of lithium rich cathode materials formed by the substitution of transition metals have been extensively studied [7-23]. The 4*d* and 5*d* metal oxides such as Li_2RuO_3-systems and Li_2IrO_3 ,which have strong covalent bonding between transition metals 4*d*/5*d* and O 2*p* orbitals, enables charge compensation by the oxidation of oxide ions to peroxide species [4,5,16-18]. Sathiya et al. has suggested The electronic state of each atoms during the charge-discharge process has been identified as a charge compensation by the oxidation of $O^{2-}$to an $(O_2)^{n-}$ species (peroxide species: O-O distance 2.42 Å) [15,16]. Luo et al., has suggested that

solid-solution oxide exhibited formation of isolated holes on oxide ions [19] where non-bonding oxygen orbital in the Li-O-Li configuration for the lithium excess system could energetically stabilize holes.

Another concept to improve the rate performance is to increase the rate of charge compensation of the transition metal, which is kinetically faster than anionic redox reaction. R. A. House et al., synthesized fluorine-doped Li_2MnO_2F cathode, which is the valence of Mn is 3+ at the pristine state [24]. By the flourine doping, the charge compensation mechanism has changed to the combination of Mn oxidization and oxygen oxidization, not like the Li_2MnO_3, showed the better rate performance. The similar type fluorine-doped cathode materials have been reported by J. Lee et al. [25], F. Kong et al. [26], and Yabuuchi et al.[27,28], however, these cathodes also showed the capacity fading with electrochemical cycles. This is a problem that needs to be solved in the future.

In this work, we focus on the oxynitride material $Li_{1.2}Ti_{0.4}Mn_{0.4}O_{2-0.015x}N_{0.01x}$ reported in Chapter 5. These nitrogen-doped cathodes show higher capacity compared to the non-doped cathode. Furthermore, it is considered that an appropriate amount of nitrogen doping has an effect of stabilizing the anion redox reaction of the lithium-rich cathode material. If the anion redox reaction is stabilized, there is a possibility that the material system exhibits rate performance. Then, we will investigate the rate performance of $Li_{1.2}Ti_{0.4}Mn_{0.4}O_{2-0.015x}N_{0.01x}$ materials and performed the local structure analysis by Hard-XAS measurements.

6-2. Experimental

6-2-1. Sample preparation

Powder of cathode materials $Li_{1.2}Ti_{0.4}Mn_{0.4}O_{2-0.015x}N_{0.01x}$ (x = 0, 5, 10, 15, 20, 25, 30) were synthesized by the mechanochemical ball milling [29]. Stoichiometric amounts of Li_2O, TiO_2 (anatase), Mn_2O_3 (trivalent: 3+) and Li_3N were scaled and put into the ball-milling pot with 10mmφ zirconia balls in Ar-filled glovebox. These starting materials were thoroughly mixed by dry mechanical ball milling at 370 rpm for 48 hours and then the mixtures were pressed into pellets. The pellets were heated at 900 °C for 1 hour (for x = 5, 10, 15, 20, 25, 30) or 12 hours (for x = 0). Each obtained pellet

was ground into fine powders and mixed with 10 wt% acetylene black by dry ball-milling at 300 rpm. Particle morphologies of the samples were observed using a scanning electron microscope (S-3400N, HITACHI). All obtained powders were characterized by synchrotron radiation (SR) X-ray powder diffraction (XRD) experiments at SPring-8 BL02B2.

6-2-2. Eletrochemical measurements

Compound cathodes (already mixed with carbon) were prepared from the paste which was produced by mixing 70 wt% of as-prepared active materials (carbon-coated), 20 wt% of acetylene black and 10 wt% of polyvinylidene difluoride binder in 1-methyl-2-pyrrolidone solvent, and then this paste was coated on the Al foil. Li foil was used as the counter electrode material and 1 mol dm^{-3} $LiPF_6$ in an acetonitrile solvent was used as an electrolyte. The 2032-type coin cells were assembled in the Ar-filled glove box.

The charge discharge performance of these cathode materials were tested by galvanostatic charge-discharge measurements. The current densities were determined by the hypothesis as all Li ion could be removed in the charge-discharge process where 1C rate was designated as 395 mA g^{-1} in all cathodes. In this work, the current rate was changed at C/50, C/20, C/10, C/2, 1C, 2C and 5C. The cut-off voltage was between 1.5 V and 4.8 V (vs. Li/Li^+) and the constant-current charge discharge measurements were operated at 50 °C.

6-2-3. X-ray absorption spectroscopies

Hard X-ray absorption spectroscopy (XAS) measurements for Ti *K*-edge and Mn *K*-edge were performed in SPring-8 BL14B2. Three electrodes ($Li_{1.2}Ti_{0.4}Mn_{0.4}O_2$, $Li_{1.2}Ti_{0.4}Mn_{0.4}O_{1.93}N_{0.05}$ and $Li_{1.2}Ti_{0.4}Mn_{0.4}O_{1.85}N_{0.10}$) were prepared for the ex-situ XAS measurement in the same condition of the galvanostatic charge-discharge measurements (Current rate: C/20). After having finished the charge discharge measurements, the cells were dissembled in an argon-filled glove box. Then electrodes were flushed the electrolyte with the dimethyl carbonate three times and dried in the Ar atmosphere with

vacuum. To prevent the electrode samples from being exposed to the air, they were packed by laminated sheets filled with Ar gas.

6-3. Results and discussion

Obtained materials were shown in Figure 6-1 (a). The $Li_{1.2}Ti_{0.4}Mn_{0.4}O_{2-0.015x}N_{0.01x}$ in the range from x = 0 to x = 30 had the cation-disordered rocksalt structure classified to a single phase of the *Fm-3m* space group. The particle size of $Li_{1.2}Ti_{0.4}Mn_{0.4}O_2$ mixed with carbon was less than about 1 μm, and the other obtained nitrogen-doped materials had almost the same size as shown in Figure 6-1 (b) - (d). Since the electrochemical performances are greatly affected by the morphology, the particle size needed to be controlled so that there was no difference in particle size between samples.

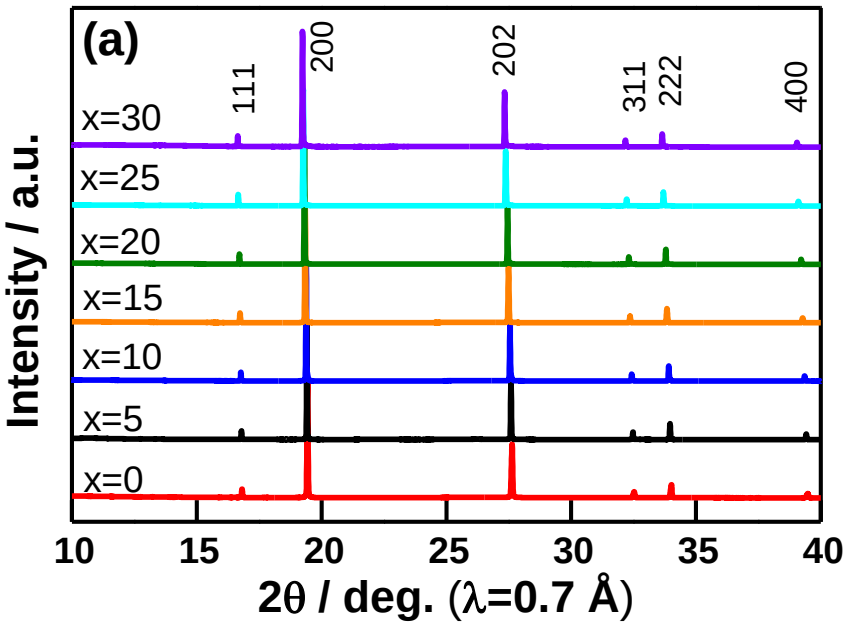

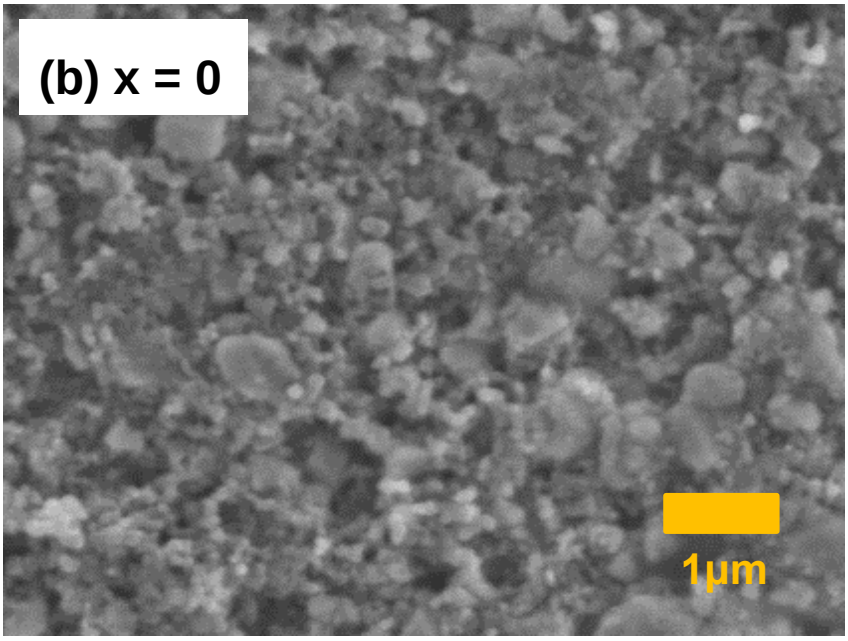
(b) x = 0
1μm

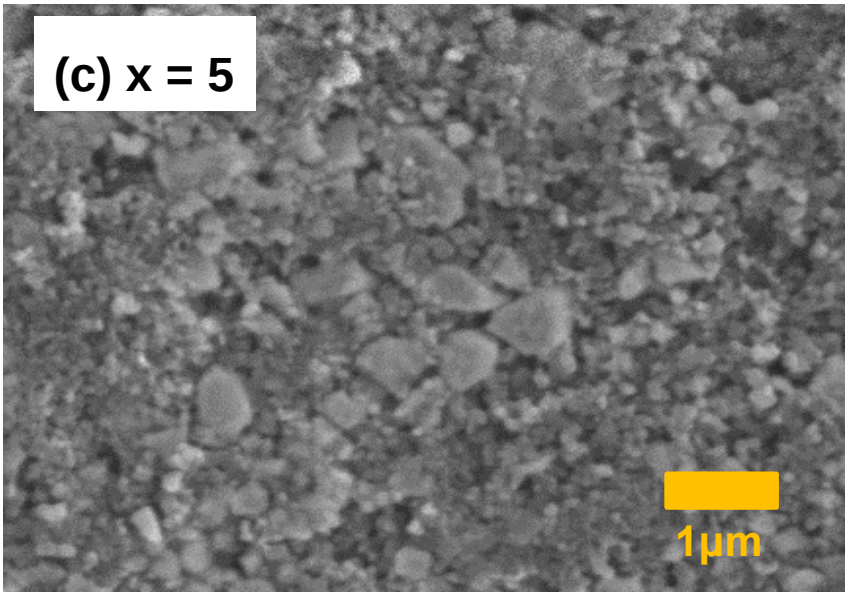
(c) x = 5
1μm

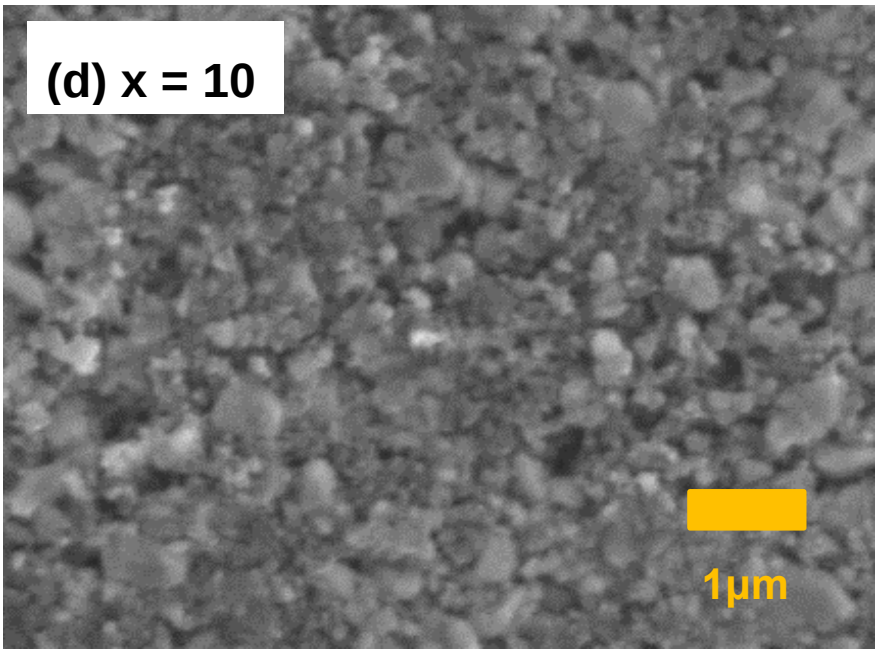

Figure 6-1. (a) Synchrotron XRD spectra for $Li_{1.2}Ti_{0.4}Mn_{0.4}O_{2-0.015x}N_{0.01x}$. (b) - (d) SEM images of carbon coated $Li_{1.2}Ti_{0.4}Mn_{0.4}O_{2-0.015x}N_{0.01x}$ samples.

The results of 1st cycle charge-discharge performance of $Li_{1.2}Ti_{0.4}Mn_{0.4}O_{2-0.015x}N_{0.01x}$ cathodes (x = 0, 5, 10, 20 and 30) are shown in Figure 6-2. The current rate of each measurements were performed at C/20. The obtained 1st charge capacities of x = 0, x = 5, x = 10, x = 20 and x =30 are 299 mAh g^{-1}, 329 mAh g^{-1}, 349 mAh g^{-1}, 321 mAh g^{-1} and 307 mAh g^{-1}, respectively (For the reference, Figure 5-3 (c)). The $Li_{1.2}Ti_{0.4}Mn_{0.4}O_{1.85}N_{0.10}$ showed largest charge capacity among these five compounds (349 mAh g^{-1}). Nitrogen doping in the range from x = 0 to x=10 improved the electrochemical performance, however, more amount of nitrogen doping (x = 20 and 30) decreased 1st charge capacity.

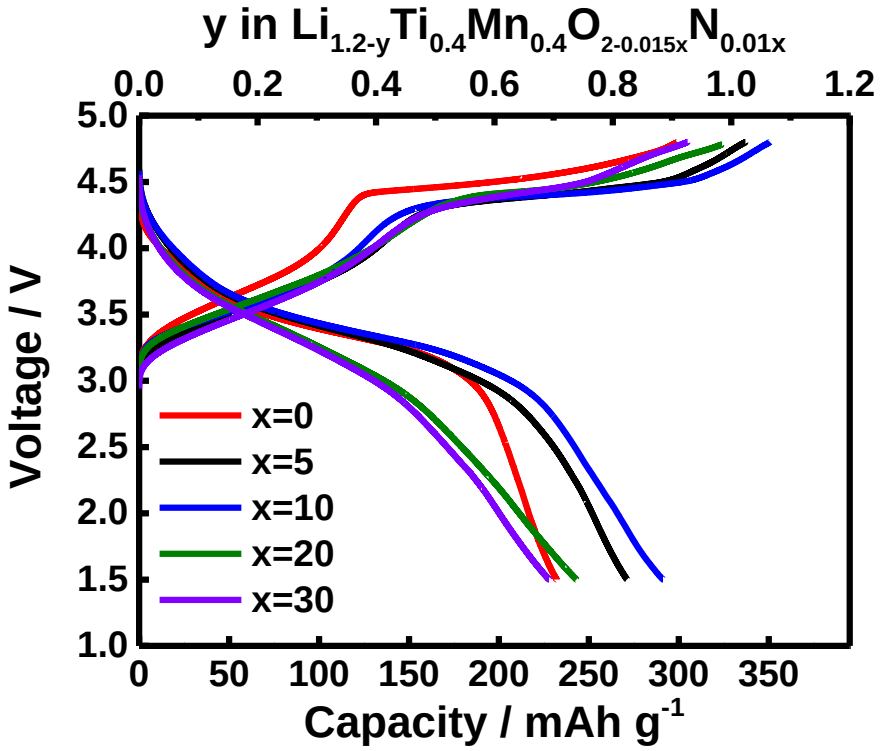

Figure 6-2. The C/20 rate galvanostatic 1st cycle charge-discharge curves measured at 50°C for $Li_{1.2}Ti_{0.4}Mn_{0.4}O_{2-0.015x}N_{0.01x}$ cathodes (x = 0, 5, 10, 20 and 30).

Figure 6-3 shows the dependence of the 1st discharge capacity on the current rate which shows the rate performance of each cathode material. The $Li_{1.2}Ti_{0.4}Mn_{0.4}O_{1.85}N_{0.10}$ cathode showed the largest capacity and the $Li_{1.2}Ti_{0.4}Mn_{0.4}O_{1.93}N_{0.05}$ cathode showed the second-largest capacity for all the current rate. This tendency was noticeable at the higher current rate, especially at 1C and 2C rate. The 1st discharge capacity of the non-doped cathode was not much more than 50 mAh g^{-1}, while that of the nitrogen-doped $Li_{1.2}Ti_{0.4}Mn_{0.4}O_{1.85}N_{0.10}$ cathode was about 150 mAh g^{-1}. The improved high-rate capability of the nitrogen-doped sample is probably due to fast charge-transfer kinetics arising from the nitrogen-doping effect.

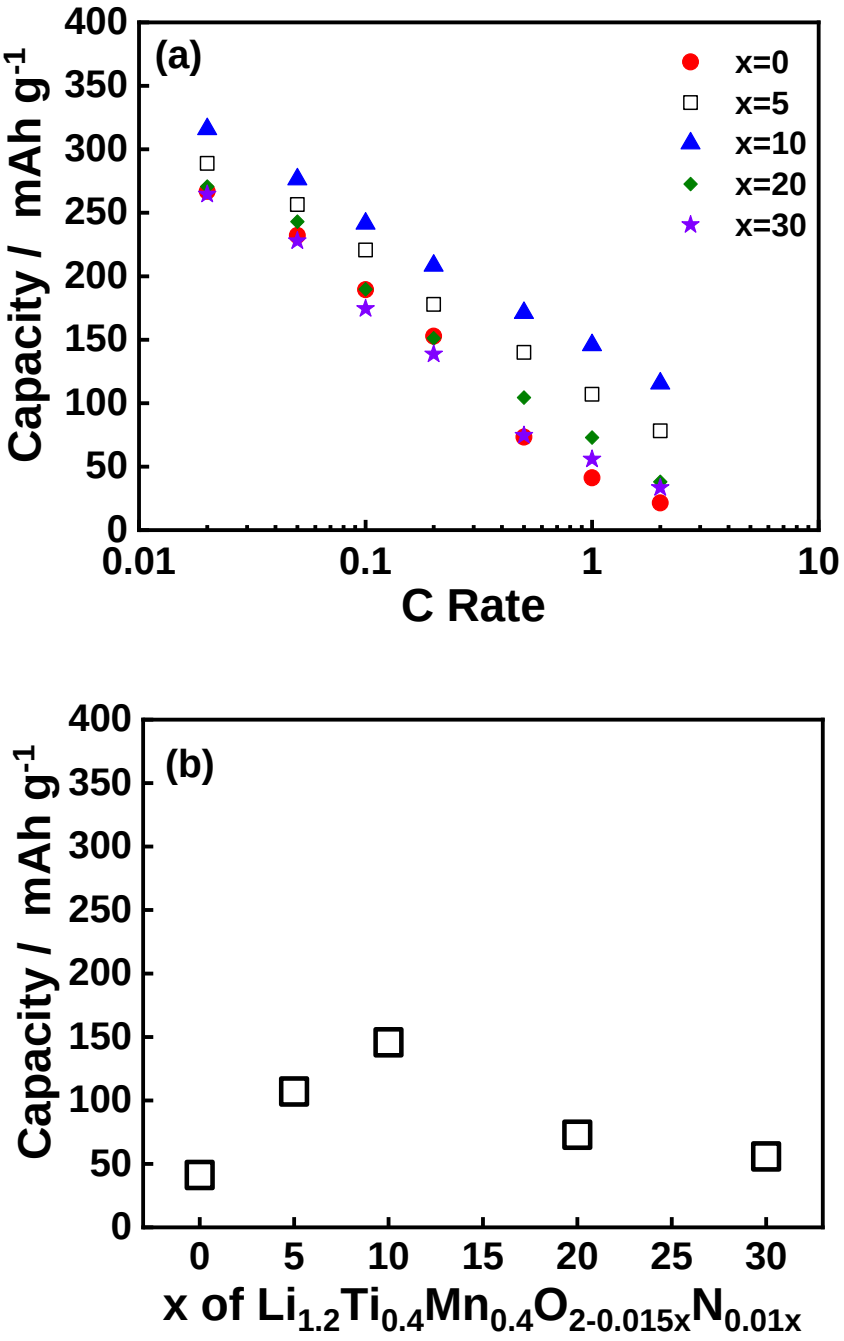

Figure 6-3. (a) Dependence of the 1st discharge capacity of $Li_{1.2}Ti_{0.4}Mn_{0.4}O_{2-0.015x}N_{0.01x}$ cathode on current rate. (b) Dependence of the 1st charge capacity of each cathode at 1C rate on the amount of nitrogen-doping.

Local structures of the $Li_{1.2}Ti_{0.4}Mn_{0.4}O_{2-0.015x}N_{0.01x}$ (x = 0 and 10) cathodes were obtained by the Fourier transformation of the Mn and Ti *K*-edge extended X-ray absorption fine structure (EXAFS) spectra. Figure 6-4 (a) and (b) show the change of the atomic distance of Mn-O and Ti-O in each cathode. Before the charge reaction, Mn-O distance increased by the nitrogen-doping because of the reduction of Mn. After the middle of charge process, variations of Mn-O distance were almost same but Ti-O distance increased associated with the oxidation of oxide ions. These results indicate that the hole formation reaction occurred around the Ti atom. Moreover, in the charge process, the variations of Mn-O distance were longer and Ti-O distance of nitrogen-doped cathodes were shorter than that of the non-doped cathode. Figure 6-4 (c) and (d) show the Debye-Waller factor (DW factor) of Mn-O and Ti-O. Since the DW factor suggests a local distortion, there was little change of Mn-O DW factor among cathodes with different y values, however the Ti-O DW factor of the nitrogen-doped cathodes were decreased compared with the non-doped cathode. The result indicates that the nitrogen-doped cathodes had less distorted structure than the non-doped cathodes which had more stable structure.

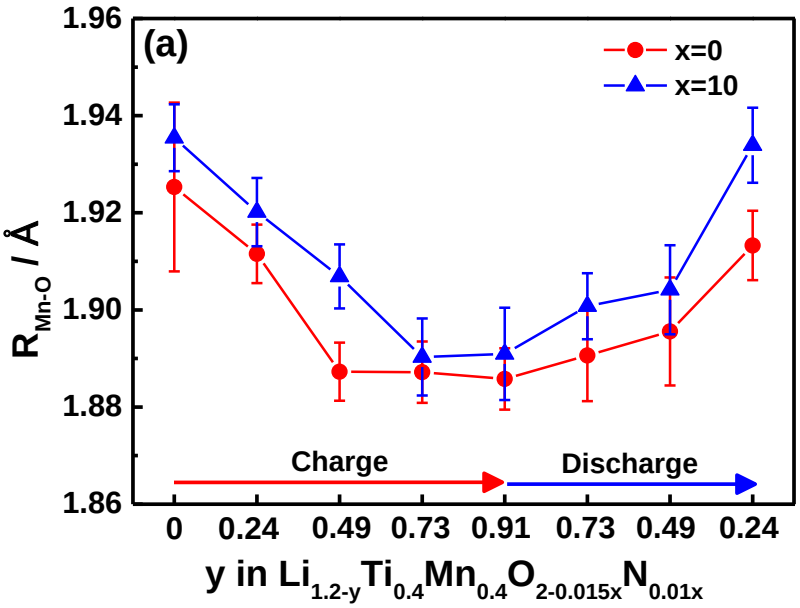

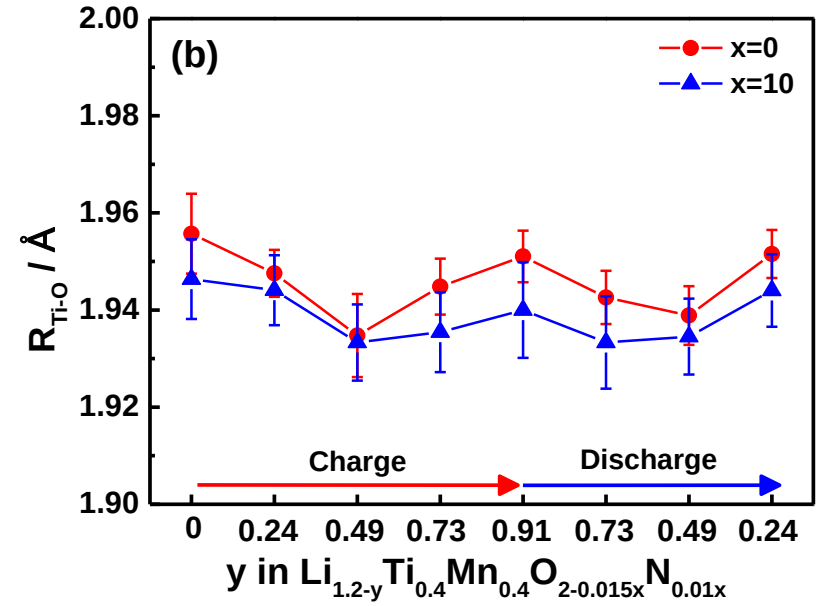
(b)
x=0
x=10
2.00
1.98
1.96
1.94
1.92
1.90
R_{Ti-O} / Å
Charge
Discharge
0
0.24
0.49
0.73
0.91
0.73
0.49
0.24
y in $Li_{1.2-y}Ti_{0.4}Mn_{0.4}O_{2-0.015x}N_{0.01x}$

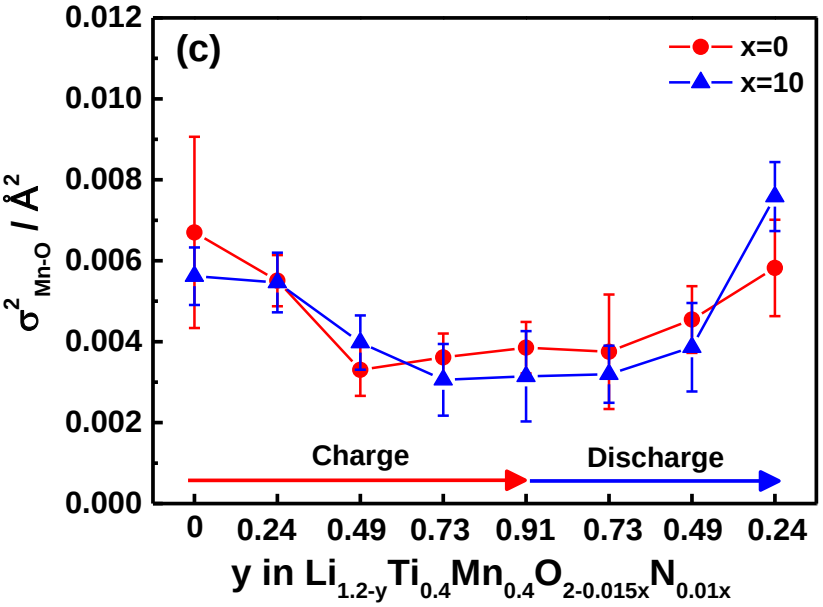
(c)
x=0
x=10
0.012
0.010
0.008
0.006
0.004
0.002
0.000
σ^2_{Mn-O} / Å^2
Charge
Discharge
0
0.24
0.49
0.73
0.91
0.73
0.49
0.24
y in $Li_{1.2-y}Ti_{0.4}Mn_{0.4}O_{2-0.015x}N_{0.01x}$

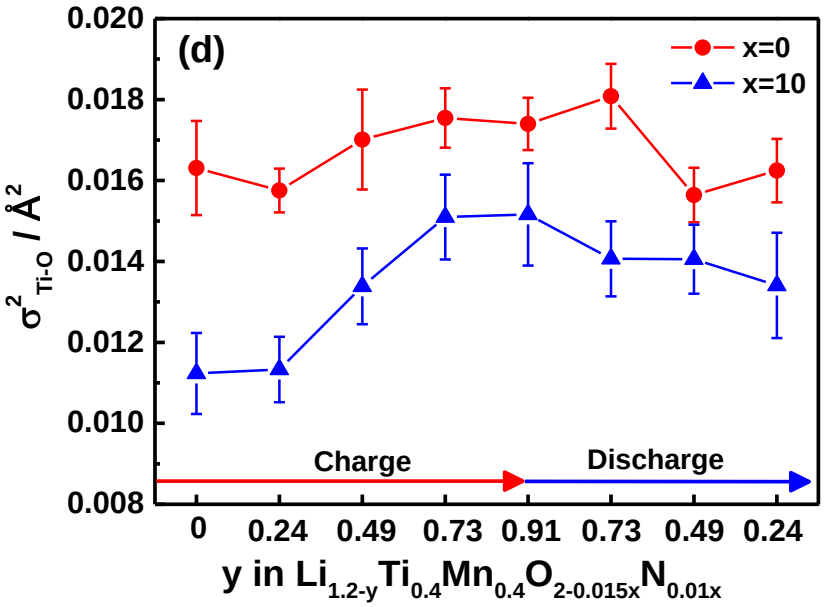

Figure 6-4. Fourier transformed Mn and Ti *K*-edge EXAFS spectra of $Li_{1.2}Ti_{0.4}Mn_{0.4}O_{2-0.015x}N_{0.01x}$ cathode during the 1st charge-discharge reaction. The atomic distance of (a) Mn-O and (b) Ti-O, and the Debye-Waller factors of (c) Mn-O and (d) Ti-O.

6-4. Conclusion

We proposed nitrogen-doping to the lithium rich cathode materials to stabilize the oxygen redox reaction and improve the rate performance. The obtained nitrogen-doped lithium rich cation-disordered cathodes especially with optimized composition $Li_{1.2}Ti_{0.4}Mn_{0.4}O_{1.85}N_{0.10}$ demonstrated the 1st charge capacity about 350 mAh g^{-1}. In addition, nitrogen-doped $Li_{1.2}Ti_{0.4}Mn_{0.4}O_{1.85}N_{0.10}$ cathode materials showed higher rate performance than any other cathode synthesized in this work. The Hard-XAS measurement revealed that the rate performances were improved because local distortion was reduced. The nitrogen-doping cathodes have potential to create new lithium rich cathode materials which achieves greater electrochemical performance without using the high-costed transition metals.

6-5. References

[1] M. Oishi, K. Yamanaka, I. Watanabe, K. Shimoda, T. Matsunaga, H. Arai, Y. Ukyo, Y. Uchimoto, Z. Ogumi and T. Ohta, "Direct observation of reversible oxygen anion redox reaction in Li-rich manganese oxide, Li_2MnO_3, studied by soft X-ray absorption spectroscopy." *Mater. Chem. A.* **4**, 9293-9302, (2016).

[2] A.R. Armstrong, M. Holzapfel, P. Novak, C.S. Johnson, S.H. Kang,M.M. Thackeray and P.G. Bruce, "Demonstrating Oxygen Loss and Associated Structural Reorganization in the Lithium Battery Cathode $Li[Ni_{0.2}Li_{0.2}Mn_{0.6}]O_2$." *J. Am. Chem. Soc.* **128**, 8694-8698, (2006).

[3] N. Yabuuchi, K. Yoshii, S-T. Myung, I. Nakai, and S. Komaba, "Detailed Studies of a High-Capacity Electrode Material for Rechargeable Batteries, Li_2MnO_3-$LiCo_{1/3}Ni_{1/3}Mn_{1/3}O_2$." *J. Am. Chem. Soc.* **133**, 4404-4419, (2011).

[4] M. Sathiya, A. M. Abakumov, D. Foix, G. Rousse, K. Ramesha, M. Saubanere, M-L. Doublet, H. Vezin, C. P. Laisa, A.S. Prakash, D. Gonbeau, G. VanTendeloo and J-M. Tarascon, "Origin of voltage decay in high-capacity layered oxide electrodes." *Nat. Mater*. **14**, 230-238, (2014).

[5] M. Sathiya, K. Ramesha, G. Rousse, D. Foix, D. Gonbeau, A. S. Prakash, M-L. Doublet, K. Hemalatha and J-M. Taracson, "High Performance $Li_2Ru_{1-y}Mn_yO_3$ ($0.2 \leq y \leq 0.8$) Cathode Materials for Rechargeable Lithium-Ion Batteries: Their Understanding." *Chem. Mater.* **25**, 1121-1131, (2013).

[6] Z. Li, F. Du, X. Bie, D. Zhang, Y. Cai, X. Cui, C. Wang, G. Chen and Y. Wei, "Electrochemical Kinetics of the $Li[Li_{0.23}Co_{0.3}Mn_{0.47}]O_2$ Cathode Material Studied by GITT and EIS." *J. Phys. Chem. C*. **114**, 22751-22757, (2010).

[7] Z. Lu and J.R. Dahn, "Understanding the Anomalous Capacity of $Li/Li[Ni_xLi_{(1/3-2x/3)}Mn_{(2/3-x/3)}]O_2$ Cells Using In Situ X-Ray Diffraction and Electrochemical Studies" *J. Electrochem. Soc.* **149**, A815-A822, (2002).

[8] K. Shimoda, M. Oishi, T. Matsunaga, M. Murakami, K. Yamanaka, H. Arai, Y. Ukyo, Y. Uchimoto, T. Ohta, E. Matsubara and Z. Ogumi, "Direct observation of layered-to-spinel phase transformation in Li_2MnO_3 and the spinel structure stabilised after the activation process." *J. Mater. Chem. A.* **5**, 6695-6707, (2017).

[9] Y. Koyama, I. Tanaka, M. Nagao and R. Kanno, “First principles study on lithium removal from Li_2MnO_3.” *J. Power Sources*. **189**, 798-801, (2009).

[10] M.M. Thackeray, S.H. Kang, C.S. Johnson, J.T. Vaughey, R. Benedek, S.A. Hackney, “Li_2MnO_3-stabilized $LiMO_2$ (M = Mn, Ni, Co) electrodes for lithium-ion batteries” *J. Mater. Chem.* **17**, 3112-3125, (2007).

[11] M. Oishi, T. Fujimoto, Y.Takanashi, Y.Orikasa, A. Kawamura, T. Ina, H. Yamashige, D. Takamatsu, K. Sato, H. Murayama, H. Tanida, H. Arai, H. Ishii, C. Yogi, I. Watanabe, T. Ohta, A. Mineshige, Y. Uchimoto and Zempachi Ogumi, “Charge compensation mechanisms in $Li_{1.16}Ni_{0.15}Co_{0.19}Mn_{0.50}O_2$ positive electrode material for Li-ion batteries analyzed by a combination of hard and soft X-ray absorption near edge structure.” *J. Power Sources.* **222**, 45-51, (2013).

[12] M. Oishi, C. Yogi, I. Watanabe, T.Ohta, Y. Orikasa, Y. Uchimoto and Z.Ogumi, “Direct observation of reversible charge compensation by oxygen ion in Li-rich manganese layered oxide positive electrode material, $Li_{1.16}Ni_{0.15}Co_{0.19}Mn_{0.50}O_2$.” *J. Power Sources.* **276**, 89-94, (2015).

[13] T. Ohzuku, M. Nagayama, K. Tsuji and K. Ariyoshi, “High-capacity lithium insertion materials of lithium nickel manganese oxides for advanced lithium-ion batteries: toward rechargeable capacity more than 300 mA h g^{-1}.” *J. Mater. Chem.* **21**, 10179-10188, (2011).

[14] H. Koga, L. Croguennec, M. Menetrier, K. Douhil, S. Belin, L. Bourgeois, E. Suard, F. Weill and C. Delmas, “Reversible oxygen participation to the redox processes revealed for $Li_{1.20}Mn_{0.54}Co_{0.13}Ni_{0.13}O_2$.” *J. Electrochem. Soc.* **160**, A786-A792, (2013).

[15] M. Sathiya, “Reversible anionic redox chemistry in high capacity layered-oxide electrodes.” *Nat. Mater.* **12**, 827-835, (2013).

[16] E. McCalla, A. M. Abakumov, M. Saubanere, D. Foix, E. J Berg, G. Rousse, M-L.Doublet, D. Gonbeau, P. Novak, G. V.Tendello, R. Dominko and J-M. Tarascon, “Visualization of O-O peroxo-like dimers in high-capacity layered oxides for Li-ion batteries.” *Science*. **18**, 1516-1521, (2015).

[17] G. Assat, C. Delacourt, D. A. Dalla Corte and J-M. Tarascon, “Practical Assessment of Anionic Redox in Li-Rich Layered Oxide Cathodes: A Mixed

Blessing for High Energy Li-Ion Batteries." *J. Electrochem. Soc.* **163**, A2965-A2976, (2016).

[18] M. Saubanere, E. McCalla, J-M. Tarascon, and M-L. Doublet, "The intriguing question of anionic redox in high-energy density cathodes for Li-ion batteries." *Energy Environ. Sci.* **9**, 984-991, (2016).

[19] K. Luo, M.R. Roberts, R. Hao, N. Guerrini, D. M. Pickup, Y. S. Liu, K. Edstrom, J. H. Guo, A. V. Chadwick, L. C. Duda and P. G. Bruce, "Charge-compensation in 3d-transition-metaloxide intercalation cathodes through the generation of localized electron holes on oxygen." *Nat. Chem.* **8**, 684-691, (2016).

[20] D. H. Seo, J. Lee, A. Urban, R. Malik, S. Y. Kang and G. Ceder, "The structural and chemical origin of the oxygen redox activity in layered and cation-disordered Li-excess cathode materials." *Nat. Chem*. **8**, 692-697, (2016).

[21] N. Yabuuchi, M. Nakayama, M. Takeuchi, S. Komaba, Y. Hashimoto, T. Mukai, H. Shiiba, K. Sato, Y. Kobayashi, A. Nakao, M. Yonemura, K. Yamanaka, K. Mitsuhara and T. Ohta, "Origin of stabilization and destabilization in solid-state redox reaction of oxide ions for lithium-ion batteries." *Nat. Commun*. **7**, 13814, (2016).

[22] N. Yabuuchi, N. Takeuchi, M. Nakayama, H. Shiiba, M. Ogawa, K. Yamanaka. T.Ohta, D. Endo, T. Ozaki, T. Inamasu, K. Sato and S. Komaba, "High-capacity electrode materials for rechargeable lithium batteries: Li_3NbO_4 -based system with cation-disordered rocksalt structure." *Proc. Natl Acad. Sci. USA.* **112**, 7650-7655 (2015).

[23] M. Nakajima and N. Yabuuchi, "Lithium-Excess Cation-Disordered Rocksalt-Type Oxide with Nanoscale Phase Segregation: $Li_{1.25}Nb_{0.25}V_{0.5}O_2$." *Chem. Mater.* **29**, 6927-6935, (2017).

[24] R. A. House, L.Jin, U. Maitra, K. Tsuruta, J. W. Somerville, D. P. Forstermann, F. Massel, L. Duda, M. R. Robertsa and P. G. Bruce, "Lithium manganese oxyfluoride as a new cathode material exhibiting oxygen redox." *Energy Environ. Sci.*, **11**, 926-932, (2018).

[25] J. Lee, J K. Papp, R J. Clement, S. Sallis, D-H. Kwon, T. Shi, W. Yang, B D. McCloskey and G. Ceder, "Mitigating oxygen loss to improve the cycling

performance of high capacity cation-disordered cathode materials." *Nat. Commun.* **8**, 981, (2017).

[26] F. Kong, C. Liang, R.C. Longo, D-H. Yeon, Y. Zheng, J-H. Park, S-G. Doo and K. Cho, "Conflicting Roles of Anion Doping on the Electrochemical Performance of Li-Ion Battery Cathode Materials." *Chem. Mater.* **28**, 6942-6952, (2016).

[27] N. Takeda, S. Hoshino, L. Xie, S. Chen, I. Ikeuchi, R. Natsui, K. Nakura, N. Yabuuchi, "Reversible Li storage for nanosize cation/anion-disordered rocksalt-type oxyfluorides: $LiMoO_2$ - x LiF ($0 \leq x \leq 2$) binary system." *J. Power Sources.* **367**, 122-129, (2017).

[28] N. Takeda, I. Ikeuchi, R. Natsui, K. Nakamura and N. Yabuuhi, "Improved Electrode Performance of Lithium-Excess Molybdenum Oxyfluoride: Titanium Substitution with Concentrated Electrolyte." *ACS Appl. Energy Mater.* **2**, 1629-1633, (2019).

[29] A. Fukushima, A Hayashi, H. Yamamura and M. Tatsumisago, "Mechanochemical synthesis of high lithium ion conducting solid electrolytes in a Li_2S-P_2S_5-Li_3N system." *Solid State Ionics.* **304**, 85-89, (2017).

Chapter 7. General Conclusion

In chapter 1, the overview of cathode materials mainly focusing on lithium-ion batteries were described. In this study, we conducted detailed analysis focusing on changes in crystal structure and electronic structure for the development of next-generation cathode materials.

In Chapter 2, Li_2TiO_3 and Li_2RuO_3 were taken up as model materials in order to conduct detailed crystal structure analysis in a material system that has been attracting attention in recent years. We clarified the existence of large amount stacking faults and cation mixing in Li_2TiO_3 while small amount in Li_2RuO_3. It is clarified that the difference of crystal structure affects the mechanism of three-dimensional Li diffusion path.

In Chapter 3, structural analysis of magnesium ion battery's cathode material was conducted as research on next-generation cathode material. It was clarified that magnesium ion intercalation reaction can be realized by using cathode material of magnesium ion batteries with olivine-type $FePO_4$ as host structure.

In Chapter 4, the lithium-rich solid solution cathode material using 4*d* transition metal Ru with a wide band structure was synthesized. Compared to the conventional lithium-rich solid solution material using Mn which has a problem of low rate performance due to the large contribution of oxygen charge compensation. Ru can expand the contribution of transition metal redox and suppress oxygen generation. Moreover, the local distortion are relaxed around Ru, then the rate performance was improved.

In Chapters 5 and 6, we attempted to control the electronic state by a new method by nitrogen doping, an anion substitution, for lithium-rich rock salt type cathode materials. Nitrogen substitution has the effect to stabilize the oxygen redox reaction during the charge / discharge reaction, and increased the charge / discharge capacity. It was also clarified that nitrogen substitution reduces local strain, which improves rate performances.

In Chapter 7, the results of the thesis were summarized. The crystal structure analysis and electronic structure analysis of the cathode materials performed in this study will give great knowledge to the future research on electricity storage systems.

Acknowledgment

I would like to express my gratitude to all those who helped me during the writing of this thesis.

My deepest gratitude goes first and foremost to Prof. Yoshiharu Uchimoto at Graduate School of Human and Environmental Studies, Kyoto University, for his constant encouragement and guidance for five years. He has walked me through all the stages of researches, experiments and the writing of this thesis. Without his consistent and illuminating instruction, this thesis could not have reached its present form.

Special thanks are expressed to Prof. Toshiyuki Matsunaga, Dr. Kentaro Yamamoto, Dr. Tomoki Uchiyama at Graduate School of Human and Environmental Studies, Kyoto University, Dr. Yuki Orikasa at Ritsumeikan University and Dr. Koji Nakanishi at University of Hyogo. They have been actively discussing and actively giving advices in my research and experiments. Discussions with them were very helpful in conducting my research.

I would like to appreciate Prof. Akitoshi Hayashi at Osaka Pref. University, Prof. Hiroshi Kageyama at Graduate School of Engineering, Kyoto University, Dr. Kazuhiko Maeda at Tokyo Institute of Technology, Dr. Masatsugu Oishi at Tokushima University and Dr. Keiji Shimoda at Office of Society-Academia Collaboration for Innovation, Kyoto University. They provided appropriate advices to my research.

I am deeply grateful to Prof. Hisao Yoshida and Dr. Mitsuo Tosaki at Graduate School of Human and Environmental Studies, Kyoto University, for their helpful comments of this thesis.

I am also greatly indebted to all the members of Prof. Uchimoto's laboratory. They are reliable members for me who can talk with each other frankly in my research life in Kyoto.

Finally, my thanks would go to my beloved family for their loving considerations and great confidence in me all through these years.

Aruto Watanabe

Kyoto, JAPAN, February, 2020